ALFRED-WEGENER-INSTITUT
HELMHOLTZ-ZENTRUM FÜR POLAR- UND MEERESFORSCHUNG

Arctic nearshore current dynamics and wave climate under declining sea ice conditions

Potential impacts on sediment pathways

A case study from Herschel Island – Qikiqtaruk, Yukon Coast, Canada

Master thesis

to attain the academic degree

Master of Science (M.Sc.) in Geosciences

Submitted by

Justus Gimsa

Institute of Geosciences

University of Potsdam

Potsdam, November 2019

Justus Gimsa

Email: gimsa@uni-potsdam.de

Erstgutachter: Prof. Dr. Hugues Lantuit
Telegrafenberg A45
14473 Potsdam
Email: hugues.lantuit@awi.de

Zweitgutachter: Dr. George Tanski
De Boelelaan 1085
1081 HV Amsterdam
Niederlande
Email: george.tanski@vu.nl

Table of Contents

Index of Figures

List of Abbreviations and Units

°C	Degree Celsius
ADCP	Acoustic Doppler Current Profiler
CTD	Conductivity Temperature Depth Sonde
E	East
h	Hour
Hz	(1/Second)
kHz	Kilohertz
km	Kilometer
m	Meter
m/a	Meter per Year
m/s	Meter per Second
N	North
NOAA	National Oceanic and Atmospheric Administration
ppt	Parts per Thousands
R^2	Coefficient of Determination
S	South
W	West

Zusammenfassung

Der durch den Menschen verursachte globale Klimawandel trifft die Arktis in besonderem Maße. Aufgrund der Erwärmungen großer Teile der Erde, verändern sich Atmosphäre, Kryosphäre und Hydrosphäre. Durch diese Veränderungen sind das arktische Ökosystem, Küstensysteme als auch kulturelle Stätten gefährdet.

Die Erwärmung des Klimas in der Arktis führt zur Beschleunigung der Abtragung eisreicher gefrorener arktischer Küstenlinien. Durch den daraus entstehenden Eintrag von Sediment, Nährstoffen, Schadstoffen und organischem Kohlenstoff, verändert sich das gesamte Ökosystem der arktischen Nahküstensysteme und durch die Umsetzung des Kohlenstoffs zu Treibhausgasen auch die Zusammensetzung der globalen Atmosphäre.

In dieser Arbeit wurde mit Hilfe von direkten Messungen der Strömungen im Nahküstengebiet, sowie der Verbindung zu anderen Messungen und Modellierung der Umweltparameter ein allgemeines Lagebild der Strömungen und deren Ursprung erstellt. Die Strömungen wurden mit Hilfe eines akustischen profilierenden Strömungsmessers (ADCP) für einen kurzen Zeitraum von jeweils zwei Wochen in der westlichen kanadischen Beaufortsee, nahe der Herschel Insel ermittelt und mit Windmessungen, Ergebnissen aus Wellenberechnungen und Wassersäulenschichtungsmessungen verbunden, um deren Einfluss auf die Strömungen festzustellen.

Die Ergebnisse zeigen einen deutlichen Einfluss des Windes auf die Strömung. Dieser Einfluss fällt jedoch je nach Tiefe und Windrichtung unterschiedlich aus und unterliegt somit eines komplexen Gefüges. Darüber hinaus zeigen die Ergebnisse der direkten Wellenmessungen in der zweiten Messung einen deutlichen Einfluss des Meereises auf die Wellenaktivität, sowie eine Reduktion der Strömung, während der Präsenz von Meereis im Studiengebiet, sowie eine Verstärkung der meeresbodennahen Strömung. Dies kann besonders wichtig für die Verteilung von eingetragener Schwebfracht des nahen Mackenzie Rivers während der Abflussspitze im Frühjahr sein.

Besonders wichtig für die weitere Entwicklung der erodierenden Küsten sind die Richtung und die Geschwindigkeit des abgetragenen Sediments im Nahküstenbereich. Diese Parameter hängen entscheidend von den vorherrschenden Strömungsbedingung in dem Bereich ab. Dadurch können die hier erhobenen und ausgewerteten Daten, Einblicke in dieses für die zukünftige Entwicklung der gefrorenen Küste wichtige Zusammenspiel geben.

Abstract

The coast of the Western Canadian Arctic is facing rapid changes under ongoing Arctic warming. As coastal erosion rates are accelerating, detailed insights into the interplay of erosional forcing parameter like wind, waves, the influence of river discharge and currents are needed. The first ever measurements of currents in the nearshore zone of the Western Canadian Beaufort Sea, reveal a substantial effect on winds on the generation of currents. In coupling the data of two current measurements in the summer season, we found that time-lag and potential direction dependence complicate the response. Sea ice played a large role in the reduction of wave activity and largely supressed water movement in the surface layer. In general, a decreased in current speed from surface to bottom was visible at both mooring locations. While at the first location current geometries throughout the water column equal and are directed offshore, at the other site current direction were opposed. The recorded current speed at both sites agree with previous values in the Canadian Beaufort Sea. Yet, with ongoing changes in the environmental forcing of the Arctic Ocean the currents in the study area are likely to change as well. These new insights can help to comprehend the annual cycle of water movement, with insights for the transport of eroded sediment in summer, the redistribution of sediment in fall storms and the spread of Mackenzie plume water in the breakup season. This knowledge may help to improve the protection of threatened historic coastal settlements and understand the further shoreline change development along the Yukon Coast.

1 Introduction

1.1 Motivation

Earth's climate is rapidly warming, very likely to increased greenhouse gas concentrations in the atmosphere. The warming is currently resulting in rapid changes of environments all around the globe (IPCC, 2019). The Arctic and the permafrost regions around the globe are under the most threatened ecosystems. The latest issue of the UN Environment Frontiers series names permafrost thaw as one of the five biggest environmental concerns of humanity (UN Environment, 2019). The central part of the Arctic, the Arctic Ocean, is the region with the largest global warming (AMAP, 2019).

While for a long time it was only the subject of scientific discussions, the topic is increasingly more present in the public communication and arouses concern, "global warming equivalent to an atombic bomb per second", "arctic warming alarmed scientists by the crazy temperatures" (Watts, 2018; Carrington, 2019).

As the global temperatures are warming, and the effect is exceptionally large in the Arctic, due to the Arctic amplification (Serreze & Barry, 2011), the Arctic coasts are under heavy threats. Shrinking sea ice enhances the wave action due to an increase in fetch and an elongated open water season in the Arctic Ocean, resulting in a positive feedback mechanism, that is expected to increase in the future (Khon et al., 2014; Overeem et al., 2011). The emerging Arctic Ocean together with warmer air temperature threatens its weak ice-rich permafrost coasts and leads to its erosion (Lantuit et al., 2012), see Appendix A.

These collapsing Arctic coastlines are not only a potential source for carbon (Lantuit et al., 2009; Tanski et al. 2019) affecting the global carbon stock and can significantly contribute to natural greenhouse gas emissions (Vonk et al., 2012; Wegner et al., 2015), but deliver vast amounts of nutrients (Dunton et al., 2006; Tanski et al., 2016), pollutants such as heavy metals (Fisher et al., 2012; Schuster et al., 2018), and sediments (Obu et al., 2016; Couture et al., 2018) into the sea. While the Arctic is mostly uninhabited, the few coastal settlements and historical sites are widely threatened (Fritz et al., 2017), see also Figure 1-1.

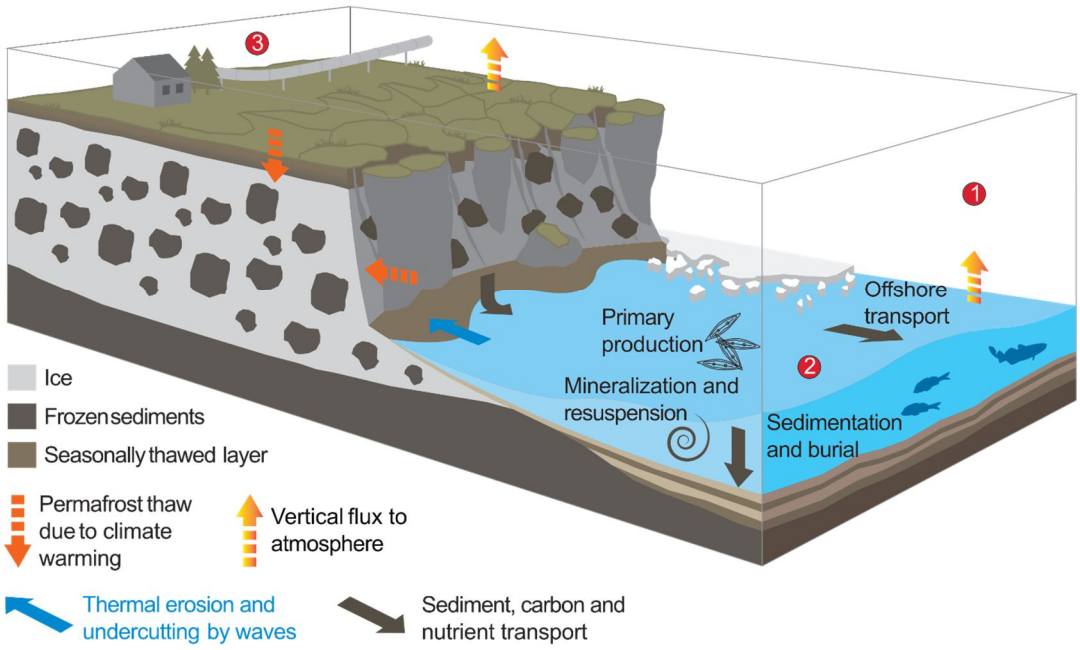

Figure 1-1. Sketch illustrating the threats and effects on environment and ecosystem along thawing permafrost coasts, from (Fritz et al., 2017).

For inhabitants settlements along the Arctic Ocean, the changes cause large concerns of various nature, as infrastructure and buildings are threatened with arctic coastal erosion rates of up to 20 m/s (Jones et al., 2018), 'Protecting Tuktoyaktuk from coastal erosion could cost $50M, says mayor'(Zingel, 2019), and adaptation strategies are conflictual, 'Tuktoyaktuk relocating homes to soon, says resident' (Last, 2019). Even though, attempts are begone to protect cultural treasure, 'Gwich'in partner with researcher to map important sites at risk in a shifting landscape' (Edwards, 2019).

As the Arctic Ocean is losing more and more of its ice, previously hidden resources prompting desires, 'Unlocking Arctic Energy Is Vital for Alaska and America' (Murkowski, 2019), 'Apocalypse Tourism? Cruising the Melting Arctic Ocean' (Orlinsky & Holland, 2016) opens new possibilities, 'China reveals Arctic ambitions with plan for 'Polar Silk Road'' (Wen, 2018) and awakens old conflicts, 'Arctic Melt Heightens U.S. Rivalry With Russia on the Northern Front' (Prapuolenis, 2019). While coastal erosion rates are being continuously reported from several arctic coasts, the controlling factors behind the change are not yet completely understood, and accelerating rates urge for insights (Günther et al., 2013; Jones et al., 2018; Irrgang et al., 2018; Lantuit et al., 2011).

1.2 Objectives

In the Western Canadian Arctic, environmental changes are reported for decades, yet many questions are unanswered. Due to the seasonal ice coverage of the Canadian Beaufort Sea, logistics and long-term measurements are extremely challenging. However, as erosion rates increase (Irrgang et al., 2018), knowledge of the underlain process is needed. The Western Canadian Arctic is known for impressive coastal erosion features like retrogressive thaw slumps are present in the region and are transporting large amounts of material to the sea. These are ice rich permafrost cliffs, that rapidly erode activated by cliff toe wave erosion, and quickly eroding through melting ground ice that is exposed to warm air temperatures during summer

Figure 1-2. Image of waves approaching Simpson Point in the summer of 2017, a highly threatened shoreline at Herschel Island. In the first decade of the 21. century the erosion rates more than doubled to up to 4 meter per year at this site (Cunliffe et al., 2019; Radosavljevic et al., 2016). Note the historic buildings in the hinterland of the spit. Picture from an AWI time lapse camera – Yukon Coast Summer Expedition 2017.

As the erosional force of approaching waves and the removal of eroded sediment with coastal currents, insights into these acting processes and geometry of the acting hydrodynamics are key for a detailed understanding for the coastal erosion. In order to improve the understanding of coastal erosion, an investigation about the hydrodynamics in the zone near the coast is made. Therefore, measurements of current speed and direction over the course of an arctic field season are performed. The data of these measurements is linked to measured waves and additional available data of environmental forcing parameter.

After data assessing and preparation a linkage of the data is performed, to find implications for the properties of sediment transport in the region and develop ideas for conditions under an emerging Arctic Ocean.

2 Scientific Background

2.1 Arctic Ocean and Sea Ice

The Arctic Ocean is the northern most water body of the planet Earth. Compared to other oceans of the planet, it is a relatively small ocean covering an area of about 15.55 x 10^6 km^2 with an average depth of about 1200 m. With its volume of about 18.75 x 10^6 km^3, the Arctic Ocean contains about 1.4% of the global ocean volume (Eakins & Sharman, 2010). The overall bathymetry is very heterogenous, see Figure 2-1.

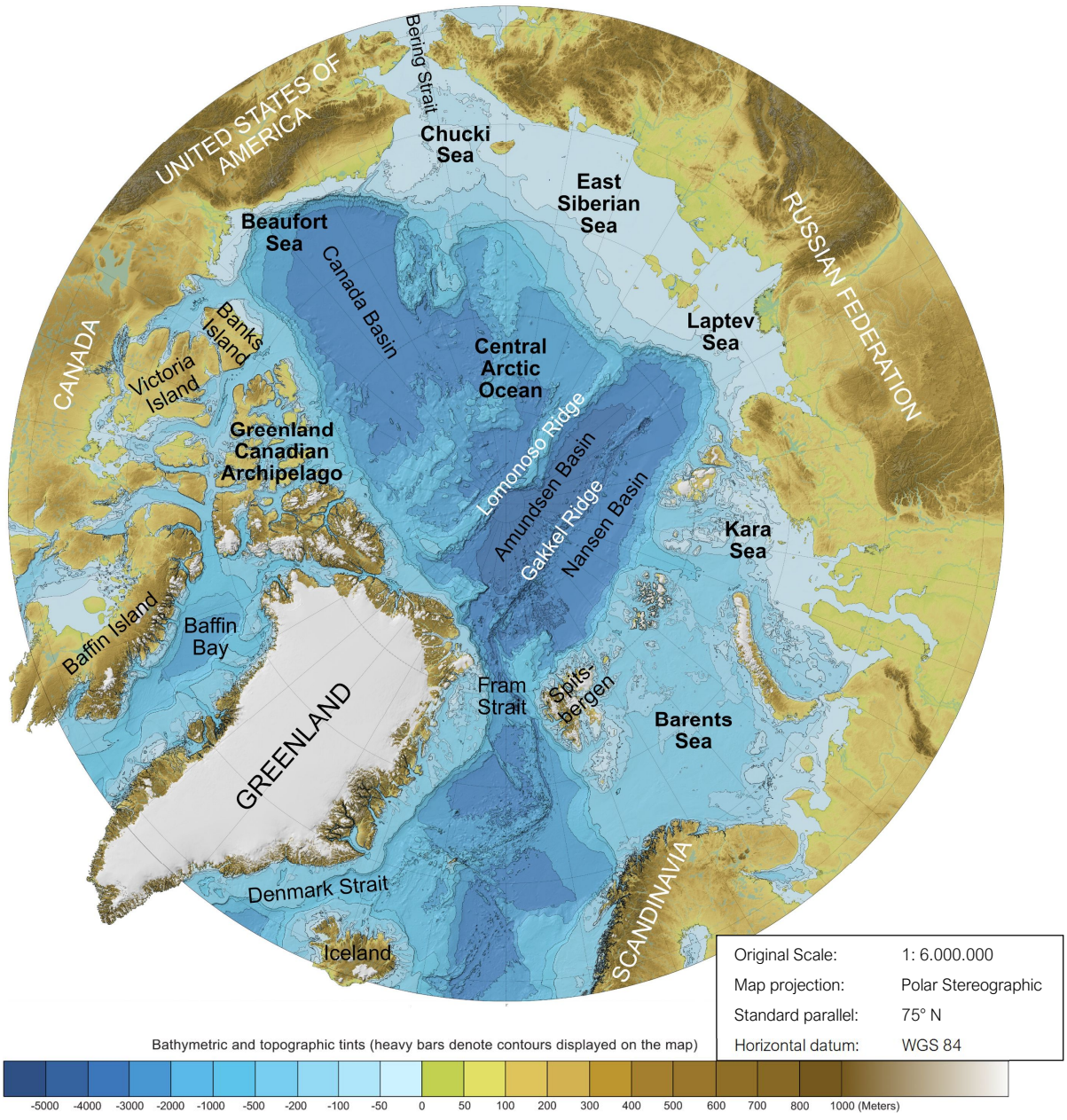

Figure 2-1: Map shows the bathymetry of the Arctic Ocean, adjusted from the International Bathymetric Chart of the Arctic Ocean (IBACO) Bathymetry v3.0 Map (Jakobsson et al., 2012).

The Barents, Kara, Laptev, East Siberian and Chukchi Sea shelf, are extending hundreds of kilometers, with less than 200-meter water depth. They make up about one third of the total size of the Arctic Ocean. In contrast, the Greenland Canadian Archipelago and the Beaufort Sea are relatively narrow shelfs, that transit into deep ocean bathymetry of more than 3000-meter depth in only a little less than 100 kilometres in offshore direction (Williams & Carmack, 2015). The Central Arctic is characterised by the deep bathymetry of large basins, like the Canada-, Makarov-, Amundsen-, and Nansen basin. That have typical depths of 3000 to 5000 metres, and they are surrounded by underwater plateaus and interrupted by large scale ridges, like the Lomonoso and the Gakkel ridge (Comiso, 2010; Jakobsson et al., 2012).

The exchange of water between the Arctic Ocean and other oceans is limited to four gateways: the Bering Strait, the Barent Sea Opening, the Fram Strait and the Davis Strait (Figure 2-2). Additionally, the Arctic Ocean receives vast amounts of fresh, warm and sediment-loaded water inflow from large rivers all over the Arctic (Lammers et al., 2001; White et al., 2007).

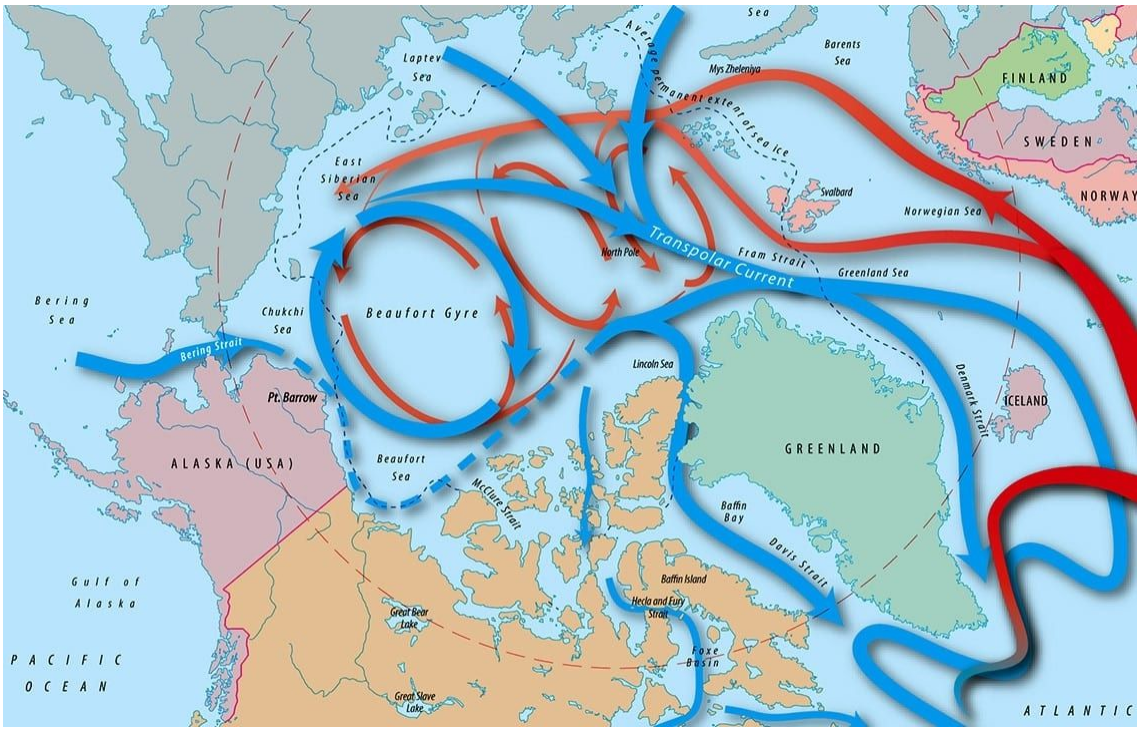

Figure 2-2: Schematic map of major currents of the Arctic Ocean. Map from the website of the Woods Hole Oceanographic Institute (WHOI, 2019).

In consequence of the absence of sunlight, within the polar circle in northern hemispheric winter, the air temperature is extremely cold over the Arctic Ocean. This cold air freezes the

surface water of the Arctic Ocean and forms a mobile layer of sea ice, called pack ice. Depending of the location of formation it is either transported with the Transpolar Current into the Atlantic Ocean, where it melts within a few seasons, or it gets trapped into the Beaufort Gyre (Figure 2-2), where it may 'survive' a melting season and gets older and thicker as multiyear sea ice. In summer, a large portion of the pack ice melts and the ice covered area shrinks drastically.

While the pack ice in the coastal zones of the Arctic Ocean is mobile, sea ice gets attached to the coast (landfast ice) and to the seafloor (bottom fast ice). This locks the coast from freeze up in mid-fall to break up in early summer and largely supresses wave action (Mahoney et al., 2013; Dammann et al., 2019).

Due to the warming of the Arctic in the last decades, the sea ice extent is shrinking, the sea ice thickness is decreasing, the percentage of more stable multiyear ice is declining, and the ice season shortens (Moore et al., 2019). Due to the arctic amplification, that is mostly driven by the decline of sea ice and the resulting decline in albedo, the sea ice loss forms a positive feedback (Serreze & Barry, 2011). A weakened sea ice cover enhances wave action in intensity and duration in the Arctic Ocean, that was previously very limited due to short a fetch and short open water seasons (Overeem et al., 2011; Thomson & Rogers, 2014).

2.2 Permafrost Coasts

The coast of the Arctic Ocean is about 100,000 kilometres long, whereas one-third is classified as lithified and the remaining two-third consists of unconsolidated sediment (Lantuit et al., 2012). Due to the overall extreme cold climatic conditions, sediments are deep-frozen and therefore bounded with ice most of the year. Permafrost is defined as ground, that stayed frozen for more than two consecutive years (French, 2018). In summer, air temperatures far above freezing, lead to an onset of permafrost thaw. Additionally, the open water season in the shelf seas of the Arctic Ocean starts and expose the thawing coasts to erosion.

Along permafrost cliffs two major processes control the erosion, thermo-abrasion and thermo-denudation. Thermo-abrasion occures at the cliff toe, as result of the combination of mechanical action of sea ice and the combined mechanical and thermal action of sea water. Thermo-denudation describes the erosion due to the energy influx on the ground

surface and the resulting thawing of permafrost above the waterline (Günther et al., 2013), see Figure 2-3 for visualization.

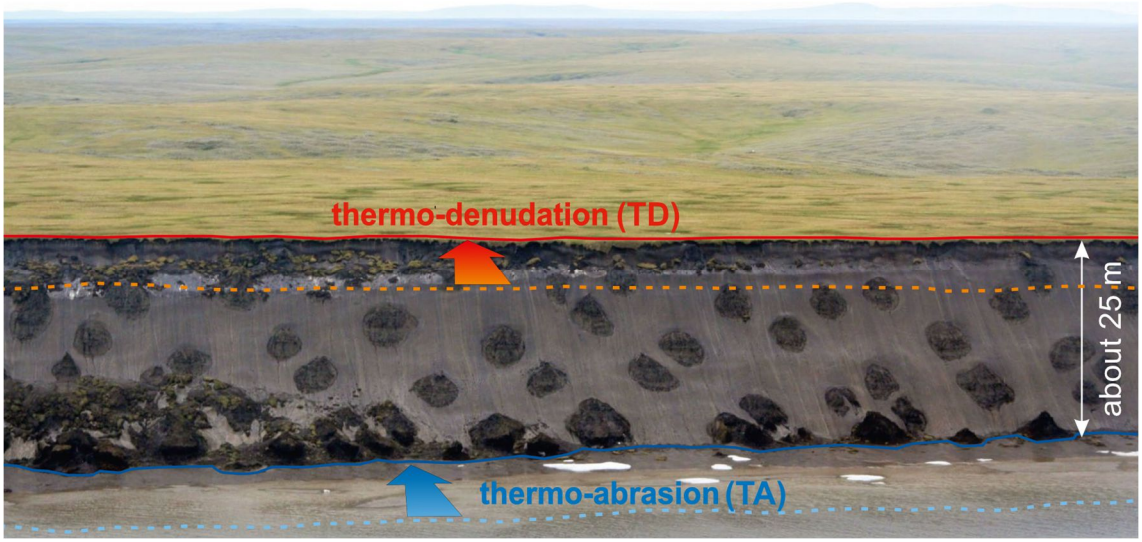

Figure 2-3: Image of an exposed permafrost cliff with marked erosional processes of thermo-denudation and thermo-abrasion from Günther et al. (2013).

Additional and special forms of permafrost coastal erosion are retrogressive thaw slumps (Lantuit & Pollard, 2008), active-layer detachment (Lewkowicz, 1991) and, block failure (Hoque & Pollard, 2009) with different extent and importance along the coastline of the Arctic Ocean. The erosion rates of arctic permafrost coasts are in general higher than the rates along other coasts of the world, even though erosion is mainly limited to the summer months, underlining the importance of the thaw processes. Ice keeling of coastal sea ice was considered to add to high erosion rates, yet Aré et al. (2008) found out, that arctic shoreline profiles don't differ from temperate shorelines, resuming that sea ice plays a minor role in sediment transport and that the wave impact is the major controlling factor. The erosion rate depends on various coastal-, as well as forcing factors. Some of the most important are cliff heights, ice content, orientation, annual air temperature, length of the open water season, fetch length and wave energy. With ongoing climate change, coastal erosion rates accelerate at many sites in the arctic (Irrgang et al., 2018; Jones et al., 2018; Günther et al., 2015), with extreme average rates of more than 20 m/a (Jones et al., 2018) and are expected to further increase (Barnhart et al., 2014a). Unfortunately incomplete data prevents the analysis of the circum-arctic erosion trend (Overduin et al., 2014; Irrgang et al. 2018).

The sediment mobilised by coastal erosion is often organic-rich (Vonk et al., 2012; Couture et al., 2018) or even contaminated with pollutants (Schuster et al., 2018). Degradation of the organic material can either occure within the erosion features or after transport to the

nearshore water (Vonk et al., 2014, 2015; Tanski et al., 2017, 2019) and is transported offshore or distributed alongshore (Hill et al., 1991). This increase in transported material is considered to alter the ecosystem, as well as the global carbon cycle (Fritz et al., 2017).

3 Study Area

3.1 Herschel Island and Herschel Basin

Herschel Island - Qikiqtaruk is an island located in the Yukon Territory, Canada. Its centred at 69.5888°N 139.0888°W, about 116 km² in size and approximately 3 km apart from the Yukon Coast in the Canadian Beaufort Sea (Burn, 2012). It has a maximum elevation of 183 m above sea level (Lantuit & Pollard, 2008). The coastline of Herschel Island is defined by a diverse geomorphology. High and steep cliffs are found on the north and west coast at Collison Head and Bell Bluff, with cliff heights up to 50 m. The east coast is less steep, cliff heights range between 20 and 30 m. At the southern coast, cliffs are relatively low and gentle with a height of about 10 m. The southern side boarders towards the Workboat Passage, a shallow and protected embayment. The island has three accumulation features as sand and gravel spits (Obu et al., 2016), that are named Avadlek Spit, Simpson Point and Osborne Point. For site names and locations see Figure 3-1.

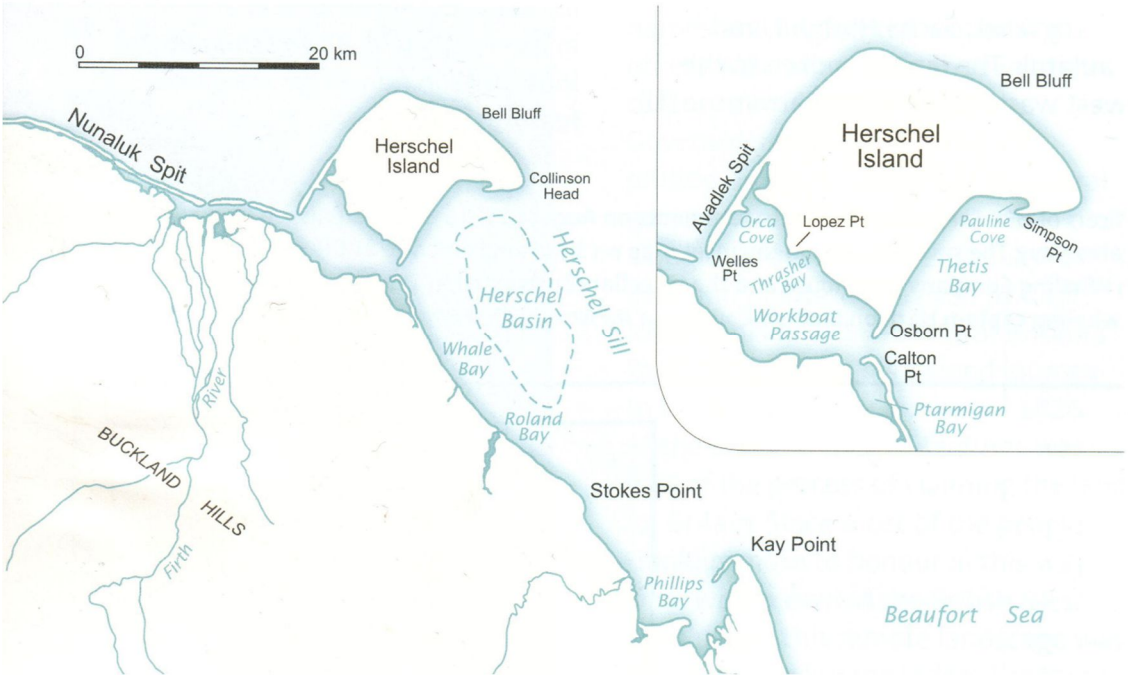

Figure 3-1: Map of the official site names along the coast of the Yukon Territory at the Southern Beaufort Sea. Map is from Burn (2012).

The formation of Herschel island results most likely from the latest advance of a side lobe of the Late Wisconsinan Laurentide ice sheet, around 16.200 years ago. This advance resulted in the build-up of an ice-thrust moraine, ridge out of marine sediments that were previously buried and nowadays form the island. The original burial site of these sediments is called Herschel Basin and is nowadays an about 80-meter-deep depression, in the southeast of

Herschel Island, see bathymetry lines at Figure 3-2 (Lantuit & Pollard, 2008; Rampton, 1982; Fritz et al., 2012).

Herschel Island lies in the continuous permafrost zone with permafrost depths of up to 600 meters (Lantuit & Pollard, 2008). The island is mainly composed of fine-grained, ice-bonded, unconsolidated marine sediments (Pollard, 1990; Fritz et al., 2011). The permafrost here is very ice-rich with an average ice volume between 30% and 60% (Couture & Pollard, 2015; Fritz et al., 2015; Lantuit et al., 2012a).

The climate is polar continental, with an average annual air temperature of -11.0°C (1971-2000), while the average July temperature is 7.8°C (1971-2000), measured at the nearby Komakuk Beach weather station (Burn, 2012). A comparison between nowadays temperature at the Herschel Island weather station and records from 1899 to 1905 indicates a climate warming of about 2.5 °C (Burn & Zhang, 2009).

While most studies describe the wind patterns in the Canadian Beaufort Sea region as bimodal with dominant north-western winds and subordinated easterly winds (Solomon, 2005; Radosavljevic et al., 2016; Burn, 2012), Hill et al. (1991) highlighted southwest wind as a third major wind direction at the Yukon Coast. These winds are associated with mountain barrier baroclinity and the orographic effects of the nearby Brooks Range (Kozo & Robe, 1986), while the bimodal winds are generated around large scale pressure systems in the Beaufort Sea. In general, the wind pattern seems to vary largely from year to year (Fissel & Birch, 1984 as cited in Hill et al., 1991), but recent studies suggest a shift towards more easterly winds (Wood et al., 2013; Wang et al., 2015). In summer, wind speeds are moderate to high with maximum reported wind speeds of 18.6 m/s NW and 12.8 m/s E (Radosavljevic et al., 2016), 11.1 m/s NW and E (Cunliffe et al., 2019), and SW winds of up to 20 m/s (Hill et al., 1991). Storms occurring mostly in fall (Solomon, 2005).

Positive storm surges in the region are associated with a south-eastward water push onto the coast by north-westerly storms. The storm surges can produce a local water level up-set of up to 2.4 m at favourable sites in the Southern Beaufort Sea, but are likely less extreme around Herschel Island (Forbes & Frobel, 1988; Harper, 1988; Hill et al., 1991; Pelletier & Medioli, 2014).

Herschel Island lies within the Canadian Beaufort Sea, a marginal sea of the Arctic Ocean, that is characterised by its steep margin and relatively narrow shelf (William & Carmack, 2015). The Canadian Beaufort Sea coast is considered as wave dominated and microtidal, with an astronomical tide ranging from 0.3 meter to 0.5 meter (Héquette et al., 1991).

Typically, the Beaufort Sea is frozen for eight months of the year, with a freeze-up in October and break-up in June. In the winter season the ice is largely blocking ocean-atmosphere

exchange and wave action. The coastal zone up to the 20 m isobath is then occupied by landfast and bottom fast ice (Mahoney et al., 2013; Carmack & Macdonald, 2002). Ongoing climate warming elongates the ice-free season by more than nine days per decade in the Beaufort Sea (Stroeve et al., 2014). Around Herschel Island rates are even faster, with reported shift of 15 days per decade recently (Barnhart et al., 2014a).

In early summer the combined force of sun radiation and warm water of the Mackenzie River forces the ice to melt and pushes it offshore out of the delta (Dunton et al., 2006). The Mackenzie River is the fourth largest of the big arctic rivers. It has an annual discharge of 316 cubic kilometre per year and considering the size of the shelf, it is the most impactful river of all arctic rivers (Carmack et al., 2015). It provides vast amounts of sediment, warm and fresh water into the Canadian Beaufort Sea and dominates as sediment source (Hill et al., 1991). In summer under east wind conditions, the Mackenzie River plume spreads towards the coastal part of Herschel Island.

When in summer the sea ice retreats, the fetch can get hundreds of kilometres large, occasionally up to 1000 kilometre in recent years (Thomson & Rogers, 2014). In this large open water area, waves up to five meter can be generated under storm conditions in the central part of the Beaufort Sea (Thomson & Rogers, 2014). For the region close to Herschel Island the mean significant wave heights are 0.45 meter to 0.6 meter in July and August, while ranging between 0.9 meter to 1.05 meter in September (1992-2013) (Wang et al., 2015, based on the MSC Beaufort Reanalysis; Swail et al., 2007). Additionally, Wang et al. (2015) showed an increase of significant wave height of about 0.5 % per year (1971-2013), likely due to increased fetch. In-situ measurements of waves in coastal waters are very rare in the western Canadian Beaufort Sea. A study within a two-week period in late summer 1985 near King Point (circa 40 kilometer southeastward of Herschel Island), recorded moderate wave heights up to 0.8 meter (Hill et al., 1991).

The largest current around the Beaufort Sea is the Beaufort Gyre. It flows in westward direction bordering between the Arctic Ocean and the Beaufort Sea shelf. Contrary to this, at the continental slope, the Beaufort Undercurrent is flowing towards the east. On an occasional base, it provides its nutrient-rich water. It is delivered upon the shelf by upwelling events or through Canyons, like the Mackenzie Canyon, around 50 kilometer north of Herschel Island. The flow is considered to mainly wind-driven and variable with speed up to 0.5 m/s in summer, and less than 0.05 m/s in winter (Dunton et al., 2006; Forest et al., 2016).

In the nearshore zone of the Canadian Beaufort Sea, currents are not well studied. The knowledge is gained from a few studies in the Eastern Part of the Canadian Beaufort Sea

and a study at King Point (Davidson et al., 1988; Hill et al., 1991; Hequette et al., 1993). In general, most currents in the coastal zone are wind driven, with an impact of waves depending on site and water depth. A decreasing trend in current strength seaward and down from the water surface. Small scale topography and coastal setting have an impact as well.

The flow speeds range up to 0.5 m/s at the bottom are in general between 0.1 and 0.2 m/s. The direction of flow is highly diverse depending on wind direction, direction of wave approach and up- and downwelling events. Around Herschel Island, Pelletier & Medioli (2014) located the main sediment drifts mainly based of knowledge about dynamical features along the coast, see Figure 3-2.

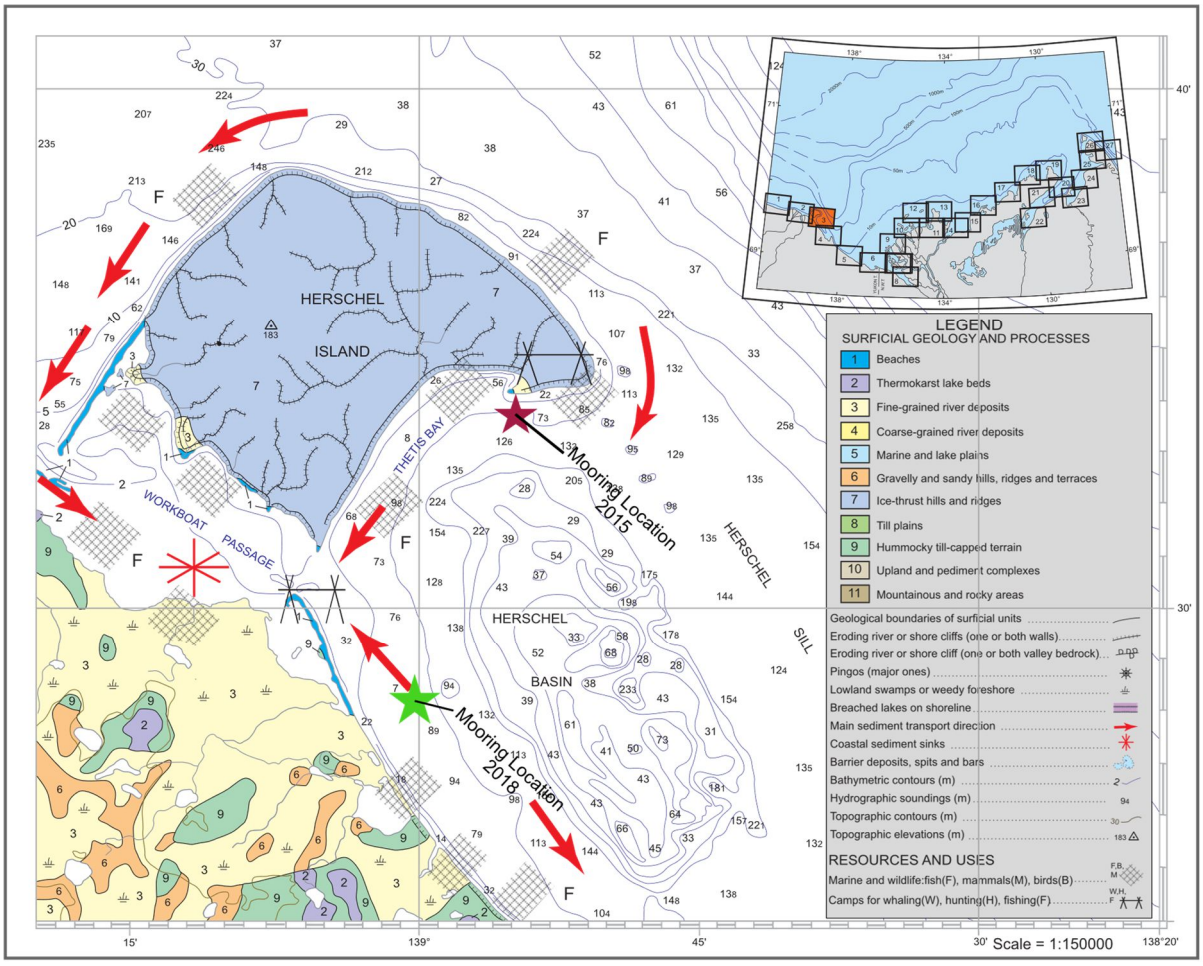

Figure 3-2: Map of Coastal Landforms and Processes around Herschel Island modified from (Pelletier & Medioli, 2014). The mooring sites of 2015 and 2018 are marked as asterisk.

The combination of wave action, currents and thawing in the summer season rapidly erodes the coast along the Yukon Coast and the Mackenzie delta. In the Mackenzie delta erosion rates of up to 22.5 meter per year are measured, with an average rate of 0.6 meter per year (1972-2000) (Solomon, 2005). At the Yukon Coast latest average erosion rates are 1.3 meter per year with locally up to 8.7 meter per year (Irrgang et al., 2018), see Figure 3-2.

At Herschel Island latest average erosion rates are 0.68 meter per year (2000-2011), see Figure 3-3 and show a general increasing trend regarding previous decades (Obu et al., 2016; Lantuit & Pollard, 2008). Cunliffe et al. (2019) showed, that erosion can be highly episodic (hours to days) in the region and short strong wind events can account for large portions of the annual erosion rate.

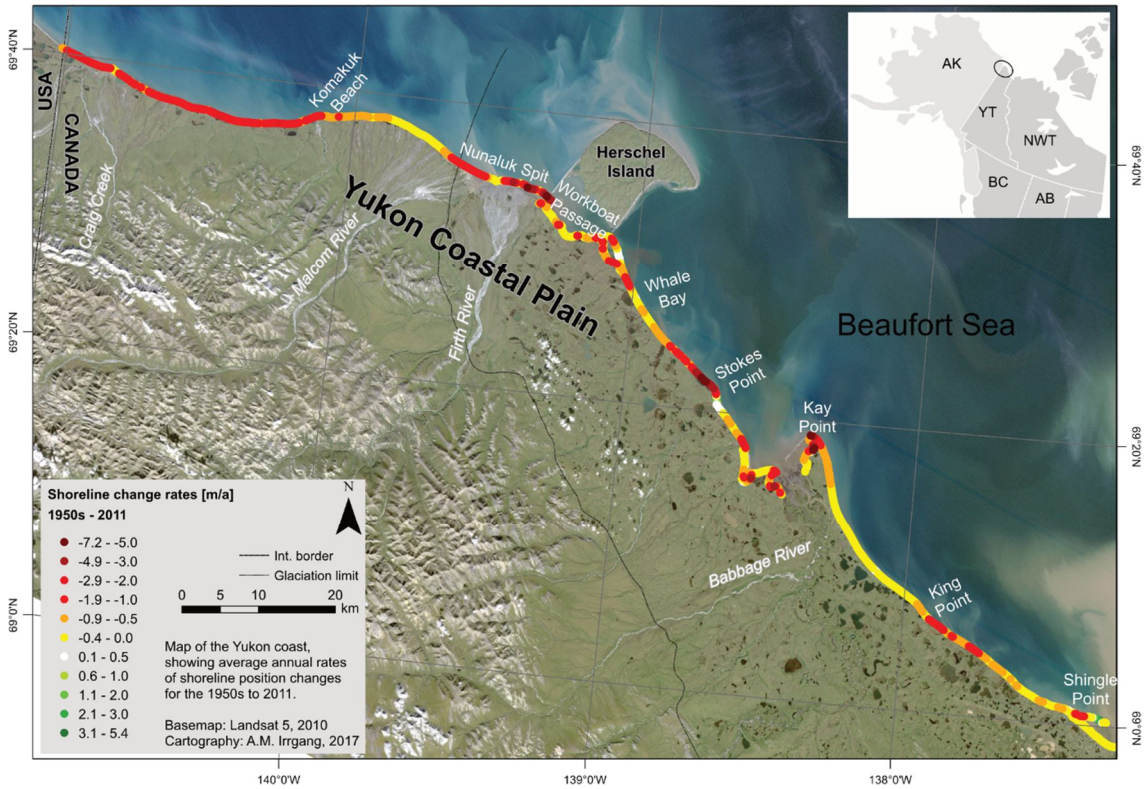

Figure 3-3: Shoreline change rates (1950-2011) along the Yukon Coast, Canada. Map from Irrgang et al. (2018).

The geomorphologic erosion processes in the region include active layer detachment, cliff incising, block failure and retrogressive thaw slumps. The later are known to transport large amounts of sediment, nutrients and carbon into the nearshore waters (Ramage et al., 2018; Tanski et al., 2017). Couture et al. (2018) show an annual flux of 36 x 10^6 kilogram of carbon for the Yukon Coast.

3.2 Location A – 2015 – Simpson Point

The first study site is in the eastern part of Qikiqtaruk, Herschel Island next to Simpson Point. Simpson Point is the location of a historic whaling settlement, it has many archaeological sites, see Burn (2012). It is a spit mostly composed of sand and gravel. It is about 870-meter-long and has a mean elevation of 0.35 m with maximum heights of 1.2 m, see Figure 3-4. Due to its low elevation the spit and the historic sites and buildings are prone to flooding and threatened by the global sea level rise (Radosavljevic et al., 2016).

Simpson Point is attached to an alluvial fan a bit further northeast, that comprised of redeposited marine and glaciogenic sediments. The coastline of this nearby fan consists out of one- to five-meter-high ice-rich bluffs, that erode very fast (Radosavljevic et al., 2016; Cunliffe et al., 2019). The eroded sediment of the retreating fan and the eroded material from the 30-meter-high cliffs of Collison Head towards the northeast are supplying Simpson Point with sediment (Obu et al., 2016; Radosavljevic et al. 2016).

Figure 3-4: Site photography of Simpson Point, photographer (author) stands on top of Slump D, a retrogressive thaw slump at the eastern site of Herschel Island and views towards the east. Scene is from early August 2018. Low lying spit, Simpson Point at the right-hand site, alluvial fan to the left, high cliffs of Collison Head behind. Note the high amounts of sea ice in the Pauline Cove and further offshore in the Southern Canadian Beaufort Sea.

The orientation of the spit is east west, with a natural protection against waves towards the north, the west and a short fetch of less than 20 kilometers towards the south. This orientation leaves the spit only directly exposed to waves approaching from the northeast to southeast. Even under these protected conditions, most of the seaward coastline of the spit is retreating with accelerating rates, of up to 5.5 meter per year (2000-2011), while the landward site towards Pauline Cove is highly dynamic and partly advancing. Overall Simpson Point is threatened by the potential of erosion, the often-occurring floods and the

global sea level rise (Radosavljevic et al., 2016), see Figure 3-5 for illustration of the trend in shoreline movement.

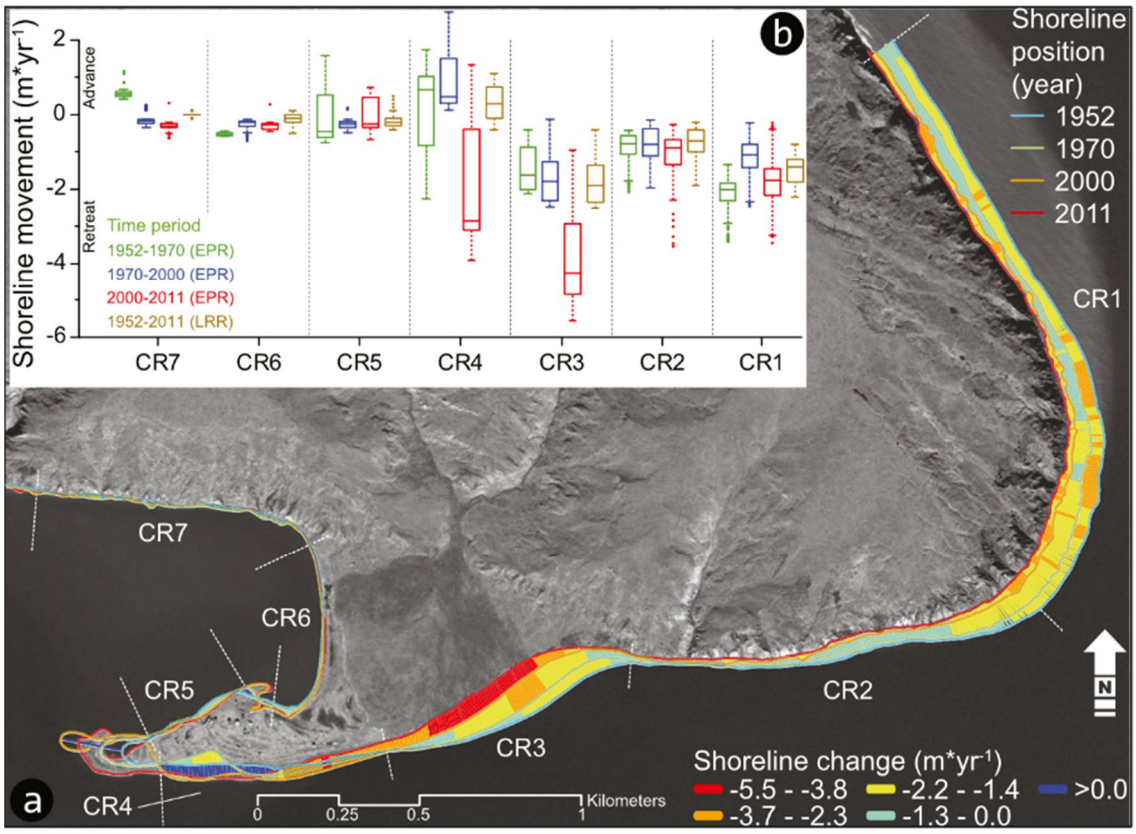

Figure 3-5: Shoreline change rates at the eastern most part of Herschel Island (1952-2011). This map is from Radosavljevic et al. (2016) and highlights the varying shoreline change rates along different coastal transects. Note the deeply incised cliffs of Collison Head at the right, the alluvial fan with its high erosion rates in the left-hand site and the highly dynamic spit Simpson Point in the lower left corner of this map.

The transition from the coast towards the northwestern site of the Herschel Basin is relatively steep. Nearshore zone (up to 20 meter water depth) is up to about 1.5 kilometer from the coast, while the deepest parts of Herschel Basin are around eight kilometer in offshore distance, see Figure 3-8. This indicated the short transport ways for sediment towards the basin and back.

3.3 Location B – 2018 – Catton Point

The second study site named Catton Point or Calton Point, is a five-kilometer-long and 20 to 50 meter wide recurved spit. It separates the Ptarmigan Bay, a shallow lagoon, from the Southern Canadian Beaufort Sea. The spit is striking NNW -SSE and therefore exposed to open water conditions from northeast to southeast (Burn, 2012; Hill et al., 1991).

On this gravelly spit, several traditional hunting and historical sites are located. According to Irrgang et al. (2019), 30 historical features are presented along the spit and seven more at the Ptarmigan Bay. In the central part of the lagoon lies a large relict island with up to five-meter-high bluffs that is boarded towards the inner site of the spit (Hill et al. 1991), see Figure 3-6.

Figure 3-6: Site photography from helicopter towards the southeast. Note the central island in the inner part of the lagoon and the large amount of aligned driftwood logs on the spit. At the right-hand site lies the shallow Ptarmigan Bay lagoon, on the left-hand site Southern Canadian Beaufort Sea. Picture by Goncalo Viera in 2018.

Catton Point builds the southeastern entrance to the Workboat Passage, south of Herschel Island, see Figure 3-7. The Catton Point spit is highly dynamic. A geographic map from 1890 of the area around Herschel Island shows two unconnected barrier islands at the position of nowadays Catton Point, see Appendix B. Irrgang et al. (2019) illustrate its highly dynamic

movement in the last decades (1950-2011) with the usage of satellite imagery, see Figure 3.7.

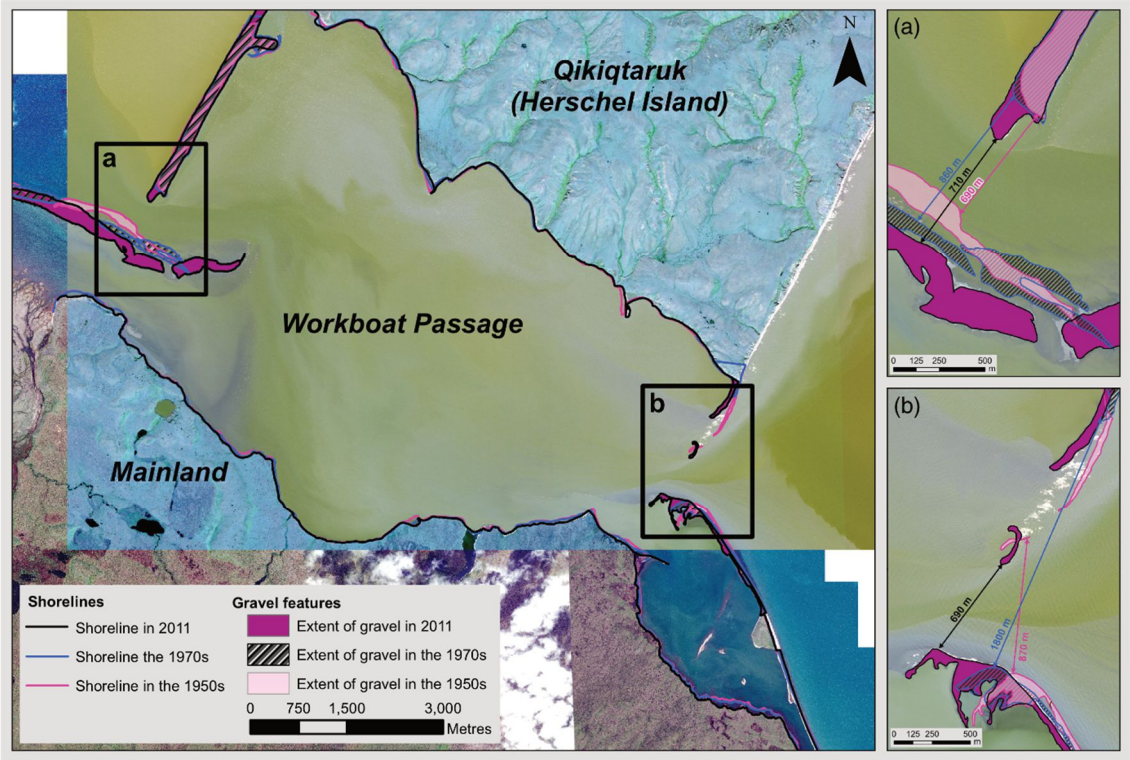

Figure 3-7: Map of dynamic movement of coastal features at the southern end of Herschel Island with a focus on the western and eastern entrance to the Workboat Passage. The lower right-hand site image shows the advance of the Catton Point spit towards the Workboat Passage. This map is from Irrgang et al. (2019).

Shoreline change rates (1950 to 2011) along the Catton Point spit are variable, according to data from Irrgang et al. (2018). The shorelines of the distal part and the proximal parts are retreating with rates up to 1.9 m/a, while the central part around the relict island is stable. The tip of Catton Point is rapidly moving towards the Workboat Passage, with an advance of about 500 m in 61 years (average annual rate of 8.2 m/a), based on Figure 3-7. The supplied sediment probably originates from eroding coasts in downdrift (southeast) direction Irrgang et al. (2018).

The slope from the shoreline of the spit towards the Canadian Beaufort Sea is gentle up to about nine kilometers offshore (15 m water depth), where it steepens towards the central part of Herschel Basin, see Figure 3-8 and 3-9.

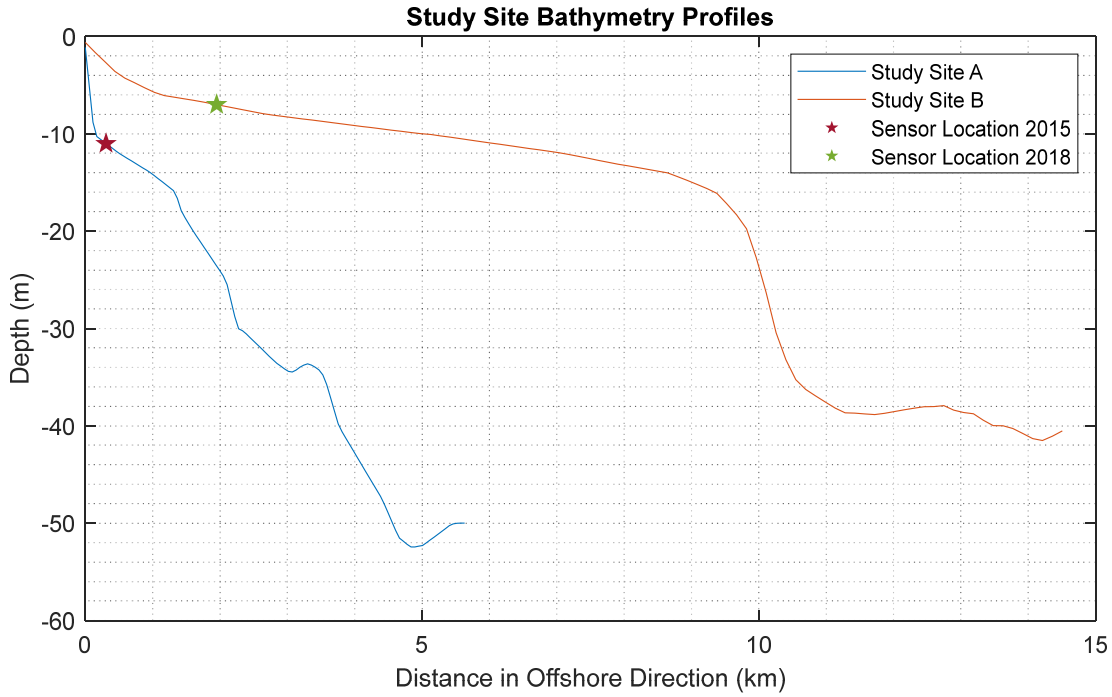

Figure 3-8: Bathymetry profiles approximately perpendicular from the coastline towards the mooring sites and into the basin. Note the difference in slope gradients between the two measurement sites. Profiles were extracted from the bathymetry model below with usage of the TopoToolbox 2 (Schwanghart & Scherler, 2014), uncertainties arise from the limited accuracy of bathymetry data, and the interpolation.

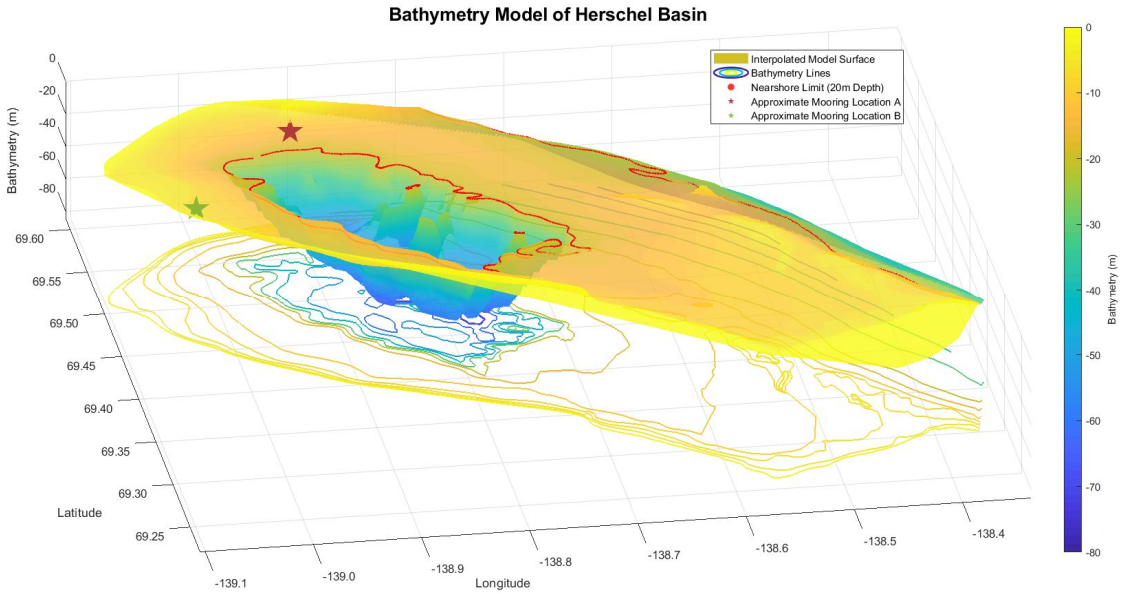

Figure 3-9: Bathymetric model of Herschel Basin. The model is based on bathymetry data from O'Connor (1984), that were digitized by Hugues Lantuit in ESRI ArcMap (ESRI, 2019). In MATLAB, processing and graphic design for this thesis was performed by the author. The bathymetry lines are at 2, 4, 6, 8, 10, 15, 20, 30, 40, 50,60, 70, and 80-meter depth. Refer to the legend of the graphic for symbols. Note the exaggeration and the misleading position of the red start due to an inaccurate resolution at Simpson Point.

4 Methods

This thesis aims to study the influence of environmental forcing factors on currents in the nearshore zone of the study area. Therefore, a current measurement device (ADCP) was mounted at the seafloor in two separate years and related environmental data were obtained, to link the forcing of wind, fetch, waves and stratification on the behaviour of currents at this location.

The first part deals with the acquisition and processing of the in-situ data with moored instruments, publicly available environmental data and modelling products of the study location A – Simpson Point in the year 2015. The mooring started at the 27th of July 2015 at 22:45 and ended at the 14th of August 2015 at 14:15 and was not performed by the author, but by the expedition team of the Yukon Coast 2015 summer expedition.

The second part deals with the acquisition and processing of the in-situ data with moored instruments, publicly available environmental data and modelling products of the study location B - Catton Point in the year 2018. The mooring started at the 4th of August 2018 at 0:00 and ended at the 18th of August 2018 12:00.

For exact and uniform processing and presentation of the data, all data was imported into MATLAB and further analysis and visualisations were performed.

4.1 Measurement Methods Study Location A – 2015

4.1.1 Wind

Wind data was obtained from the nearest official World Meteorological Organisation weather station, due to a failure at the weather station at Herschel Island during the mooring period, the data of the second nearest is taken, which is the Komakuk Beach weather station. This station is listed as number 71046 at the World Meteorological Organisation and roughly 50 kilometer westward of the mooring site (Environment Canada, 2019). This weather station measures air temperature, wind speed, wind direction, dew point temperature, relative humidity and air pressure every minute and averages the data to hourly values. The data was downloaded in XML-format at http://climate.weather.gc.ca. For further processing the hourly wind speed and direction values within the mooring period were extracted and stored in a MATLAB timetable, then the data was averaged into three-hourly mean values for further analyses. The resolution for wind direction is 10 degree and the resolution for wind speed is one kilometer per hour (0.28 m/s).

4.1.2 Sea Ice – Directional Fetch

The concentration of sea ice and the position of the ice edge was obtained using the daily sea ice data from the Canadian Ice Service (CIS, 2005). Daily sea ice charts are available for the western arctic from 1999 on and cover the season from mid June to end of October of each year. They are publicly accessible under the website of Environment and Climate Change Canada (CIS, 2019) and were previously used for other studies of sea ice in the Canadian Arctic (Manson et al., 2016). The product is delivered in gif-format. Every chart contains a geographic coordinate system as grid, sea ice data in form of the international EGG code and an information box about the used sensors to produce the chart. The charts are standardized, containing the same grid and are filled with ice information of available sources, various radar satellites imagery and icebreaker data in the region. They are updated till 18:00 at the specific date.

In the mooring period of 2015, every chart was at least produced with the help of RADARSAT or even higher resolution products. The estimated accuracy of the ice edge position for a 100m resolution imagery, like RADARSAT is given 630 meters (CIS, 2005).

The charts in the mooring period are downloaded and loaded into MATLAB, where the data format was changed from gif to tif (tagged image format). The unprojected charts were imported into ArcMap, where the graticules of the charts were used for georeferencing. Therefore 15 widely distributed grid cross points, spanning the whole area, were used to act as reference points for a 2nd order polynomial transformation.

The georeferenced maps were used to draw a shapeline on the edge of the sea ice to determine the open water area around the moored sensor. The edge was defined as boundary between open water and areas with more or equal than 20 % sea ice concentration, while the resolution of the sea ice concentration of the charts is 10%. In using 20 % as threshold concentration, this study orientated at previous studies that used 15% sea ice concentration as threshold (Overeem et al., 2011; Barnhart et al., 2014a). This is a conservative approach, as other studies used higher sea ice concentrations as determination for areas of no wave propagation (Swail et al., 2007). Even though, Barnhart et al. (2014a) considered this simple approach as enough. Other studies showed that the sea ice concentration as the only input is a simplification and showed that other ice

properties like thickness and flow size diameter play significant roles in their wave dampening effects. (Manson et al., 2015; Zhang et al., 2015).

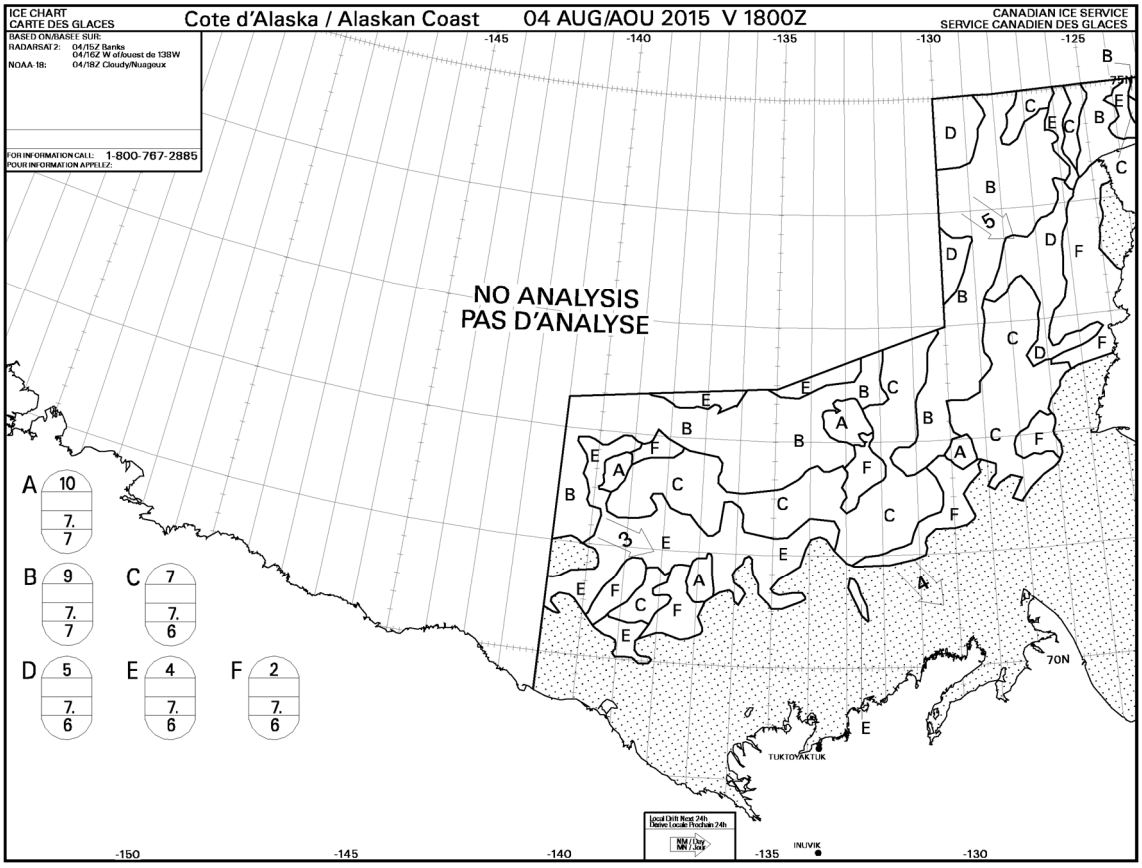

Figure 4-1: Paradigm chart of sea ice product of the Canadian Ice Service (CIS, 2019)

The position of the sea ice edge was mapped starting at the closest sea ice feature to the west and goes on along the ice edge clockwise to the east, until land was reached.

The produced daily sea ice edge shapelines were imported into MATLAB, where they were used together with shoreline data of the GSHHG dataset (global self-consistent hierarchical high-resolution shoreline) (Wessel and Smith, 1996) to determine the distance from the sensor to the nearest sea ice edge or land feature. Therefore, an algorithm was programmed in MATLAB, starting with the position of the sensor, the sea ice edge line of the respective day and the shoreline. It computes, angle preserving lines from the sensor position in each direction and finds the intersection points of the line and the sea ice edge or coastal feature. The closest point is chosen and the distance from the sensor to this point is calculated. The

results are the distances in kilometers to the ice edge or coast at every specific day from 10 to 360 degree in ten-degree increments.

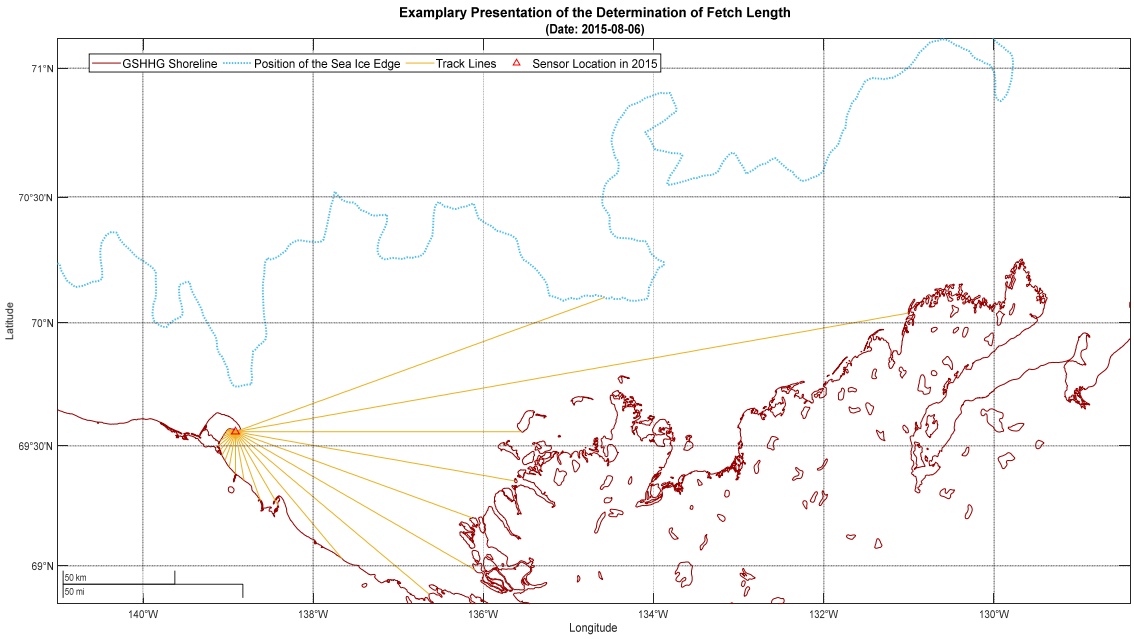

Figure 4-2: Example of the determination of fetch length for a day, here the 6th of August 2015. In MATLAB, the sensor location (red triangle) is used as starting point to determine in every direction (yellow lines) (ten-degree increments) how far the next shoreline (red line) (GSHHG dataset) (Wessel & Smith, 1996) or edge of same or greater than 20% sea ice concentration (light blue broken line) (CIS, 2019), that was mapped before in ArcMap using daily charts of the Canadian Ice Service is (CIS, 2005).

To determine how much distance for wave generation at a specific time was available, the so-called directional fetch was calculated, an approach introduced by Overeem et al. (2011). The hourly wind direction is taken (Chapter 4.1.1) and in the direction the wind was blowing from, the distance to the sea ice (daily updated boundaries) or land from the sensor was defined as fetch at this time. Afterwards the hourly values for the directional fetch were average to three-hourly values.

4.1.3 Modelled Waves

In 2015, the mooring had no instrument for the measurement of waves. To overcome this gap, several options were considered. The best cast would have been measurements of wave height, using buoy data or satellite measurements. Unfortunately, both are unsuitable for this study. Publicly available satellite data in the study area has a poor temporal resolution of about two weeks, which is highly unsatisfying for measurements of wave heights over a short field season. Data from wave buoys, which are widely used for wave measurements in all regions of the world, are not available in the Canadian Beaufort Sea. The closest buoy

to the study site is in offshore waters of the US American Beaufort Sea (National Data Buoy Center, 2019) and are to far away to represent the local waves.

To overcome this gap in direct measured wave properties, available hindcast data are used. The most famous wave hindcast for the Canadian Beaufort Sea is the commercial MSC Beaufort Reanalysis (Swail et al., 2007), that is produced every few years. But unfortunately, they did not produce available data in the study periods. Instead, the NOAA WaveWatch III® (NWW3) multigrid productional hindcast was used (Tolman, 2008; WW3DG, 2016). This hindcast uses all available data, such as daily ice fields and hourly wind data to calculate wave parameter globally in different grids, while each grid can influence each other (Chawla et al., 2013). For further information and the possibility to access the hindcast data the reader is referred to the website of the Environmental Modeling Center (EMC, 2019)

Fortunately, the grid for the coastal waters of Alaska is large enough to cover our study area in the Canadian Beaufort Sea. For the Alaskan coastal waters, the grid resolution is four arc minutes: This is a much higher spatial resolution than the Arctic Analysis and Forecast by the Copernicus service of the European Union has. They use the WAM model (WAMDI Group, 1988; Saetra et al., 2018).

The NWW3 model is occasionally updated and refined. Unfortunately, one of the major updates fell into the mooring period of 2015 (WW3DG, 2016). In order to keep the data comparable within the dataset, as well as with the data from 2018, only wave data after the update is considered. The data calculation changed with the 1st of August 2015 0:00 UTC, which is equivalent to the 31st of July 2015 18:00 at the study site.

The data output has a temporal resolution of three hours and is provided in grib2-format. To simplify the data processing in MATLAB the data was converted into NC file format, using the Netcdf-Java ToolBox from Signell & Bhate (2013) to process the data. The grid point that is nearest to the mooring location is 69.533 °N 138.867°W. Using this grid point, the time-series of wave direction (resolution of 0.01 degree) and significant wave height are obtained (resolution 0.01 m). See Chapter 4.2.4 for further explanation of this parameter. In MATLAB further processing and graphical analysis were performed.

4.1.4 Stratification

To investigate on the layering of the water column, the stratification was measured occasionally near the moored sensor using a handheld CTD probe. The device used was a CastAway® CTD that was lowered from a small boat. The instrument records the position in the water column, the conductivity and temperature at that position. While temperature is

measured directly, the device calculates salinity from measured conductivity. The data is initially stored on the device and can be downloaded afterwards with the associated CastAway® CTD software (Xylem Inc., 2012). The datapoints of interest were selected and exported to MATLAB. In MATLAB data was analysed using basic statistical parameter and was prepared for display.

4.1.5 Currents

The main goal of this thesis is to measure and analyse the currents of the study area in direction and speed.

Various techniques for the measurement of currents are available. Methodical approaches that track the position of a passively flowing drifter over time are known as Lagrangian Method (Joseph, 2014). It provides speed and direction of a flow over a wide area along the path but it is limited in time and more useful to obtain the flow structure over a large area (up to hundreds of km). Techniques that measure the currents stationary, to create time-series of flow velocity and direction, are called Eulerian approaches (Joseph, 2014). It provides a detailed stationary long-term current record throughout the water column and is widely used in coastal engineering and environmental assessments (Joseph 2014).

One device that uses the Eulerian measurement approach is the so-called Acoustic Doppler Current Profiler (ADCP). The ADCP emits acoustic pulses through their beams at a certain frequency through the water column and measures the backscattered doppler-shifted acoustic signal in various predefined depth cells (bins). The pulses get backscattered at particles that drift passively in the water with the speed and in the direction of the water. Signals of actively moving objects like fish are removed in the post-processing to prevent signal errors (Gordon, 1996; Terrey et al., 1999a; Joseph, 2014).

The device used for the study was an RDI Teledyne Workhorse Sentinel 600 kHz ADCP (Teledyne RD Instruments Inc. 2001, 2008). It has four beams that are 20 degree tilted, forming a so-called Janus configuration. The 600kHz stands for the frequency in which the pulses are emitted, different pulse frequencies have different properties in maximum range and resolution (Teledyne RD Instruments Inc., 2008)

Prior to the mooring, the device was calibrated at the field site, following the standard steps of the user guide (Teledyne RD Instruments Inc., 2001), by using the set-up software RD Instrument WinSc (Teledyne RD Instruments Inc., 2001). This includes a beam check, clock check and compass calibration, which is an important step to perform onsite, as magnetic field varies global. Due to the relative proximity to the north pole magnetic field variations

can be rather big (Hamilton, 2001). After calibration and check ups, the measurement properties were configurated. The depth cell was set to 0.50 meter, being a compromise of a small cell size with a relatively large error and a large bin size, with smaller error but less resolution (Teledyne RD Instruments Inc., 2008). The number of cells (bins) was set to 29. The first bin starts at 1.59 meter, which is the first technical possible height above the seafloor to measure, so that potentially a water column of 15.59 meter could be measured. As bathymetry is not completely known in the area the position of the mooring platform, this was to make sure a potential deeper site could also be covered.

The measurement cycle was put to 15 minutes, as a compromise between battery lifetime and coverage. The device works in a way, where in every cycle 50 pulses, so-called pings in equal spacing are emitted, being here a ping every 18 seconds. This ensemble measurement is used to reduce the standard deviation value, which is 12.9 cm/s for a single ping at 0.50-meter bin size by device design. Using an ensemble measurement of 50 pings reduces the standard deviation value to 1.8 cm/s, calculated with the following formula from (Joseph, 2014, p. 342), where σ_{Vmean} is the standard deviation for the speed of an ensemble measurement, σ_{Vping} the standard deviation of the speed for a single ping measurement and $\sqrt{N}$ the square root of the number of pings that are ensembled.

$$\sigma_{Vmean} = \frac{\sigma_{Vping}}{\sqrt{N}}$$

After the pre-deployment software set-up was done, the device was mounted on a steel platform, equipped with a weight and a buoy for platform retrieve and was then lowered from a small boat. The weight keeps the buoy in place next to the platform but a bit off to avoid buoy induced movements to affect the measurements. The platform was mounted at 69.558393°N 138.914445°W in eleven-meter water depth or so, varying with sea level (Figure 3-2 and 3-9) and started recording at the 27th of July 2015 22:45.

At the 14th of August 2015 at 14:15, the platform was retrieved, the data was downloaded from the device and stored. Later imported into RDI Velocity, which is the latest postprocessing software of the Teledyne RD Instruments Inc. (Teledyne RD Instruments Inc., 2018). Using this software, the first step is to calibrate the measurements by determining the salinity. Here 20 ppt was used as compromise between less saline waters of the Mackenzie river plume and the more saline water of the arctic ocean (Mulligan et al., 2010). For density, the standard value was used. For the calculation of the speed of sound the recalculation option of the software was used, that calculates the speed of sound using

temperature, salinity and depth. The value for magnetic declination (22.45°) was obtained from the National Geophysical Data Center for the mooring period and study site (NGDC, 2019).

The "Range to boundary - Intensity" function of the Velocity software was used to remove bins that were affected by turbulent mixing of air particles. The software uses the backscatter intensity for this sorting (Teledyne RD Instruments Inc., 2018). Afterwards the dataset was exported into MAT-file format and then loaded into MATLAB. In MATLAB the data was averaged into three-hourly values, as standard measurement period here for the different environmental parameter. The bins were merged into bottom (1.59 meter above the seafloor to 2.59 above the seafloor), upper water column (9.59 meter above the seafloor to 10.59 meter above the seafloor) and the 14 bins in between (2.59 meter above the seafloor to 9.59 meter above the seafloor) as mid column. The differing column size are used to preserve the signal near the sea surface (upper column) and near the seafloor (bottom column), while using two bins each to prevent potential bin specific errors to falsify the data. The final step was the visualisation of the data in MATLAB (Berens, 2009).

4.2 Measurement Methods Study Location B -2018

The in-situ measurements in 2018 were performed by the author with the help of the team of the Yukon Coast 2018 summer expedition.

4.2.1 Wind

For the study in 2018, the wind data was obtained using the nearest official weather station, which was the Herschel Island Weather Station (WMO Identifier: 71501) (Environment Canada, 2019). The data handling was done like in 2015, explained in Chapter 4.1.1.

4.2.2 Sea Ice – Directional Fetch

The methodical approach and implementation are the same as in the 2015 data period, described in Chapter 4.1.2.

4.2.3 Modelled Waves

The methodical approach and implementation are the same as in the 2015 study, see Chapter 4.1.3., different only in the grid point of data extraction and the period. In 2018, the nearest data point to the sensor location was at 69.4666°N and 139.0001°W.

4.2.4 In-Situ Waves

In Contrast to 2015, the mooring platform had a sensor for measurement of wave height. The logger model was the RBR solo³ D |wave16 (Tsai et al., 2005; RBR Ltd., 2017) which is a nondirectional pressure sensor. It measures the water pressure in a high frequency to reveal fluctuations of the surface. The logger was pre calibrated for up to 20-meter water depth. Prior to deployment the device was configurated using the manufacturers standard software RBR Ruskin, where different measurement profiles are available (RBR Ltd., 2019). The sensor was configurated for the burst mode, where it measures every five minutes 4096 times with a frequency of 16 Hertz (RBR Ltd., 2017, 2018a).

After the set-up, the device was mounted on the ADCP, sitting 0.1 meter above the seafloor. The data was retrieved from the sensor using the RBR Ruskin software, that automatically imports the raw data and calculates wave statistics for the recorded pressure signal (RBR Ltd., 2019). For further analysis the datafile was exported to MATLAB, where a specialised MATLAB Toolbox (RSK MATLAB Toolbox Version 3.1.0) simplifies the work with the dataset (RBR Ltd., 2018b). To separate the measured water pressure from the total pressure (air pressure and water pressure), the raw data was corrected in MATLAB using pressure data that was recorded in a nearby field site at 69.57743°N 138.90130°W (Coch et al., 2018). The used sensor was a HOBO U20 Water Level logger (Onset, 2012). It recorded air pressure every hour, this dataset was exported into MATLAB, where a spline interpolation was performed to resample the data to a five-minute interval. The calculations that are performed in order to transfer the pressure signal to wave statistics can be found in (RBR Ltd., 2018b). The wave parameter that is of most importance for this study is the significant wave height (SWH), which is equal to the average wave height of the highest one-third of all measured waves. This parameter is widely used, when working with wave heights (Francis et al., 2011; Barnhart et al., 2014a). In MATLAB further data statistics and figure preparation was performed.

4.2.5 In-Situ Sea Level

The sensor described in Chapter 4.2.4 does not only measure the water pressure changes occurring from waves, but also pressure change from water level fluctuations like tides and surges. The data of water level above the sensor is used to determine the sea level at the mooring site. The data is displayed in MATLAB.

4.2.6 Stratification

The methodical approach and implementation are the same as in the 2015 study.

4.2.7 Currents

While the methodical approach and the device are the same as in the 2015 study, the implementation is slightly different. The measurement frequency was enhanced, that the sensor took data every minute, ping every 1.2 seconds, instead of every 15 minutes, ping every 18 seconds. The study site was further southeastward at a gentler slope and a shallower site, deployment depth of seven meter. The location was at 69.465833°N 139.030555°W, the mooring started at the 4th of August 2018 0:00 and ended at the 18th of August 2018 12:00. Due to the change in location the magnetic declination value for this site and time period was 20.26°, obtained using the same way as in Chapter 4.1.5.

Due to the shallower depth, the number of bins decreased, so after removing of the topmost bins, see Chapter 4.1.5, the lowest two bins were used as bottom (1.59m above the seafloor to 2.58 meter above the seafloor), the upmost two were used as upper water column (4.59m to 5.59m above the seafloor) and the four bins (2.59m to 4.59m above the seafloor) in between were used as mid water column.

5 Results

The result section is following the methodical structure of this thesis and separates the 2015 data set near Simpson Point from the 2018 data set near Catton point. The first study started at the 28th of July 2015 0:00 and ended at the 13th of August 2015 15:00, the results of this are shown in part 5.1. The second study period spans from the 4th of August 2018 0:00 to the 18th of August 2018 15:00, the results of this are shown in part 5.2.

In the third and fourth part of this chapter, a simple statistical analysis is presented, to investigate on the linkage between environmental forcing parameter and the response of the currents, again separated by years.

5.1 Results for Study Location A – Simpson Point 2015

5.1.1 Wind

The measurement period for the 2015 mooring started at 28th of July 2015 0:00 and ended on the 13th of August 2015 15:00. The maximum wind speed was 15.3 m/s (55.1 km/h) at 10th of August 2015 21:00, minimum wind speed occurred at 13th of August 2015 6:00 0.6 m/s (2.2 km/h). The mean value for the wind speed is 5.3 m/s (19.1 km/h), the median value 4.7 m/s (16.7 km/h) and standard deviation value is 3.0 m/s (10.8 km/h).

One arctic storm event, following the arctic storm definition of Atkinson (2005), where an arctic storm is a period of at least 6 hours with wind speeds of at least 10 m/s, occurred. The storm started at the 10th of August 2015 at 12:00 and ended at the 11th of August 2015 at 06:00, the wind was coming from west, with wind directions between 260 degree and 280 degree. The wind speed varied from 10.6 to 15.3 m/s (38.2 km/h to 55.1km/h). The time series of wind measurements in 2015 is visualised in Figure 5-1.

The wind direction in the measurement period varied from 27 degree to 340 degree (clockwise). The wind data is presented, following the meteorological convention, where the direction indicates the origin of the wind (Thomson & Emery, 2014). NE to SE winds had varying wind speeds, wind from SE to SW had only low wind speeds, while winds from SW to NW had varying speed. Additionally, a very few winds were recorded from N. In Figure the 5-2, the distribution of wind in the 2015 measuring period is illustrated in a polar scatter plot.

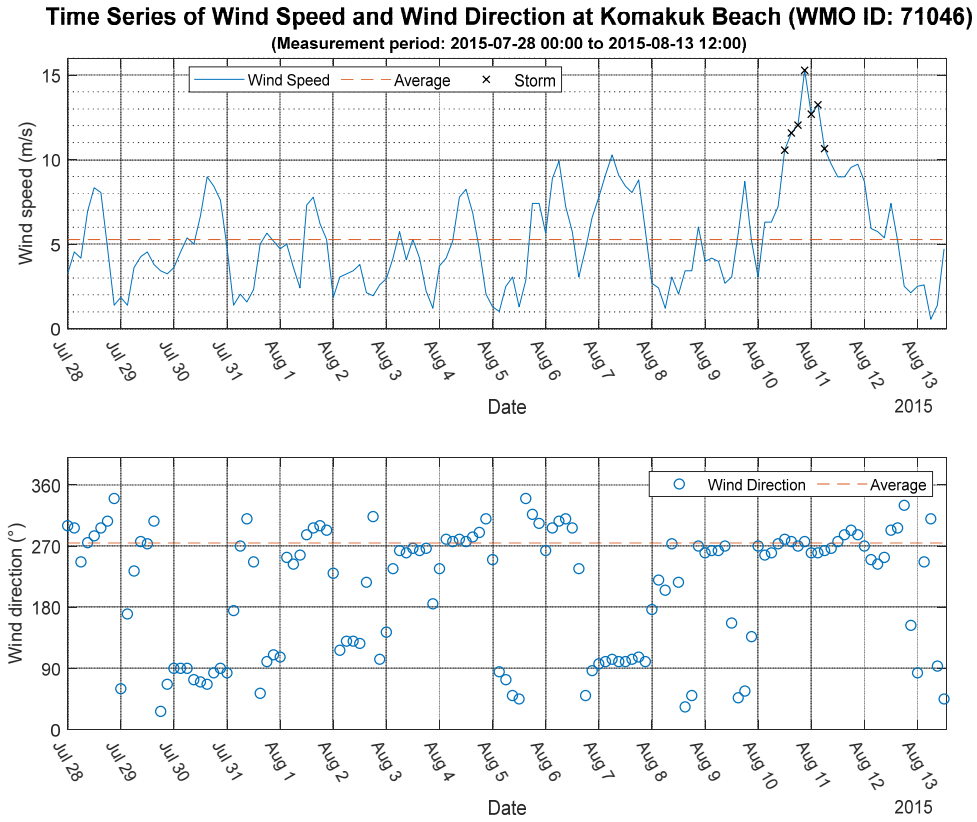

Figure 5-1: Top - Wind speed in the 2015 measurement period, obtained from the Komakuk Beach weather station (WMO ID: 71046). The blue line indicates wind speed, orange broken line indicates the mean value within the period, black cross the storm events, following the arctic storm definition of Atkinson 2005 (at least 6 hours of at least 10 m/s wind speed). Bot – Wind direction in the 2015 measurement period, obtained from the Komakuk Beach weather station (WMO ID: 71501). Blue dots indicate wind direction, where the wind is coming from (meteorological convention) in degree. The broken orange line indicates the mean wind direction within this period.

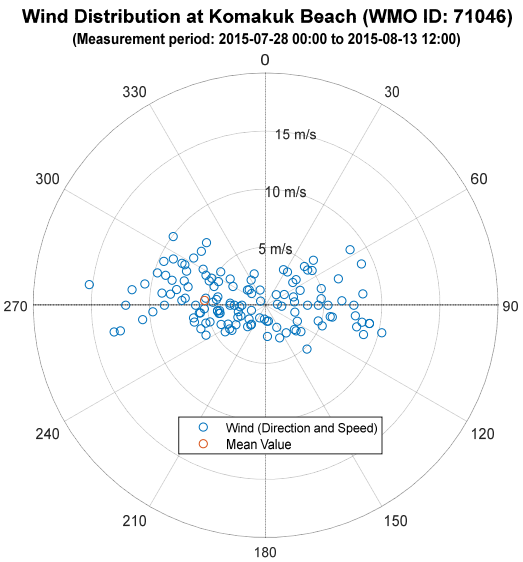

Figure 5-2: Polar scatter plot of wind direction and speed during the 2015 measurement period recorded at the Komakuk Beach weather station (WMO ID: 71046). Blue circles indicate wind direction in degree and wind speed in m/s. The red circle is the mean wind speed and direction in the measurement period.

5.1.2 Sea Ice – Directional Fetch

Directional fetch was calculated for the 2015 mooring period from the 28th of July 2015 0:00 to the 13th of August 2015 12:00. Within this period the direction from which the wind is blowing is taken and, in an angle preserving line (rhumb line) from the sensor location the distance to the next land or field of more than 20% sea ice was calculated. The maximum fetch during this period is 506 km, occurring at the 30th of July 2015 09:00 and the 5th of August 2015 06:00. Minimum value was calculated for the 6th of August 2015 15:00 with a fetch of 0 km. The median value for the data is 5 km, while mean value is 53 km, illustrating that periods of very long fetch are influencing the mean value quite strong. The standard deviation is 91 km.

Extended periods of long fetch, above 100 km, occurred between the 29th of July 2015 21:00 and the 30th of July 2015 21:00, between the 2nd of August 3:00 and 12:00, the 2nd of August 2015 21:00 and the 5th of August 2015 0.00, and between the 6th of August 2015 21:00 and the 7th of August 2015 21:00. The time series of the directional fetch with the measurement period is shown in Figure 5-3. In Figure 5-4, the average and the maximum potential fetch during the measurement period in every direction is displayed. On the left in a large scale, zoomed imagery and in a big picture scenery to the right. This Figure illustrates the wind directions with the highest potential to generate waves.

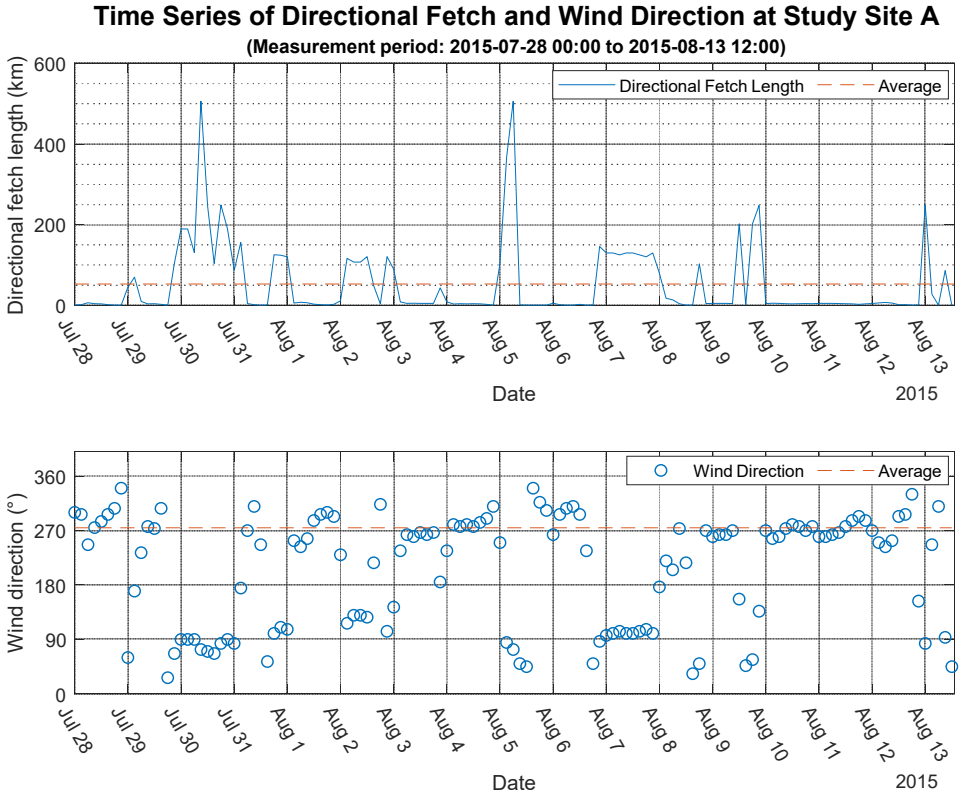

Figure 5-3: Top – Blue line indicates the directional fetch in the 2015 measurement period. This was calculated for the 2015 mooring site (69.558393°N 138.914445°W). The wind direction is

obtained from the Komakuk Beach weather station (WMO ID: 71046), to determine the direction, where the wind is coming from. Daily sea ice charts of the Canadian Ice Service and the GSHHG coastline data were used to determine the possible distance for wave generation in this direction. Broken orange line is the average value within the period. Bot – Wind direction in the 2015 measurement period, obtained from the Komakuk Beach weather station (WMO ID: 71046). Blue line indicates the wind direction, where the wind is coming from in degree. The broken orange line indicates the mean wind direction.

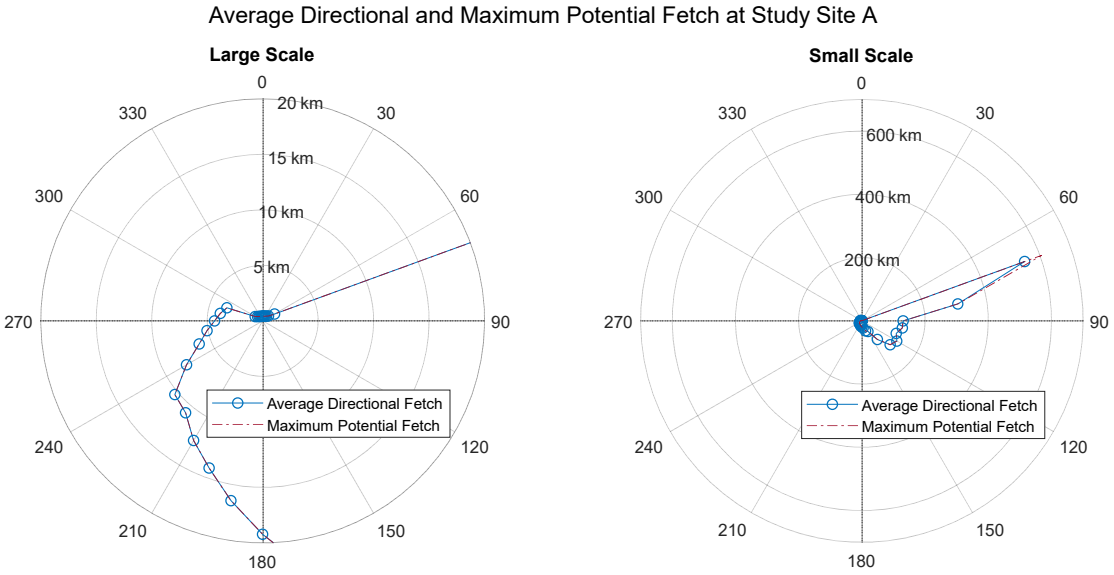

Figure 5-4: Polar plots of the average potential fetch and the maximum (no sea ice) fetch length in the 2015 measurement period. On this plot the sensor is "located" in the center of the plot. The average distance to the next wave blocking feature (land or sea ice with a concentration of more than 20%) in each direction in ten degree increments is shown. Daily sea ice charts of the Canadian Ice Service and the GSHHG coastline data were used, to determine the possible distance for wave generation in this direction. The left side and the right side plot show the same situation with different scales. Distance in km, direction (zero equals N).

5.1.3 Modelled Waves

The obtained data of the NOAA WAVEWATCH III® model hindcast covers the period from the 31st of July 2015 18:00 to the 13th of August 2015 12:00, which is a little shorter than the mooring period, as explained in Chapter4.1.3. Within this period at the point of interest, the maximum calculated wave height is 1.04 m at the 11th of August 6:00, minimum value occurred at the 3rd of August 2015 12:00 with 0.04 meter. The median value for this period is 0.32 m, the mean value 0.39 m. Data has a standard deviation of 0.25 m. Visualisation of the time series can be found in Figure 5-5.

The mean wave direction is at 23 degree (coming from). In the data period, waves occurred from nearly all directions, although no waves were recorded between 10 and 50 degree, 130 to 215 degree and 220 and 270 degree. Between 310 and 320 degree, 0 and 5 degree and 70 to 120 degree waves larger than 0.50 m occurred. They occurred within two periods, one from the 7th of August 6:00 to the 8th of August 9:00 2015 and from the 10th of August 12:00 to the 12th of August 9:00. The directional distribution of wave heights for the period can be seen in Figure 5-6.

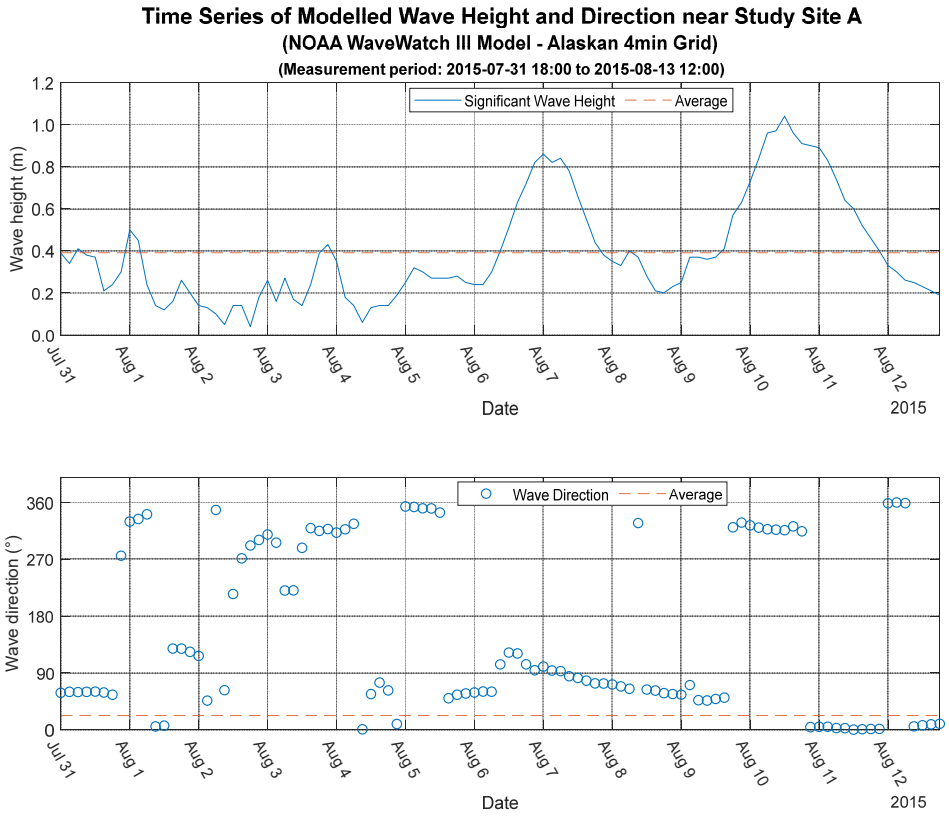

Figure 5-5: Top – NOAA WAVEWATCH III® modelled wave heights at 69.533°N 138.867°W. Data period is from the 31st of July 2015 18:00 to the 13th of August 2015 12:00. Broken orange line indicates the mean value. Bot - NOAA WAVEWATCH III® modelled wave directions (meteorological convention) for the same grid point and the same period. The orange line indicates the mean value.

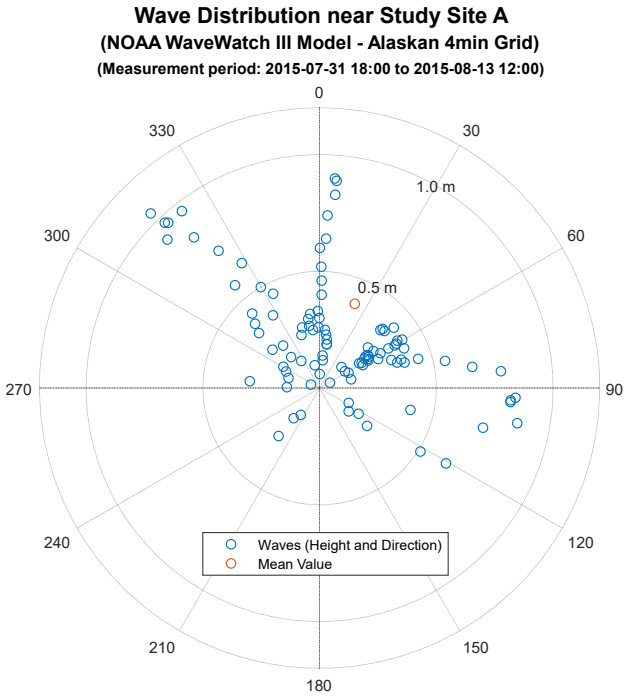

Figure 5-6: Polar scatter plot of the NOAA WAVEWATCH III® modelled wave heights and directions (meteorological convention) at 69.533°N and 138.867°W. Data period is from the 31st of July 2015 18:00 to the 13th of August 2015 12:00. Red circle indicates the mean value in direction and height.

5.1.4 Stratification

Within the mooring period, four CTD profiles were taken nearby the moored ADCP. The measurements took place at the 28th of July 22:15, the 30th of July 20:43, the 5th of August 20:35 and the 9th of August 01:28 2015. Each profile contains 68 measurements or so, between 0.15 m and 20.35 m water depth. They were taken near 69.5521° N 138.9228° W. In focus are the parameters salinity in ppt and temperature in °C.

At the first measurement, the maximum salinity was 31.77 ppt in 20.81 m water depth. The minimal value for the salinity was 15.54 ppt at 0.15 m water depth. The mean salinity value for the first measurement is 24.97 ppt. The temperature was maximal in the profile at 0.45 m water depth with 9.78°C. At 20.51 m the temperature was minimal with 0.58 °C. The mean temperature was 4.94 °C.

At the second measurement the maximum salinity was 31.48 ppt in 20.55 m water depth. The minimal value for salinity occurred at 0.15 meter water depth with 15.47 ppt. The mean salinity value for the second measurement is 24.51 ppt. The temperature was maximal in the profile at 1.36 m water depth with 9.90 °C. At 20.55 m the temperature was minimal with minus 0.20 °C. The mean temperature was at 5.43 °C.

At the third measurement the maximum salinity was at 31.44 ppt in 20.35 m water depth. The minimal value for salinity occurred at 2.26 m water depth with 19.81 ppt. The mean salinity value for the third measurement is 25.20 ppt. The temperature was maximal in the profile at 2.56 m water depth with 9.49 °C. At 20.35 m the temperature was minimal with minus 0.15 °C. The mean temperature was at 5.75 °C.

At the fourth measurement the maximum salinity was at 30.57 ppt in 19.56 m depth. The minimal value for salinity occurred at 0.15 m water depth with 16.69 ppt. The mean salinity value for the fourth measurement is 28.10 ppt. The temperature was maximal in the profile at 0.15 m water depth with 10.51 °C. At 19.56 m water depth the temperature was minimal with 0.17 °C. The mean temperature was at 2.63 °C.

The full profiles of salinity and temperature for all measurements in 2015 are shown in Figure 5-7.

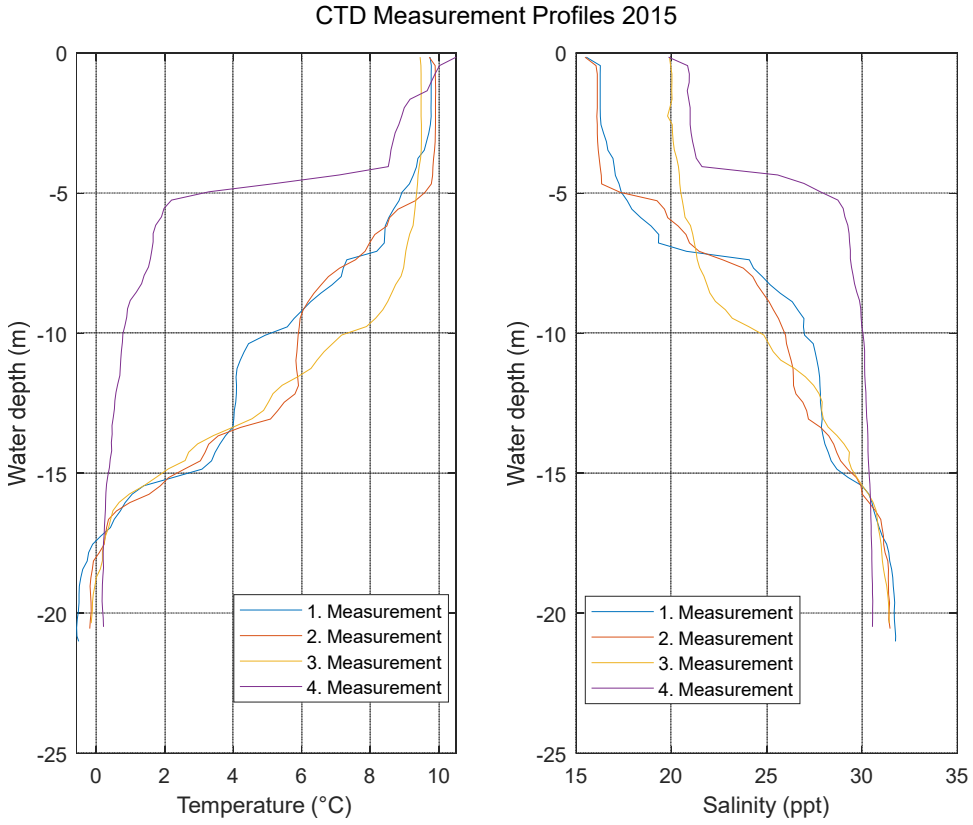

Figure 5-7: CastAway®-CTD measurement profiles in the 2015 mooring period. On the left side depth profiles for temperature (in degree Celsius), on the right side depth profiles for salinity (in parts per thousand). The location was at 69.5521°N 138.9228°W. The first measurement was at the 28th of July 22:15, the second one at the 30th of July 20:43, the third one at the 5th of August 20:35 and the fourth one at the 9th of August 01:28 2015.

5.1.5 Currents

Current measurement in 2015 started at the 28th of July at 0:00 and ended at the 13th of August at 15:00. The data is divided into upper, mid and lower column currents, where the upper column contains the averaged two topmost nonremoved bins. The lower one, the averaged two lowest bins, and the mid column are the 14 layers in between. Due to the sensor restrictions the lower column starts at 1.59 m above the seafloor and ends at 2.59 m. The middle column starts at 2.59 m and ends at 9.59 m above the seafloor. The upper most column starts at 9.59 m and ends at 10.59 m above the seafloor.

In the upper column, the mean flow speed in the measurement period is 0.18 m/s. The median value is 0.17 m/s. The flow speed was minimal the 4th of August 0:00 with 0.02 m/s. The maximum flow speed occurred at the 10th of August 03:00 and reached 0.54 m/s. The standard deviation within the period is 0.11 m/s. In total, the current speed was 26.1 % of the time below 0.10 m/s, 36.6 % of the time between 0.10 and 0.20 m/s. Values of 0.20 to 0.30 m/s were reached at 23.1 % of the time and current speed exceeded 0.30 m/s, 14.2% of the time.

In the upper column, currents were directed (direction in which the current is flowing (oceanographic convention)) in nearly all directions. Even though, a gap between 192 degree and 263 degree in clockwise direction exists. The mean direction in the upper column is 132 degree. Whenever the current speed exceeds 0.20 m/s, it was directed between 125 and 182 degree. In general, most of currents are directed in this direction. The time series for the current speed and direction for the upper column can be found in Figure 5-8. The distribution of currents speed per direction for the upper column is shown in the polar scatter plot in Figure 5-9.

In the mid column, the mean and median flow speed in the measurement period is 0.12 m/s. The flow speed was minimal at the 30th of July 15:00 with 0.01 m/s. The maximum flow speed occurred at the 29th of August 03:00 and reached 0.32 m/s. The standard deviation within the period is 0.08 m/s. In total, the current speed was 37.3 % of the time below 0.10 m/s, 50.0 % between 0.10 and 0.20 m/s. Values of 0.20 to 0.30 m/s were reached at 11.2 % of the time and currents exceeding 0.30 m/s occurred 1.5% of the time.

In the mid water column, currents occur at all directions, even though a large gap of currents exceeding 0.10 m/s exists between 176 degree and 337 clockwise. The mean direction is 106 degree. If the current speed exceeded 0.20 m/s, the direction is either between 338 degree and 2 degree or between 90 and 160 degree clockwise. The time series for the current speed and direction for the mid column can be found in Figure 5-10. The distribution

of currents speed per direction for the mid column is shown in the polar scatter plot in Figure 5-11.

In the lower column, the mean flow speed in the measurement period is 0.09 m/s and the median value 0.08 m/s. The flow speed was minimal at the 8th of August 12:00 with 0.01 m/s. The maximum flow speed occurred at the 9th of August 09:00 and reached 0.23 m/s. The standard deviation within the period is 0.05 m/s. In total, the current speed was 68.7% of the time below 0.10 m/s, 27.6 % between 0.10 and 0.20 m/s. Values of 0.20 to 0.30 m/s were reached at 3.7 % of the time. and currents exceeding 0.30 m/s occurred 1.5% of the time.

Within the measurement period, the current direction is widely spread. If the flow speed exceeded 0.10 m/s, it was directed either between 105 and 174 degree or between 309 and 5 degree, clockwise. The mean current direction is 87 degree. The time series for the current speeds and directions for the lower column can be found in Figure 5-12. The distribution of currents speed per direction for the lower column is shown in the polar scatter plot in Figure 5-13.

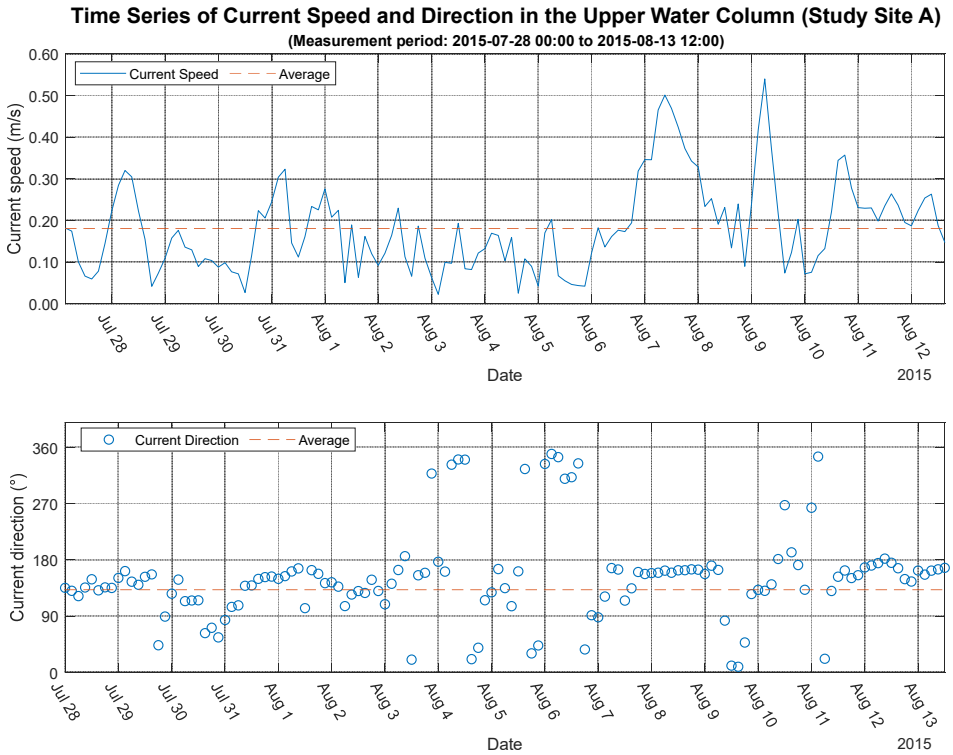

Figure 5-8: Current speed and direction for the upper water column, 9.59m to 10.59m above the seafloor. The values are 3-hourly means, measured with a 600kHz ADCP. The measurement period covers the period from the 28th of July 0:00 to the 13th of August 15:00 2015. The sensor was located at 69.558393°N 138.914445°W. Top - Blue line indicates the current speed, while the broken orange line shows the mean value for the period. Bot – The blue circles indicate the direction and the broken orange line indicates the mean direction over the measurement time.

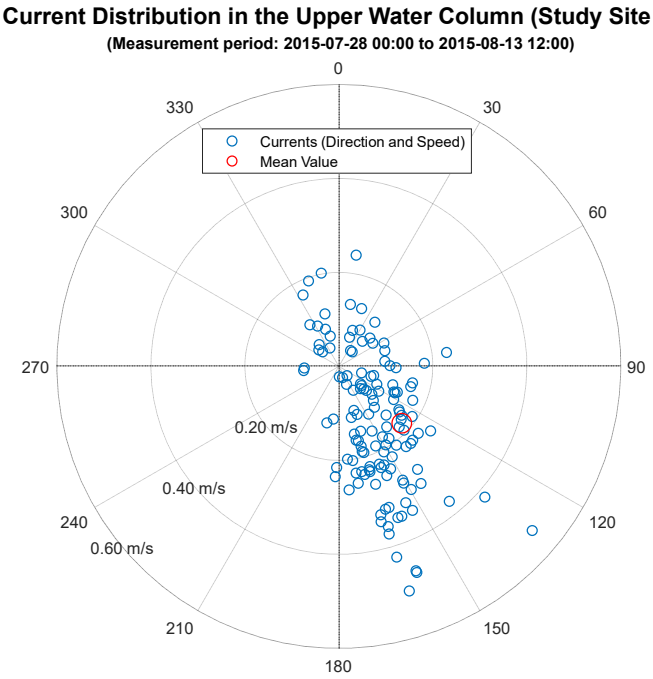

Figure 5-9: Current speed and direction for the upper water column, 9.59m to 10.59m above the seafloor. The measurement covers the period from the 28th of July at 0:00 the 13th of August at 15:00. The sensor was located at 69.558393°N 138.914445°W. Blue dots indicate 3 hourly means of actual measurements, while the red dot indicates the mean value in direction and speed. Current speed is in m/s and direction of flow in degree.

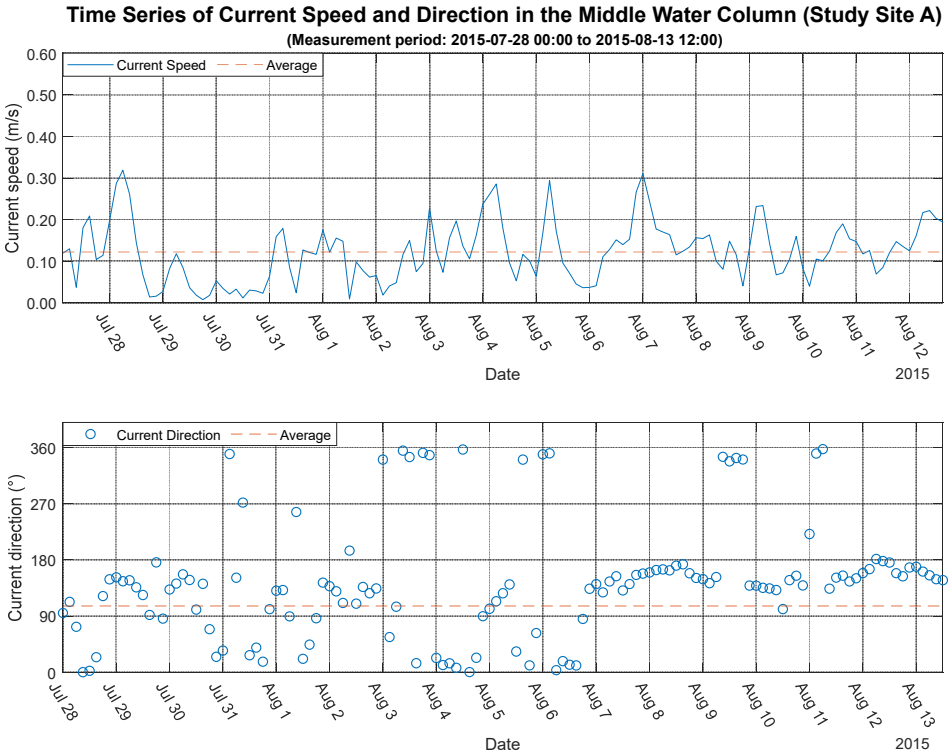

Figure 5-10: Current speed and direction for the mid water column, 2.59m to 9.59m above the seafloor. The values are 3-hourly means, measured with a 600kHz ADCP. The measurement period covers the period from the 28th of July 0:00 to the 13th of August 15:00 2015. The sensor was located at 69.558393°N 138.914445°W. Top - Blue line indicates the current speed, while the broken orange line shows the mean value for the period. Bot – The blue circles indicate the direction and the broken orange line indicates the mean direction over the measurement time.

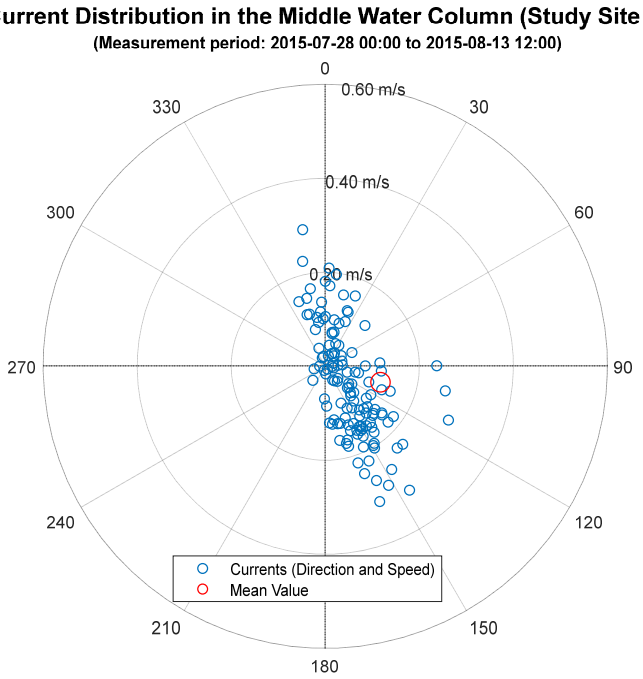

Figure 5-11: Current speed and direction for the mid water column, 2.59m to 9.59m above the seafloor. The measurement covers the period from the 28th of July at 0:00 the 13th of August at 15:00. The sensor was located at 69.558393°N 138.914445°W. Blue dots indicate 3 hourly means of actual measurements, while the red dot indicates the mean value in direction and speed. Current speed is in m/s and direction of flow in degree.

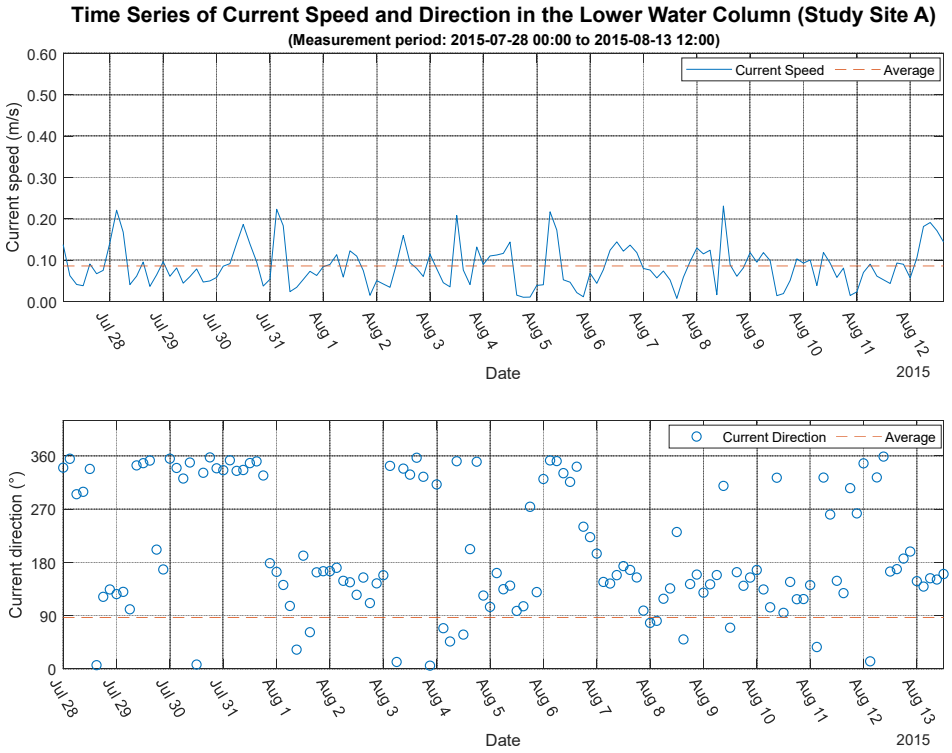

Figure 5-12: Current speed and direction for the lower water column, 1.59m to 2.59m above the seafloor. The values are 3-hourly means, measured with a 600kHz ADCP. The measurement period covers the period from the 28th of July 0:00 to the 13th of August 15:00 2015. The sensor was located at 69.558393°N 138.914445°W. Top - Blue line indicates the current speed, while the

broken orange line shows the mean value for the period. Bot – The blue circles indicate the direction and the broken orange line indicates the mean direction over the measurement time.

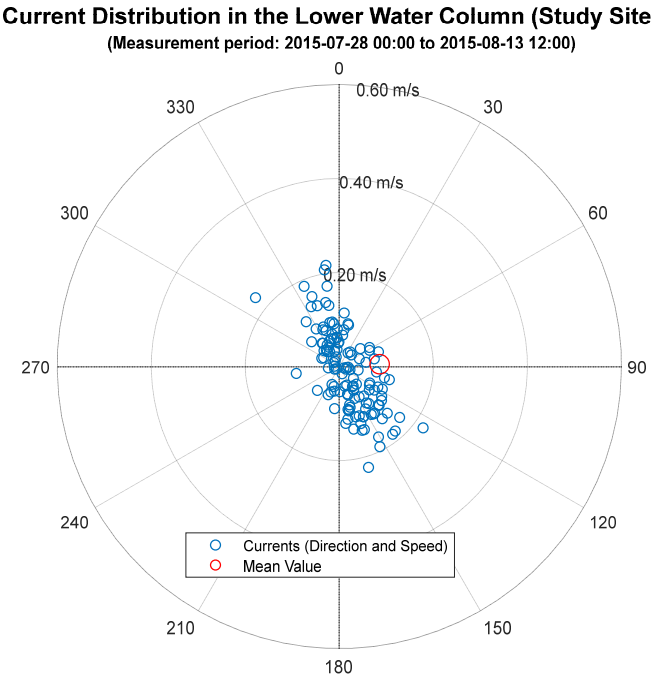

Figure 5-13: Current speed and direction for the lower water column, 1.59m to 2.59m above the seafloor. The measurement covers the period from the 28th of July at 0:00 the 13th of August at 15:00. The sensor was located at 69.558393°N 138.914445°W. Blue dots indicate 3 hourly means of actual measurements, while the red dot indicates the mean value in direction and speed. Current speed is in m/s and direction of flow in degree.

5.2 Results for Study Location B – Catton Point 2018

5.2.1 Wind

The wind speed and direction are obtained from the Herschel Island weather station in the measurement period from the 4th of August 2018 0:00 to the 18th of August 2018 15:00. The maximum wind speed recorded was 14.5 m/s (52.2 km/h) at the 17th of August 2018 0:00. The mean wind speed for the measurement period is 5.4 m/s (19.4 km/h), the median value 4.8 m/s (17.3 km/h). The lowest value occurred at the 16th of August 2018 18:00 with 0.7 m/s (2.5 km/h). The standard deviation for this data is 3.1 m/s (11.1 km/h).

Three storm events, following the arctic storm definition of Atkinson (2005), occurred. The first one covered the period from the 4th of August 18:00 to the 5th of August 6:00 and reached wind speeds of up to 13.7 m/s (49.3 km/h) with wind directions from 280 to 310 degree. The second storm occurred between the 14th of August 6:00 and 12:00 and reached 10.7 m/s (38.7 km/h) in peak with wind directions from 220 to 240 degree. The third storm occurred at the 17th of August between 0:00 and 12:00 and reached 14.5 m/s in peak with wind directions from 210 to 230 degree. The time series for this wind data is displayed in Figure 5-14.

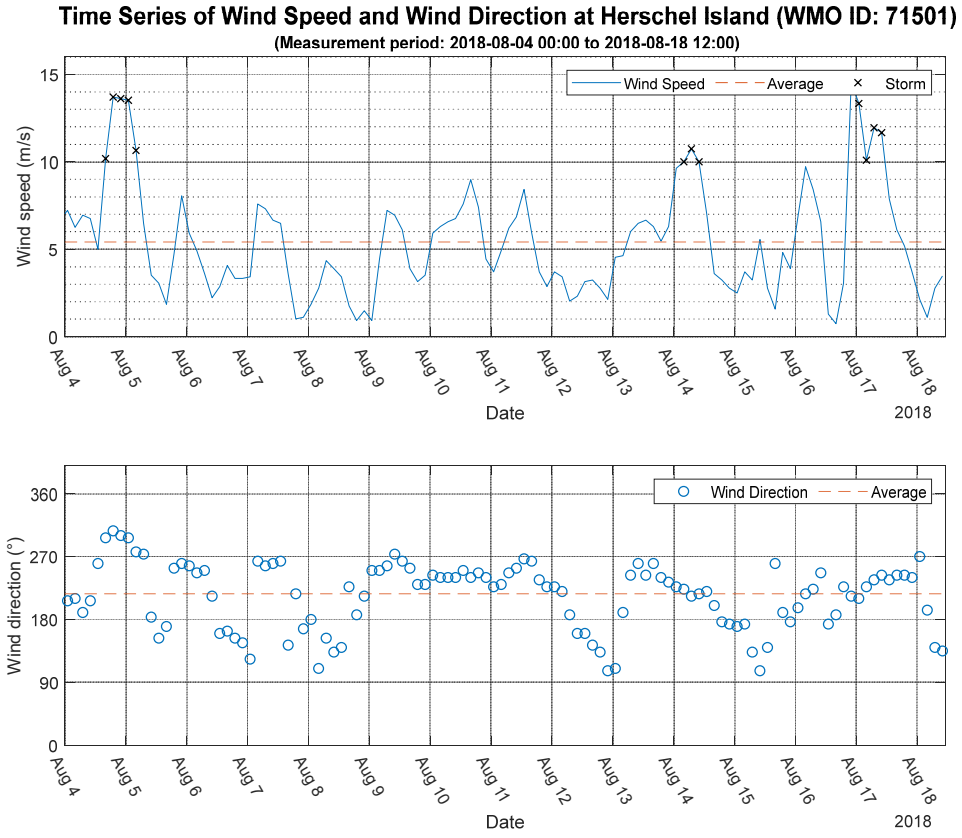

Figure 5-14: Top - Wind speed in the 2018 measurement period, obtained from the Herschel Island weather station (WMO ID: 71501). Blue line indicates wind speeds, the broken orange line indicates the mean value and black cross the storm events, following the arctic storm definition of Atkinson 2005 (at least 6 hours of at least 10 m/s wind speed). Bot – Wind direction in the 2018

measurement period, obtained from the Herschel Island weather station (WMO ID: 71501). Blue circles indicate wind direction, where the wind is coming from. The broken orange line indicates the mean wind direction in this period.

The wind direction varied from 107 (E) to 307 (NW) degree. The data indicates the direction the wind is coming from. The mean direction is 217 degree. In general, the wind is coming from SE to NW. The Figure 5-15 visualises the exclusively low to moderate wind speeds coming from E to S, the varying wind speed from south to west directions and exclusively high to very high wind speed from W to NW direction and a complete absence of wind coming from NW to E direction in a polar scatter plot.

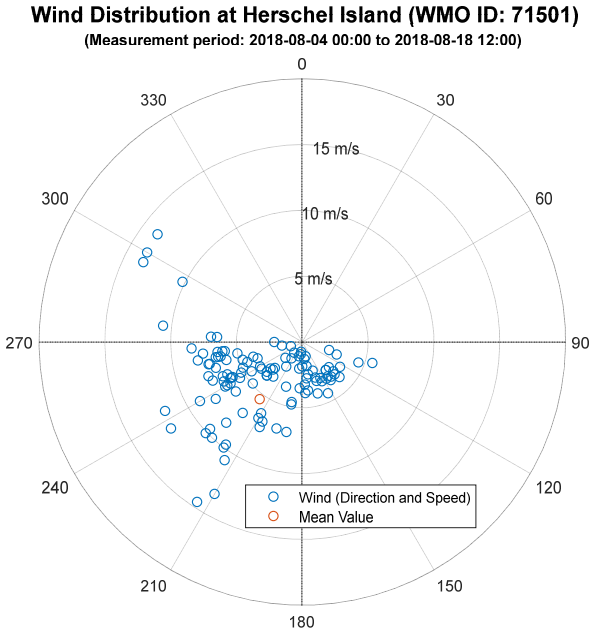

Figure 5-15: Polar scatter plot of wind direction and speed during the 2018 measurement period, recorded at the WMO station 71501 (Herschel Islands). Blue circles indicate wind direction in degree and wind speed in meter per second. The red circle is the mean direction and wind speed value in the measurement period.

5.2.2 Sea Ice – Directional Fetch

Directional fetch was calculated for the 2018 mooring period from the 4th of August 2018 0:00 to the 18th of August 2018 12:00. Within this period the direction from which the wind is blowing is taken and, in an angle preserving line (rhumb line), from the sensor location the distance to the next land or field of more than 20% sea ice was calculated.

The maximum calculated fetch in this period was 128 km occurring at the 13th of August 2018 at 0:00. The minimum value is 0 km occurring at times, where the sea ice with more

than 20% concentration was above the sensor. The mean fetch length within this period is 12 km. The median value is two 2 km. The standard deviation value for this data is 27 km. Extended periods of long fetch, above 100 km, occurred only between the 13th of August 2018 0:00 and 3:00. Between the 8th of August 2018 18:00 and the 12th of August 2018 09:00 the directional fetch length was very low (below 4 km). The whole time series of the directional fetch at the period is shown in Figure 5-16. In Figure 5-17, the average and the maximum potential fetch during the measurement period in every direction is displayed. On the left in a large scale, zoomed imagery and in a big picture scenery to the right. This Figure illustrates the wind directions with the highest potential to generate waves.

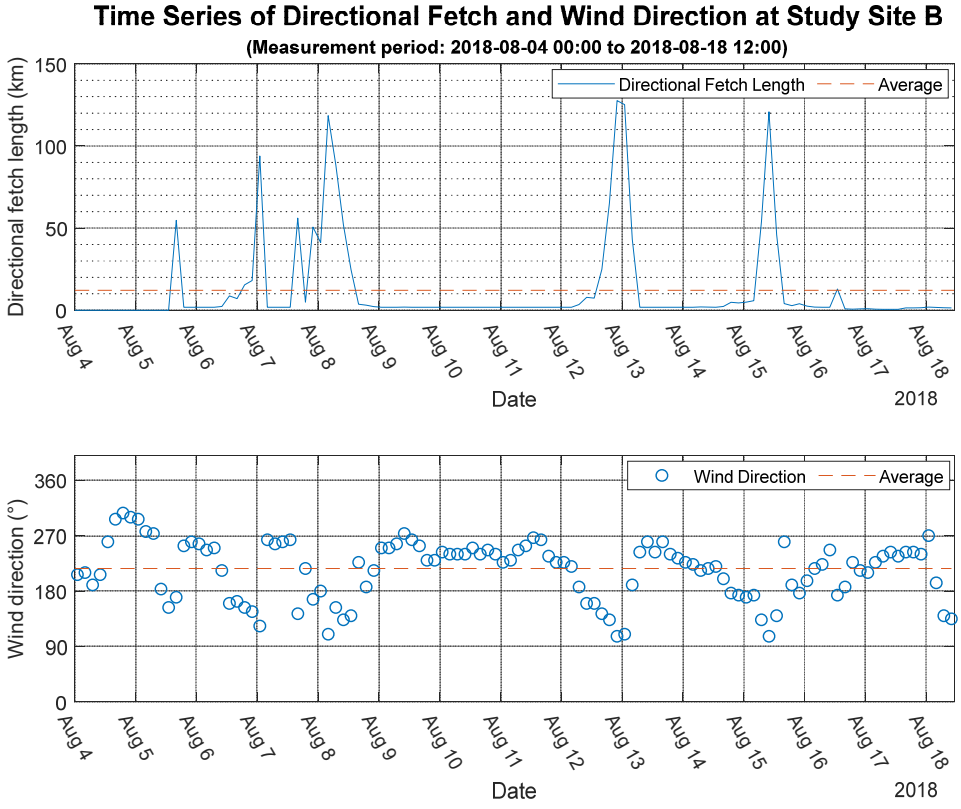

Figure 5-16: Top – Blue line indicates directional fetch in the 2018 measurement period at 3-hourly averaged values. This was calculated for the 2018 mooring site at 69.465833 °N / 139.030555 °W. Wind directions obtained from the Herschel Island weather station (WMO ID: 71501), were used to determine direction. Daily sea ice charts of the Canadian Ice Service and the GSHHG coastline data were used to determine the possible distance for wave generation in this direction. Orange line is the mean value line Bot – Wind direction in the 2018 measurement period, obtained from the Herschel Island weather station (WMO ID: 71501). Blue line indicates wind direction grouped in three hourly mean values. The orange line indicates the mean wind direction.

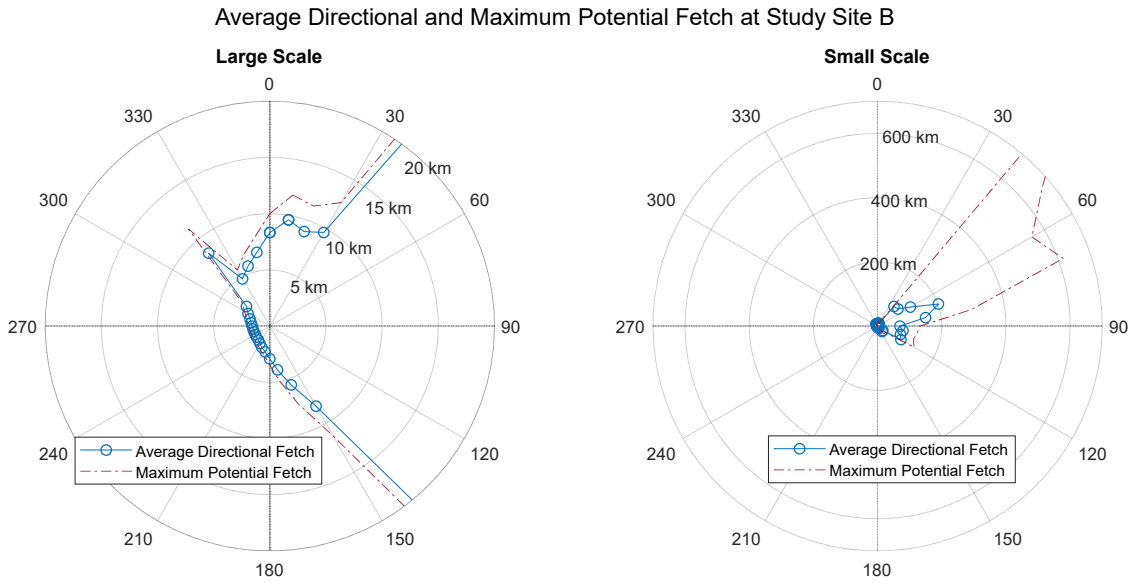

Figure 5-17: Polar plots of the average potential fetch and the maximum (no sea ice) fetch length in the 2018 measurement period. On this plot the sensor is "located" in the center of the plot. The average distance to the next wave blocking feature (land or sea ice with a concentration of more than 20%) in each direction in ten degree increments is shown. Daily sea ice charts of the Canadian Ice Service and the GSHHG coastline data were used, to determine the possible distance for wave generation in this direction. The left side and the right side plot show the same situation with different scales. Distance in km, direction (zero equals N).

5.2.3 Modelled Waves

The obtained data of the NOAA WAVEWATCH III® model covers the period from the 4th of August 2018 03:00 to the 18th of August 2018 12:00. The point of interest is at 69.4666°N 139.0001°W, which is the closest point to the mooring location in 2018. Within this period, the maximum calculated wave height is 0.62 m at the 16th of August 2018 21:00, the minimum value occurred at 15th of August 2018 15:00 with 0.04 m. The median value for the period is 0.23 m, the mean value 0.39 m with a standard deviation of 0.27 m.

Wave height events above 0.50 m were calculated for the period between the 4th of August 2018 15:00 and the 4th of August 2018 21:00, the 7th of August 2018 3:00, the 16th of August 2018 15:00 and the 17th of August 2018 3:00. The time series is shown in Figure 5-18.

Waves occurred from any directions, even though a two-fold pattern of higher wave events can be seen. Those higher waves occur between 310 and 339 degree and between 57 and 78 degree. The mean direction, where the waves are coming from is at 0 degree (N). The distribution of wave heights at the various direction can be found in Figure 5-19.

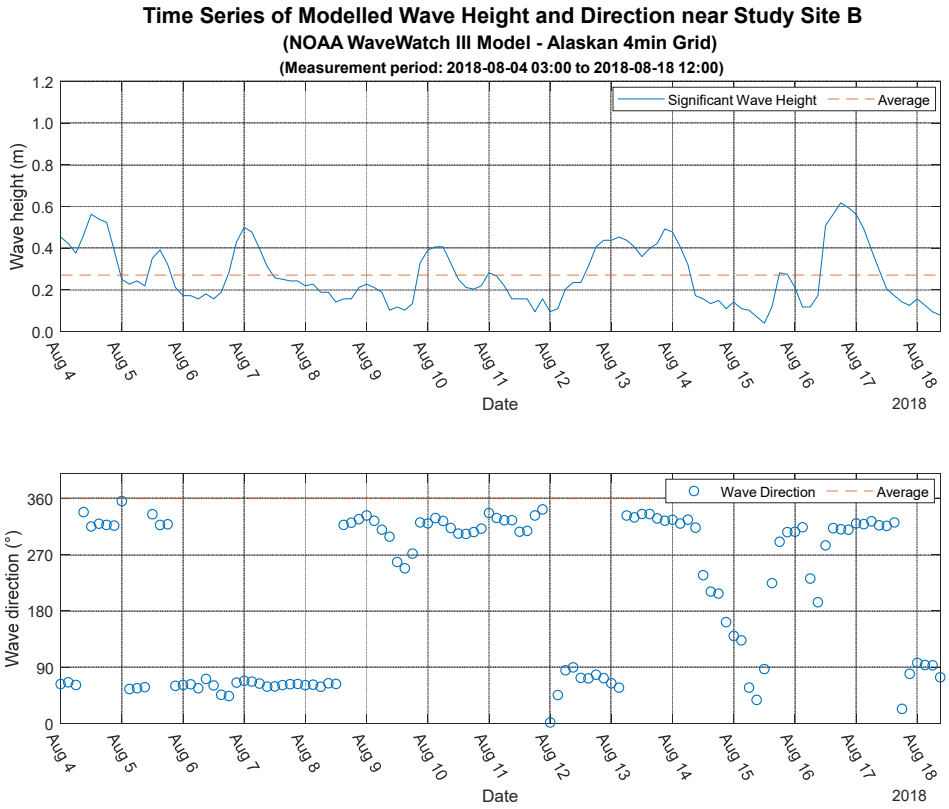

Figure 5-18: Top - Plot of the NOAA WAVEWATCH III® modelled wave heights at 69.4666°N and 139.0001°W. Broken red line indicates the mean value. Bot - NOAA WAVEWATCH III® modelled wave directions, coming from (meteorological convention), for the same grid point. Broken red line indicates the mean value.

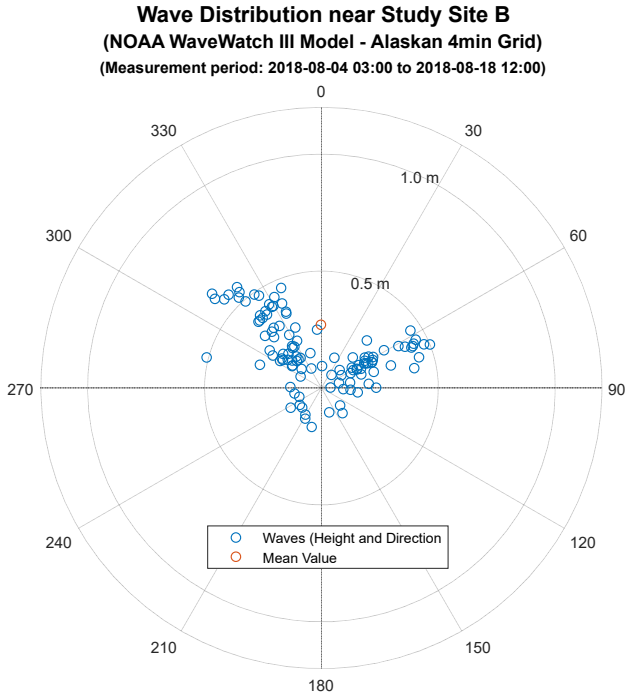

Figure 5-19: Polar scatter plot of the NOAA WAVEWATCH III® modelled wave heights and directions (meteorological convention) at 69.4666 N and 139.0001 W. Red circle indicates the mean value in wave direction and wave height.

5.2.4 Measured Waves

In 2018 nondirectional waves were measured using a RBRsolo³ D |wave16 sensor, that was located at 69.46583°N 139.03055°W. The measurement covers the period from the 4th of August 2018 03:00 to the 18th of August 2018 12:00. The maximum wave height occurred at the 7th of August 2018 15:00 and reached 0.49 m. Minimum wave height occurred at the 18th of August 2018 03:00 0.00 with 0.00 m. Mean value is 0.07 m, median value is 0.03 m. Standard deviation within this period is 0.09 m.

Waves higher than 0.15 m were recorded at the 5th of August 2018 21:00 with 0.17 m and at the 14th of August 2018 between 03:00 to 06:00 with 0.15 to 0.18 m. Additionally, between the 7th of August 2018 12:00 and the 8th of August 3:00, where wave heights from 0.17 to 0.48 m were recorded, being the largest waves in this period. An extended period of exceptionally low wave heights is from the 9th of August 2018 06:00 to the 13th of August 2018 0:00, within this 90-hour long period waves did not exceed 0.05 m. Another period where wave heights did not exceed 0.035 m was 54h long and spanned from the 14th of August 2018 21:00 to the 17th of August 2018 03:00. In total, 74.1% of the wave heights were below 0.10 m and 25.9% of the waves were between 0.10 to 0.50 m. Time series of wave height is visualised in Figure 5-20.

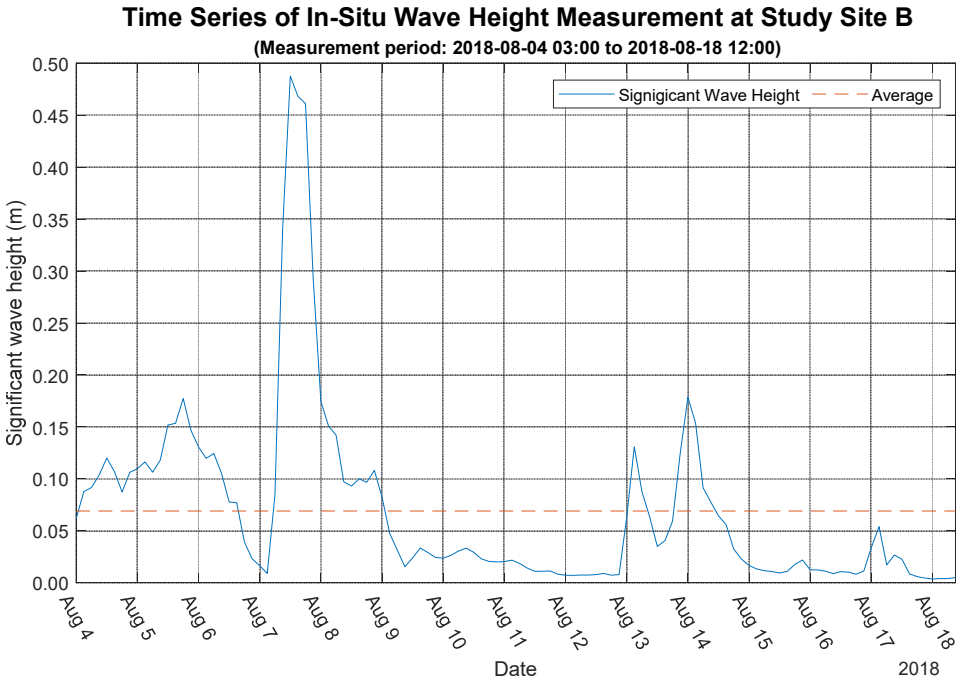

Figure 5-20: Nondirectional wave height measurement obtained with a RBRsolo³ D|wave16 sensor, that was located at 69.46583°N 139.03055°W from the 4th of August 2018 03:00 to the 18th of August 2018 12:00. Broken red line indicates the mean value for the measurement period.

5.2.5 Measured Sea Level

The sea level was measured using a RBRsolo³ D |wave16 sensor, that was located at 69.46583°N 139.03055°W. The measurement covers the period from the 4th of August 2018 03:00 to the 18th of August 2018 12:00. Within this period maximum sea level was 7.29 m, minimum water depth is 6.61 m. The mean water depth is 6.87 m, median is 6.85 meter. The standard deviation for the data is 0.14 m. The data shows a cyclic structure, where every six hours a local minima or maxima is reached. Time series of water depth is illustrated at Figure 5-21.

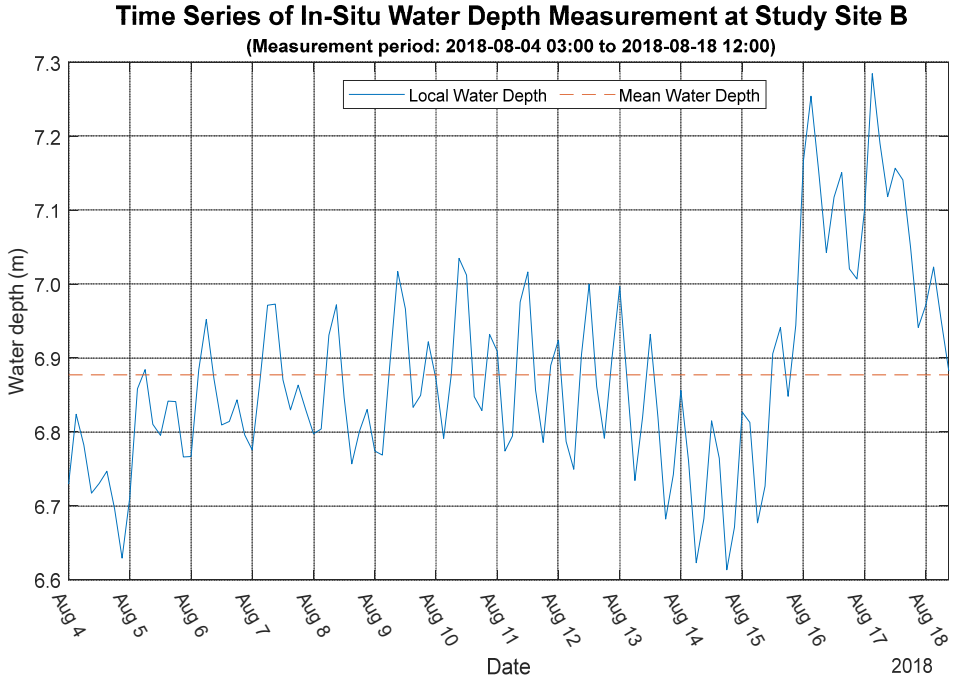

Figure 5-21: Water depth derived from RBRsolo³ D |wave16 measurements at sensor location (69.46583°N 139.03055°W). Measurement period is from the 4th of August 2018 3:00 to the 18th of August 2018 12:00. Broken red line shows the mean water depth.

5.2.6 Stratification

The stratification was measured two times within the 2018 mooring period. The first measurement took place at the 9th of August 2018 16:24, located at 69.4651 °N 139.0306 °W. It measured 23 times within one cast every 30 cm or so, started at 0.15 m and ended at 6.83 m water depth. Salinity in ppt and temperature in °C are extracted from the cast. Within this depth profile, the minimum salinity was 20.22 ppt at 0.15 m water depth, maximum salinity was 24.17 ppt at 6.83 m water depth. At this cast the mean salinity was at 22.11 ppt. The minimum temperature of 3.21°C was at 6.83 m water depth. The maximum temperature was 3.61°C at 0.15 m water depth. Mean temperature at this cast is 3.45°C.

The second measurement took place at the 11th of August 2018 15:46. The location of this measurement was 69.4645 °N and 139.0279 °W. It measured 24 times within one cast every 30 cm or so, started at 0.15 m and ended at 7.04 m water depth. The maximum salinity in this cast was 21.38 ppt occurring at 7.04 m water depth. The minimum salinity was 16.69 ppt at 0.15 m water depth. The mean salinity is 18.79 ppt. The minimum temperature was 4.37°C at 2.56 m water depth. Maximum water temperature was 5.21°C in 5.57 m water depth. The mean temperature 4.62 °C at this cast. The profiles are visualized in Figure 5-22.

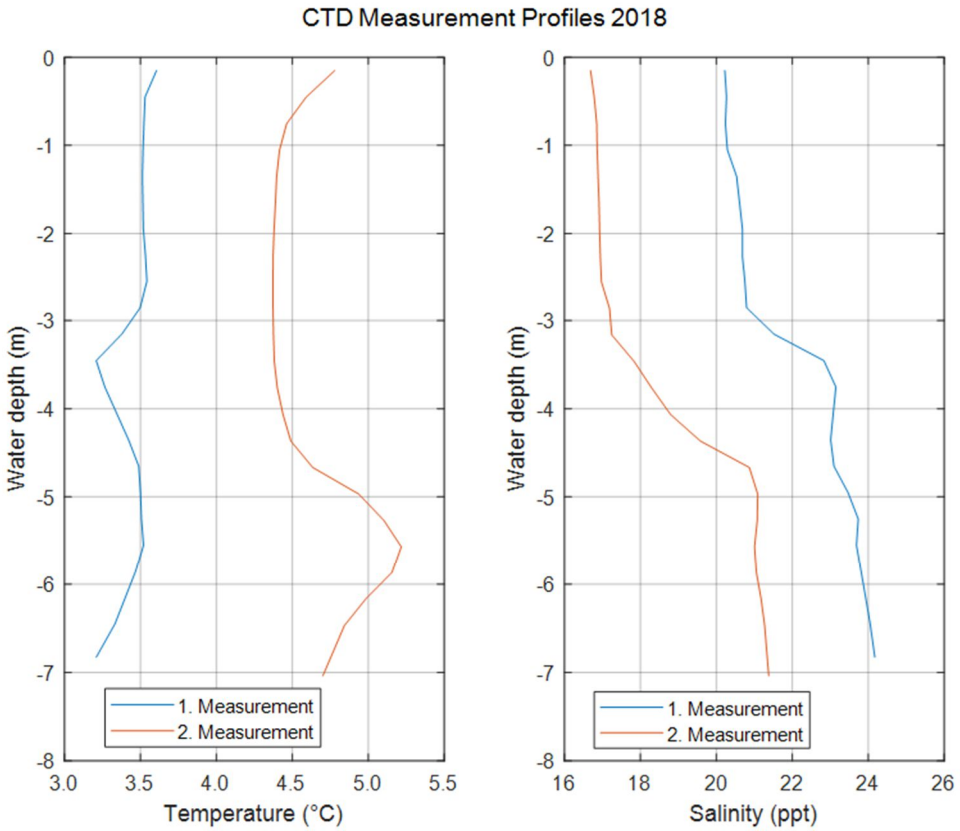

Figure 5-22: CastAway®-CTD measurement profiles in the 2018 mooring period. On the left side depth profiles for temperature (in degree Celsius). On the right side depth profiles for salinity (in parts per thousand). The first measurement was at the 9th of August 2018 16:24 at 69.4651°N 139.0306°W. The second took place at the 11th of August at 15:46, located at 69.4645°N 139.0279°W.

5.2.7 Currents

Current measurement in 2018 started at the 4th of August 2018 0:00 and ended at the 18th of August 2018 12:00. The data is divided into upper, mid and lower column currents. The upper column contains the averaged two-topmost nonremoved bins, the lower column, the averaged two lowest layers, and the mid column the four bins in between. Each bin is 0.50

m wide. Due to the sensor configuration the lower bin starts at 1.59 m above the seafloor and ends at 2.59 m. The middle layer starts at 2.59 m and ends at 4.59 m above the seafloor. The upper most one starts at 4.59 meter and ends at 5.59 m above the seafloor, which is 1.29 m below the average water level in the mooring period.

In the upper column the mean flow speed in the measurement period is 0.16 m/s and median value is 0.14 m/s. The minimal flow speed occurred at the 10th of August 03:00 and was 0.02 m/s. The maximum flow speed occurred at the 6th of August 03:00 and was 0.57 m/s. The standard deviation within the period is 0.11 m/s. In total, 35.0% of the time the current speed was below 0.10 m/s, 38.5 % of the time between 0.10 and 0.20 m/s and 15.4 % of the time between 0.20 and 0.30 m/s. Current speed exceeded 0.30 m/s for 11.1 % of the period.

In the upper water column, flow of speed below 0.10 m/s is in nearly all directions directed. Currents where the speed exceeds 0.10 m/s occur only at directions between 23 and 56degree, between 185 and 269 degree. From 202 to 234 degree, current with flow speed greater than 0.20 m/s occurred. The mean direction within the upper column is 225 degree. The time series for the current speed and direction for the upper column can be found in Figure 5-23. The distribution of currents speeds per direction for the upper column in the polar scatter plot at Figure 5-24.

In the mid column the mean flow speed in the measurement period is 0.11 m/s and the median value is 0.08 m/s. The flow speed was minimal at the 17th of August 09:00 with 0.00 m/s. The maximum flow speed occurred at the 6th of August 03:00 with 0.42 m/s. The standard deviation within the period is 0.08 m/s. In total, the current speed is less than 0.10 m/s at 64.1 % of the time. 26.5 % of the period the flow was between 0.10 and 0.20 m/s. Higher speed between 0.20 m/s and 0.30 m/s occurred at 6.0 % of the time, 3.4 % of the time the current speed exceeded 0.30 m/s.

In the mid column, currents of speeds below occur everywhere but from 99 to 171 degree. Current speed that exceeded 0.10 m/s occurred from 8 to 55 degree and from 209 to 253 degree. Current speed that exceeded 0.20 m/s occurred from 217 230 degree. Mean direction is at 350 degree. The time series for the current speed and direction for the mid column can be found in Figure 5-25. The distribution of current speed per direction for the mid column in the polar scatter plot at Figure 5-26.

In the lower column the mean flow speed in the measurement period was 0.11 m/s and the median value 0.09 m/s. The minimal flow speed was 0.00 m/s occurring at the 4th of August 03:00. The maximum flow speed occurred at the 11th of August 03:00 was 0.28 m/s. The standard deviation within the period was 0.07 m/s. The current speed was below 0.10 m/s

for 52.1 % of the time. Current speeds between 0.10 and 0.20 m/s occur at 34.2 %. Current speeds exceeding 0.20 m/s occur at 13.7 % of the time.

In the lower column, current speeds below 0.10 m/s occur at nearly all directions. Directions were the speed exceeds 0.10 m/s are from 8 to 71 degree, from 218 to 250 degree, and from 287 to 319 degree. Current speeds where the speed exceeds 0.20 m/s occur from 24 to 47 degree and between 216 and 240 degree. The mean direction is at 17 degree. The time series for the current speeds and directions for the lower column can be found in Figure 5-27. The distribution of currents speed per direction for the lower column is shown in the polar scatter plot at Figure 5-28.

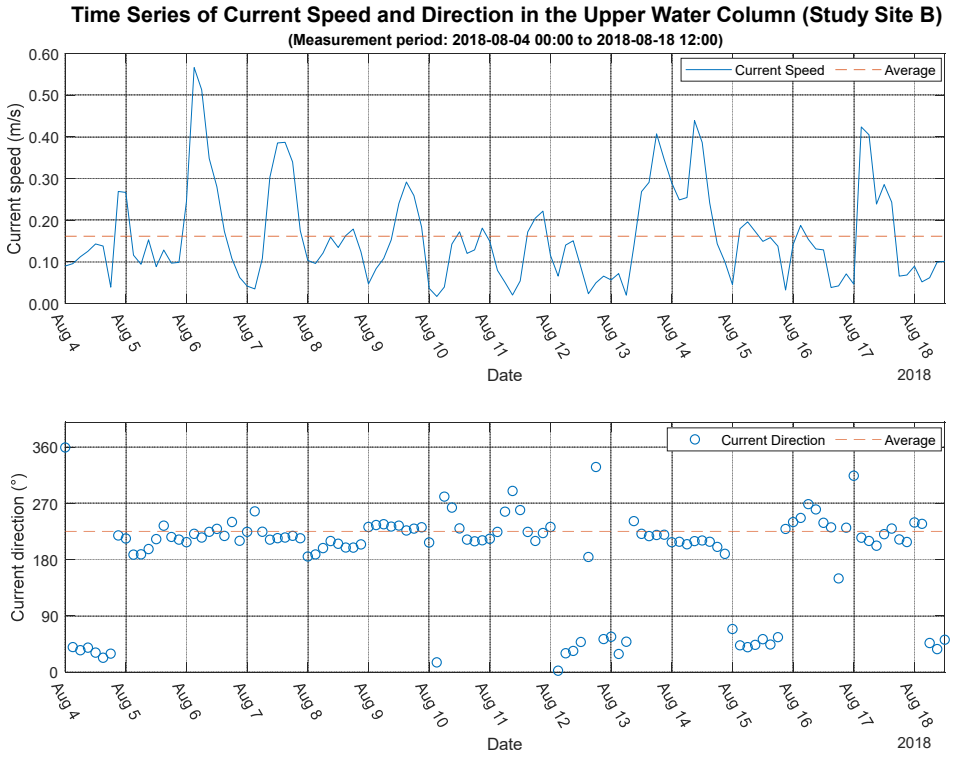

Figure 5-23: Current speeds and directions for the upper water column, 4.59m to 5.59m above the seafloor. The values are 3-hourly means, measured with a 600kHz ADCP. The measurement period covers the period from the 4th of August 2018 0:00 to the 18th of August 2018 12:00. The sensor was located at 69.465833°N 139.030555°W. Top - Blue line indicates the current speed, while the broken orange line shows the mean value for the period. Bot – The blue circles indicate the direction and the broken orange line indicates the mean direction over the measurement time.

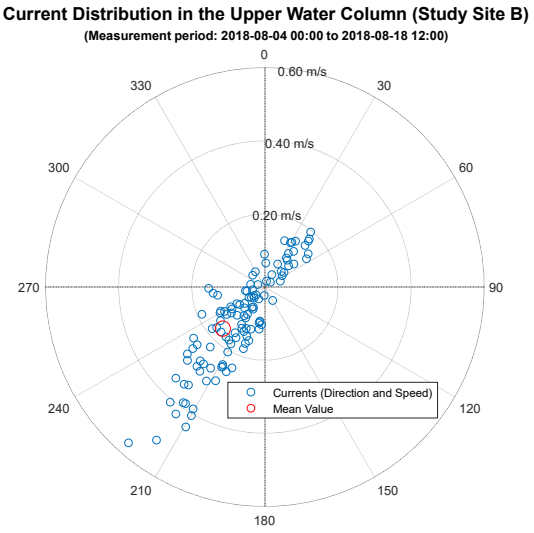

Figure 5-24 Current speed and direction for the upper water column, 4.59m to 5.59m above the seafloor measured with a 600kHz ADCP. The measurement period covers the period the 4th of August 2018 0:00 to the 18th of August 2018 12:00. The sensor was located at 69.465833°N 139.030555°W. Blue dots indicate 3 hourly means of actual measurements, while the red dot indicates the mean value in direction and speed. Current speed is in m/s and direction of flow in degree.

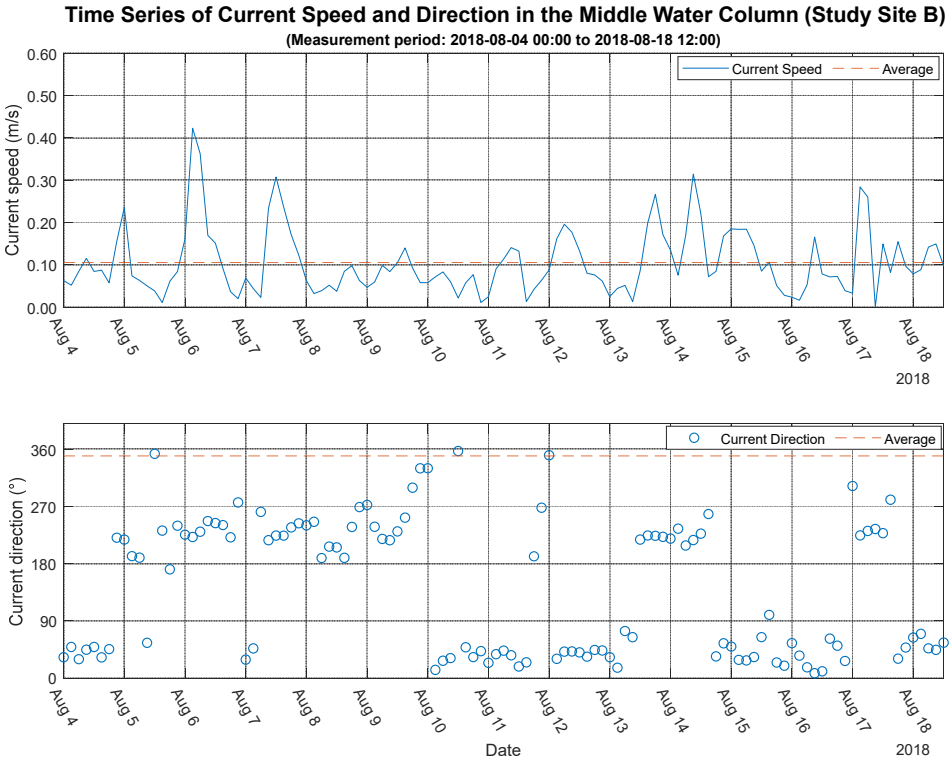

Figure 5-25: Current speeds and directions for the mid water column, 2.59m to 4.59m above the seafloor. The values are 3-hourly means, measured with a 600kHz ADCP. The measurement period covers the period from the 4th of August 2018 0:00 to the 18th of August 2018 12:00. The sensor was located at 69.465833°N 139.030555°W. Top - Blue line indicates the current speed, while the broken orange line shows the mean value for the period. Bot – The blue circles indicate the direction and the broken orange line indicates the mean direction over the measurement time.

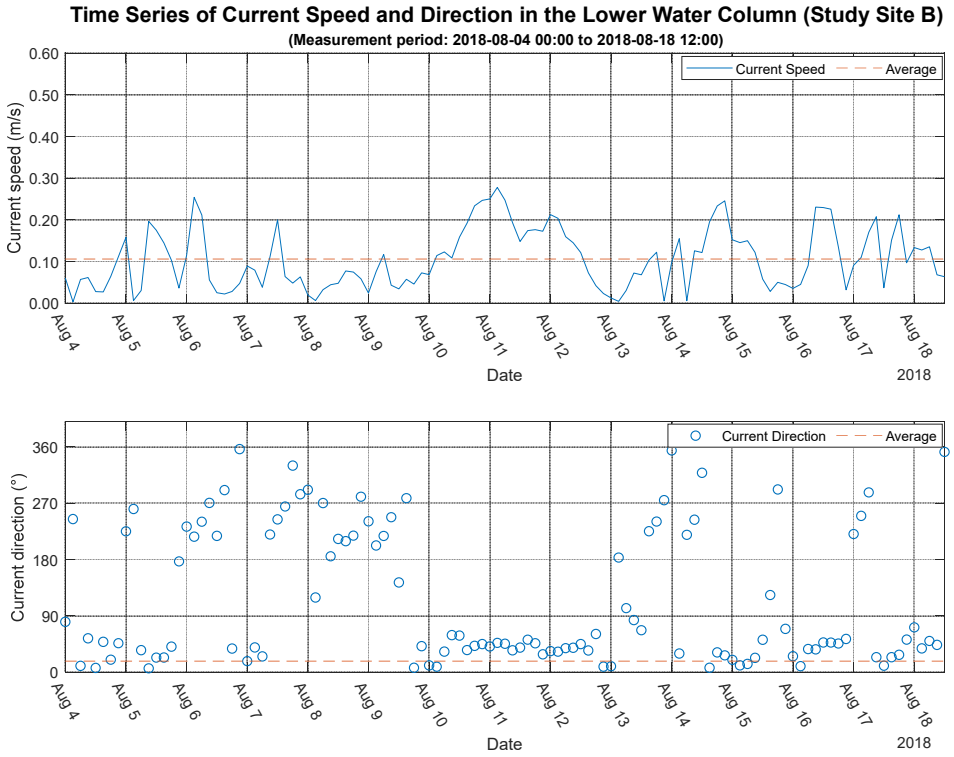

Figure 5-26: Current speed and direction for the mid water column, 2.59m to 4.59m above the seafloor measured with a 600kHz ADCP. The measurement period covers the period the 4th of August 2018 0:00 to the 18th of August 2018 12:00. The sensor was located at 69.465833°N 139.030555°W. Blue dots indicate 3 hourly means of actual measurements, while the red dot indicates the mean value in direction and speed. Current speed is in m/s and direction of flow in degree.

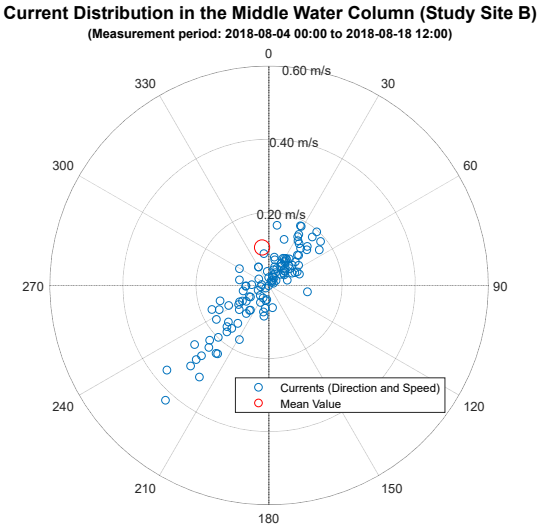

Figure 5-27: Current speeds and directions for the lower water column, 2.59m to 4.59m above the seafloor. The measurement period spans from the 4th of August 2018 0:00 to the 18th of August 2018 12:00. The sensor was located at 69.465833 °N 139.030555 °W. Top - Blue line indicates 3-hourly means of current speeds, while the orange line shows the mean value for the period. Bot – The blue line indicates the 3-hourly means of direction values and the orange line indicates the mean direction over the measurement time.

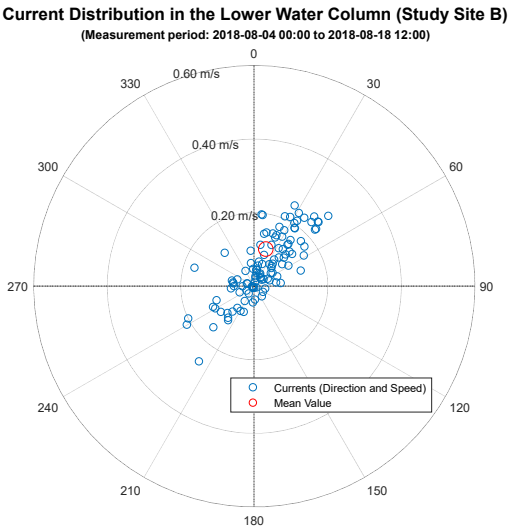

Figure 5-28: Current speed and direction for the lower water column, 1.59m to 2.59m above the seafloor measured with a 600kHz ADCP. The measurement period covers the period the 4th of August 2018 0:00 to the 18th of August 2018 12:00. The sensor was located at 69.465833°N 139.030555°W. Blue dots indicate 3 hourly means of actual measurements, while the red dot indicates the mean value in direction and speed. Current speed is in m/s and direction of flow in degree.

5.3 Statistical Relationship – Study Location A – 2015

The goal of this section is to determine the grade of correlation of the potential environmental forcing parameter wind and waves towards currents. It aims to give a statistical base for interpreting the potential relationship between the forcing parameter and the currents, divided into the upper, mid and bottom column. For simplicity reasons, the focus is on the relationship to current speed rather than direction. In Figure 5-29, a combination of the environmental forcing parameter and the current speed is shown.

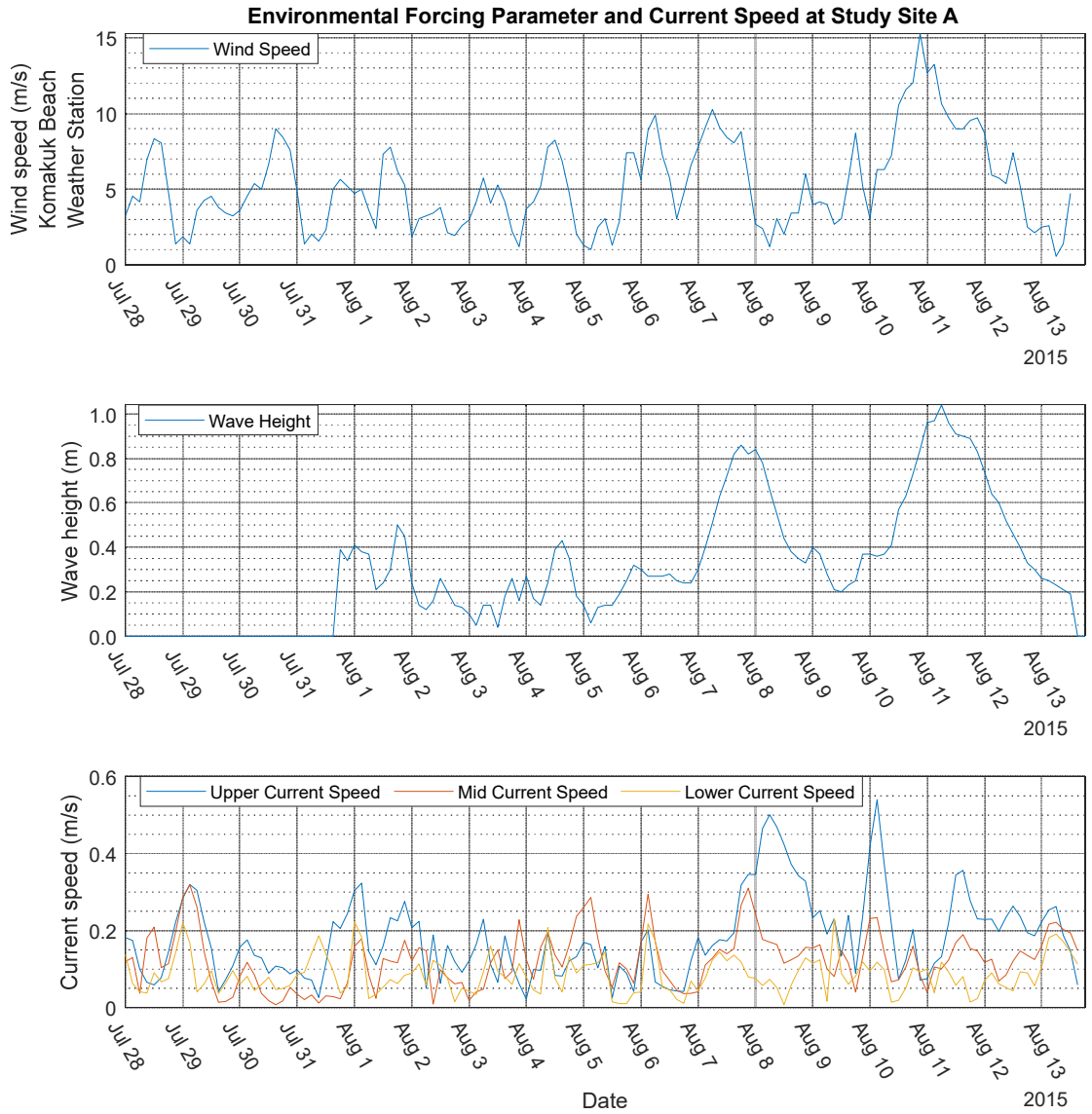

Figure 5-29: Multiplot of environmental forcing parameter and current speeds. Top: Wind speed in m/s in the 2015 measurement period from the 28th of July 2015 to the 13th of August 2015, obtained from the Komakuk Beach weather station (WMO ID: 71046). Mid: NOAA WAVEWATCH III® modelled wave height in m at 69.533°N and 138.867°W. Data period is from the 31st of July 2015 18:00 to the 13th of August 2015 12:00. Bot: Current speed in m/s, for the upper water column (9.59m to 10.59m above the seafloor) in blue, mid water column (2.59m to 9.59 m above the seafloor) in red and the lower water column (1.59 m to 2.59m above the seafloor) in yellow. The measurement covers the period from the 28th of July at 0:00 the 13th of August at 15:00. The 600kHz ADCP was located at 69.558393 °N 138.914445 °W.

5.3.1 Wind Speed and Current Speed

Wind speed is a main driver for the generation of coastal currents throughout the water column. To link those two in this study, the wind speed is combined with the adjacent current speed, in the upper, middle and lower water column. The scatter plot serves as reflection of the potential correlation of the parameter. The correlation of wind speed and upper column current speed can be found in Figure 5-30.

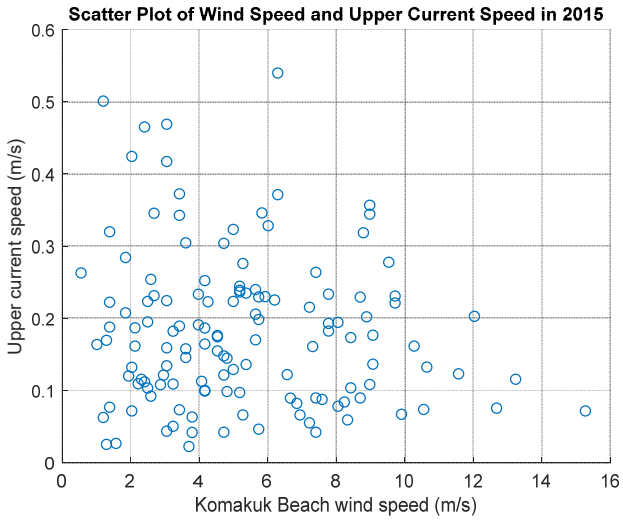

Figure 5-30: Scatter plot of wind speed in (m/s) in the 2015 measurement period from the 28th of July at 0:00 the 13th of August at 15:00, obtained from the Komakuk Beach weather station (WMO ID: 71046) and the currents of the upper water column (9.59m to 10.59m above the seafloor), obtained using ADCP measurements from the 28th of July at 0:00 the 13th of August at 15:00. The ADCP was located at 69.558393°N 138.914445°W.

The Figure 5-30 illustrates that no linear correlation can be found between the two parameters. This is also reflected in the coefficient of determination (R^2) that is at 0.01 at a sample size of 133. In Figure 5-31 the correlation of wind speed and mid column current

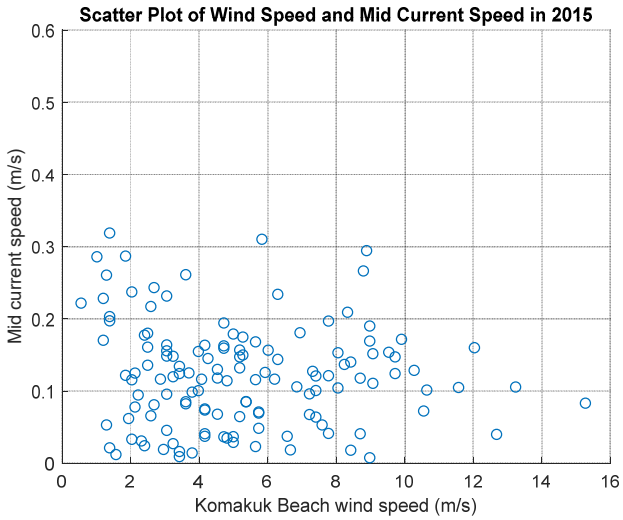

Figure 5-31: Scatter plot of wind speed in meter per second in the 2015 measurement period from the 28th of July at 0:00 the 13th of August at 15:00, obtained from the Komakuk Beach weather station (WMO ID: 71046) and the currents of the mid water column (2.59m to 9.59m above the seafloor), obtained using in-situ ADCP measurements from the 28th of July at 0:00 the 13th of August at 15:00. The ADCP was located at 69.558393°N 138.914445°W.

speed is displayed. For this plot a linear correlation is also not visible in the scatter plot. This is also indicated by the very low R^2 value, which is 0.01 with a sample size of 133.In the third plot of this set, Figure 5-32, the correlation of wind speed and lower water column is displayed, plot shows no linear correlation, also reflected in the low R^2 of 0.01 with a sample size of 133.

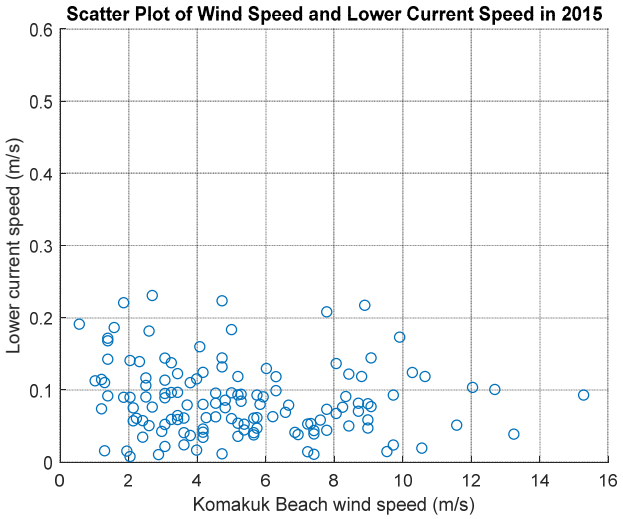

Figure 5-32: Scatter plot of wind speed in meter per second in the 2015 measurement period from the 28th of July 2015 to the 13th of August 2015, obtained from the Komakuk Beach weather station (WMO ID: 71046) and the currents of the lower water column (1.59m to 2.59m above the seafloor), obtained using in-situ ADCP measurements from the 28th of July at 0:00 the 13th of August at 15:00. The ADCP was located at 69.558393°N 138.914445°W.

All three plots show a broad scatter of the data and no significant linear correlation. Indicating that at the study site A in 2015 the current speed throughout the water column did not responded linear to the wind speed, measured in circa 50 km distance at the Komakuk Beach weather station, the closest official available WMO station.

To overcome the potential effect of different response to wind from different wind directions, the wind is categorized in eight directions. The directions are north from 337.5 to 22.5 degree, northeast from 22.5 degree to 67.5 degree, east from 67.5 degree to 112.5 degree, southeast from 112.5 degree to 157.5 degree, south from 157.5 degree to 202.5 degree, southwest from 202.5 degree to 247.5 degree, west from 247.5 degree to 292.5 degree and northwest from 292.5 degree to 337.5 degree.

In the next three Figures, the correlation of wind speed and current speed of the upper column, mid column and bottom column, additional the direction, where the wind is coming from is indicated. As the data period is limited, specific wind directions occurred more often than other ones. In Figure 5-33 the correlation of wind speed and upper column current speed is displayed, sorted by wind direction.

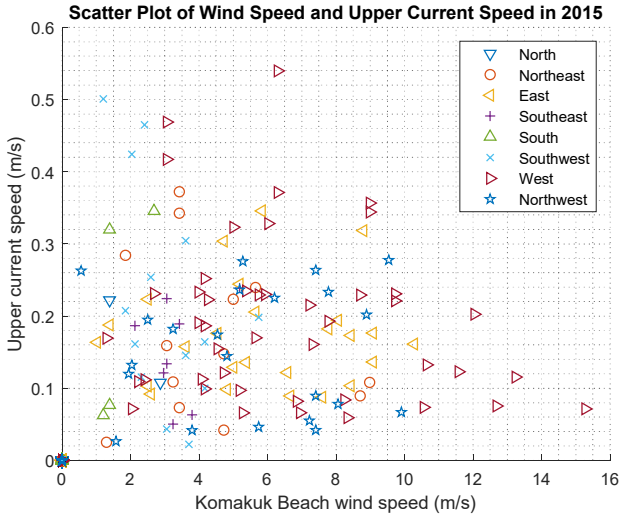

Figure 5-33: Scatter plot of wind speed in meter per second in the 2015 measurement period from the 28th of July 2015 to the 13th of August 2015, obtained from the Komakuk Beach weather station (WMO ID: 71046) and the currents of the upper water column (9.59m to 10.59m above the seafloor), obtained using in-situ ADCP measurements from the 28th of July at 0:00 the 13th of August at 15:00. The ADCP was located at 69.558393 °N 138.914445 °W. The data points are symbolized using the symbols in the legend in the upper right corner. The wind direction is divided into eight categories.

The correlation for the upper column current speed and wind speed is calculated for wind directions that have more than ten appearances. This is to avoid a too small sample size to bias the statistic. The coefficient of determination (R^2) is 0.035 for northeast winds that appear 13 times, 0.00 for east that appear 25 times, 0.231 for southwest that appear 14 times, 0.037 for west that appear 45 times,0.00 for northwest that appear 22 times. The wind direction north, southeast and south are not considered to a too low sample size. The coefficients of determination for the other directions show that no wind direction has a linear correlation between the upper column current speed and the wind speed.

In Figure 5-34 the correlation of wind speed and mid column current speed is displayed, sorted by wind direction. The correlation for the mid column current speed and wind speed is calculated for wind directions that have more than ten appearances. This is to avoid a too small sample size to bias the statistic. The coefficient of determination (R^2) is 0.16 for northeast winds that appear 13 times, 0.041 for east that appear 25 times, 0.083 for southwest that appear 14 times, 0.009 for west that appear 45 times,0.02 for northwest that appear 22 times. The wind direction north, southeast and south are not considered to a too low sample size. The coefficients of determination for the other directions show that no wind direction has a linear correlation between the mid column current speed and the wind speed.

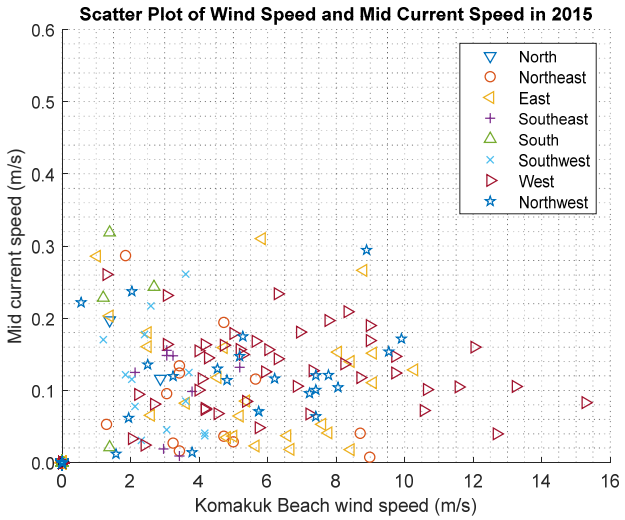

Figure 5-34: Scatter plot of wind speed in meter per second in the 2015 measurement period from the 28th of July 2015 to the 13th of August 2015, obtained from the Komakuk Beach weather station (WMO ID: 71046) and the currents of the mid water column (2.59m to 9.59m above the seafloor), obtained using in-situ ADCP measurements from the 28th of July at 0:00 the 13th of August at 15:00. The ADCP was located at 69.558393 °N 138.914445 °W. The data points are symbolized using the symbols in the legend in the upper right corner. The wind direction is divided into eight categories.

In Figure 5-35 the correlation of wind speed and lower column current speed is displayed, sorted by wind direction. The correlation for the lower column current speed and wind speed is calculated for wind directions that have more than ten appearances. This is to avoid a too small sample size to bias the statistic. The coefficient of determination (R^2) is 0.066 for northeast winds that appear 13 times, 0.0046 for east that appear 25 times, 0.072 for southwest that appear 14 times, 0.035 for west that appear 45 times,0.03 for northwest that appear 22 times. The wind direction north, southeast and south are not considered to a too low sample size. The coefficients of determination for the other directions show that no wind

direction has a linear correlation between the lower column current speed and the wind speed.

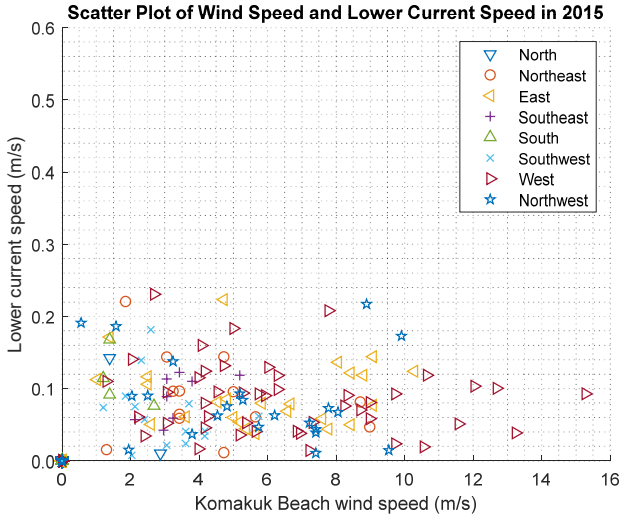

Figure 5-35: Scatter plot of wind speed in meter per second in the 2015 measurement period from the 28th of July 2015 to the 13th of August 2015, obtained from the Komakuk Beach weather station (WMO ID: 71046) and the currents of the lower water column (1.59m to 2.59m above the seafloor), obtained using in-situ ADCP measurements from the 28th of July at 0:00 the 13th of August at 15:00. The ADCP was located at 69.558393 °N 138.914445 °W. The data points are symbolized using the symbols in the legend in the upper right corner. The wind direction is divided into eight categories.

The sorting via the wind direction brought no linear correlation between the speed of the different columns of the current and the wind speed, as shown in the coefficients of correlation where the highest number is 0.23, which is still very low and displays no linear correlation in the statistical sense of linear correlation.

To overcome the potential effect, that the categorical wind directions may not necessarily reflect the wind directions that have a large potential fetch, and so have more potential to generate large wave and current action, a new sorting is done. To do so the data is divided into upper, mid and lower column current speed and the wind speed into no fetch, small fetch and large fetch.

For this the average fetch for the different directions is used, that are calculated and used in chapter 5.1.2. The large fetch direction is here defined as wind directions, where directional fetch directions wind coming from directions between 70 degree and 190 degree clockwise, this are the directions where the fetch is at least 15 kilometre in average.

The small fetch are the directions between 190 and 270 degree, where the average potential directional fetch is between 15 and three kilometres, no fetch directions (below three kilometre) are the directions between 270 and 70 degree clockwise. The Figure 5-36 show the correlation of upper column current speed and wind speed sorted by the fetch categories just mentioned.

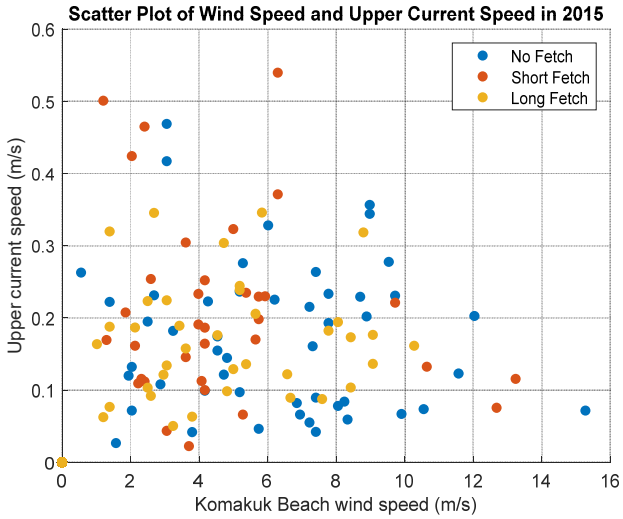

Figure 5-36: Scatter plot of wind speed in meter per second in the 2015 measurement period from the 28th of July 2015 to the 13th of August 2015, obtained from the Komakuk Beach weather station (WMO ID: 71046) and the currents of the upper water column (9.59m to 10.59m above the seafloor), obtained using in-situ ADCP measurements from the 28th of July at 0:00 the 13th of August at 15:00. The ADCP was located at 69.558393 °N 138.914445 °W. The data points are symbolized using the symbols in the legend in the upper right corner. No fetch is defined as directional fetch below 3 km, short fetch as between 3 and 15km and long fetch everything above 15km.

The R^2 value for the upper column speed and wind speed at large fetch conditions is 0.00 with a sample size of 37. The R^2 value for the upper column speed and wind speed at small fetch conditions is 0.03 with a sample size of 34. The R^2 value for the upper column speed and wind speed at no fetch conditions is 0.01 at 49 occurrences. The Figure 5-37 show the correlation of mid column current speed and wind speed sorted by the fetch categories. The R^2 value for the mid column speed and wind speed at large fetch conditions is 0.06 with a sample size of 37. The R^2 value for the mid column speed and wind speed at small fetch conditions is 0.03 with a sample size of 34. The R^2 value for the mid column speed and wind speed at no fetch conditions is 0.00 at 49 occurrences.

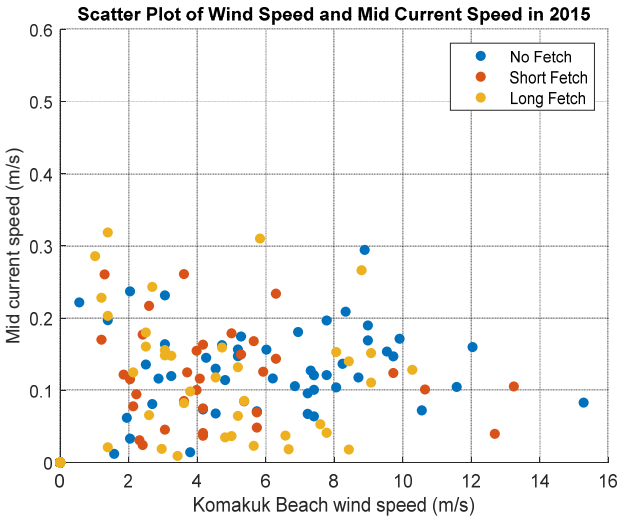

Figure 5-37: Scatter plot of wind speed in meter per second in the 2015 measurement period from the 28th of July 2015 to the 13th of August 2015, obtained from the Komakuk Beach weather station (WMO ID: 71046) and the currents of the mid water column (2.59m to 9.59m above the seafloor), obtained using in-situ ADCP measurements from the 28th of July at 0:00 the 13th of August at 15:00. The ADCP was located at 69.558393 °N 138.914445 °W. The data points are symbolized using the symbols in the legend in the upper right corner. No fetch is defined as directional fetch below 3 km, short fetch as between 3 and 15km and long fetch everything above 15km.

The Figure 5-38 show the correlation of lower column current speed and wind speed sorted by the fetch categories. The R^2 value for the lower column speed and wind speed at large fetch conditions is 0.00 with a sample size of 37. The R^2 value for the lower column speed and wind speed at small fetch conditions is 0.01 with a sample size of 34. The R^2 value for the lower column speed and wind speed at no fetch conditions is 0.05 at 49 occurrences.

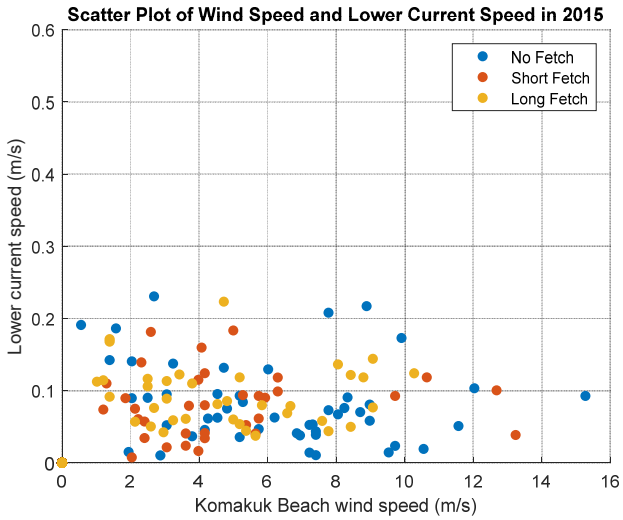

Figure 5-38: Scatter plot of wind speed in meter per second in the 2015 measurement period from the 28th of July 2015 to the 13th of August 2015, obtained from the Komakuk Beach weather station (WMO ID: 71046) and the currents of the lower water column (1.59m to 2.59m above the seafloor),

obtained using in-situ ADCP measurements from the 28th of July at 0:00 the 13th of August at 15:00. The ADCP was located at 69.558393°N 138.914445°W. The data points are symbolized using the symbols in the legend in the upper right corner. No fetch is defined as directional fetch below 3 km, short fetch as between 3 and 15km and long fetch everything above 15km.

5.3.2 Modelled Waves and Current Speed

The wave heights, in 2015 obtained from the Alaska 4m grid of the NOAA WaveWatch III® productional hindcast for the grid point at 69.533°N and 138.867°W, are linked with the current speed of the three different parts of the water column. The first plot, Figure 5-39, shows the correlation of wave height and current speed for the upper water column. The R^2 value for this data is 0.12 for the 103 data points.

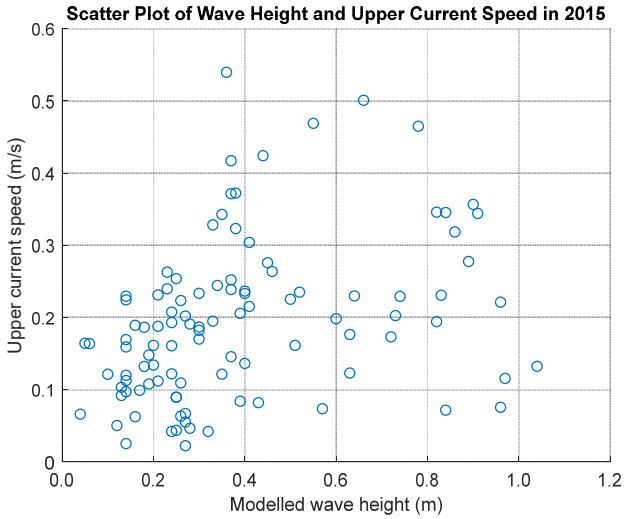

Figure 5-39: Scatter plot of NOAA WAVEWATCH III® modelled wave height in meter at 69.533°N and 138.867°W and the currents of the upper water column (9.59m to 10.59m above the seafloor), obtained using in-situ ADCP measurements. Data period is from the 31st of July 2015 18:00 to the 13th of August 2015 12:00. The ADCP was located at 69.558393 °N 138.914445 °W.

The second plot, Figure 5-40 shows the correlation of wave height and current speed for the mid water column. The R^2 value for this data is 0.02 for the 103 data points. The third plot, Figure 5-41 shows the correlation of wave height and current speed for the lower water column. The R^2 value for this data is 0.00 for the 103 data points. The R^2 values are very low for wave height and current speed of all column. This indicates that no direct linear correlation between the parameter exists, for the data presented here.

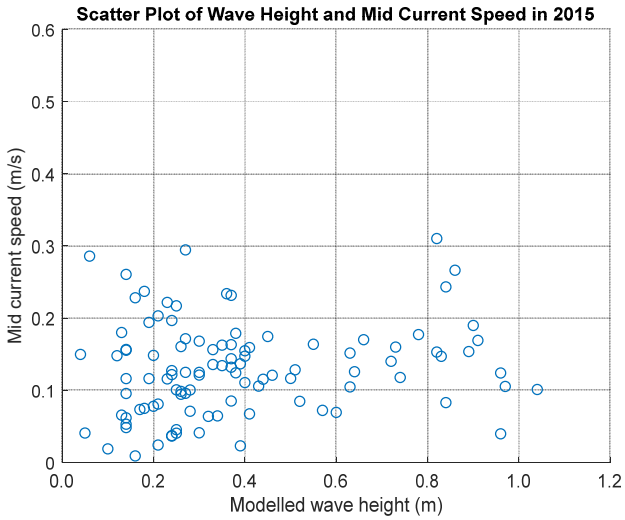

.Figure 5-40: Scatter plot of NOAA WAVEWATCH III® modelled wave height in meter at 69.533°N and 138.867°W and the currents of the mid water column (2.59m to 9.59m above the seafloor), obtained using in-situ ADCP measurements. Data period is from the 31st of July 2015 18:00 to the 13th of August 2015 12:00. The ADCP was located at 69.558393°N 138.914445°W.

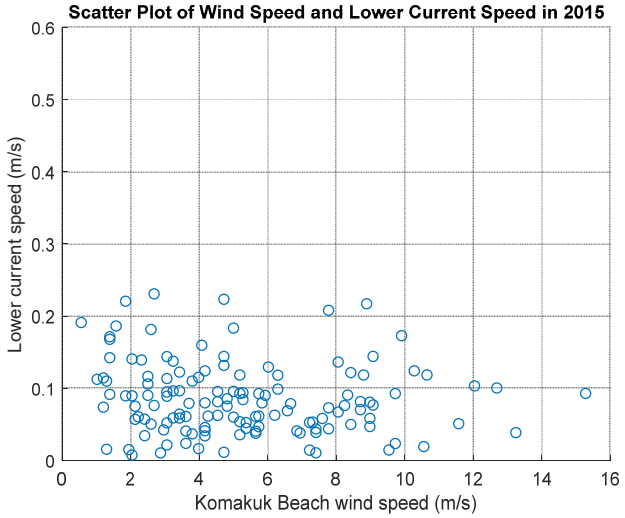

Figure 5-41: Scatter plot of NOAA WAVEWATCH III® modelled wave height in meter at 69.533 N and 138.867 W and the currents of the lower water column (1.59m to 2.59m above the seafloor), obtained using in-situ ADCP measurements. Data period is from the 31st of July 2015 18:00 to the 13th of August 2015 12:00. The ADCP was located at 69.558393 °N 138.914445 °W.

5.4 Statistical Relationship – Study Location B – 2018

In this chapter the linkage for the environmental forcing parameter and the current speed in the three parts of the water column for the mooring in 2018 at study site B is investigated. In Figure 5-42 the environmental forcing parameter and the current speeds are shown.

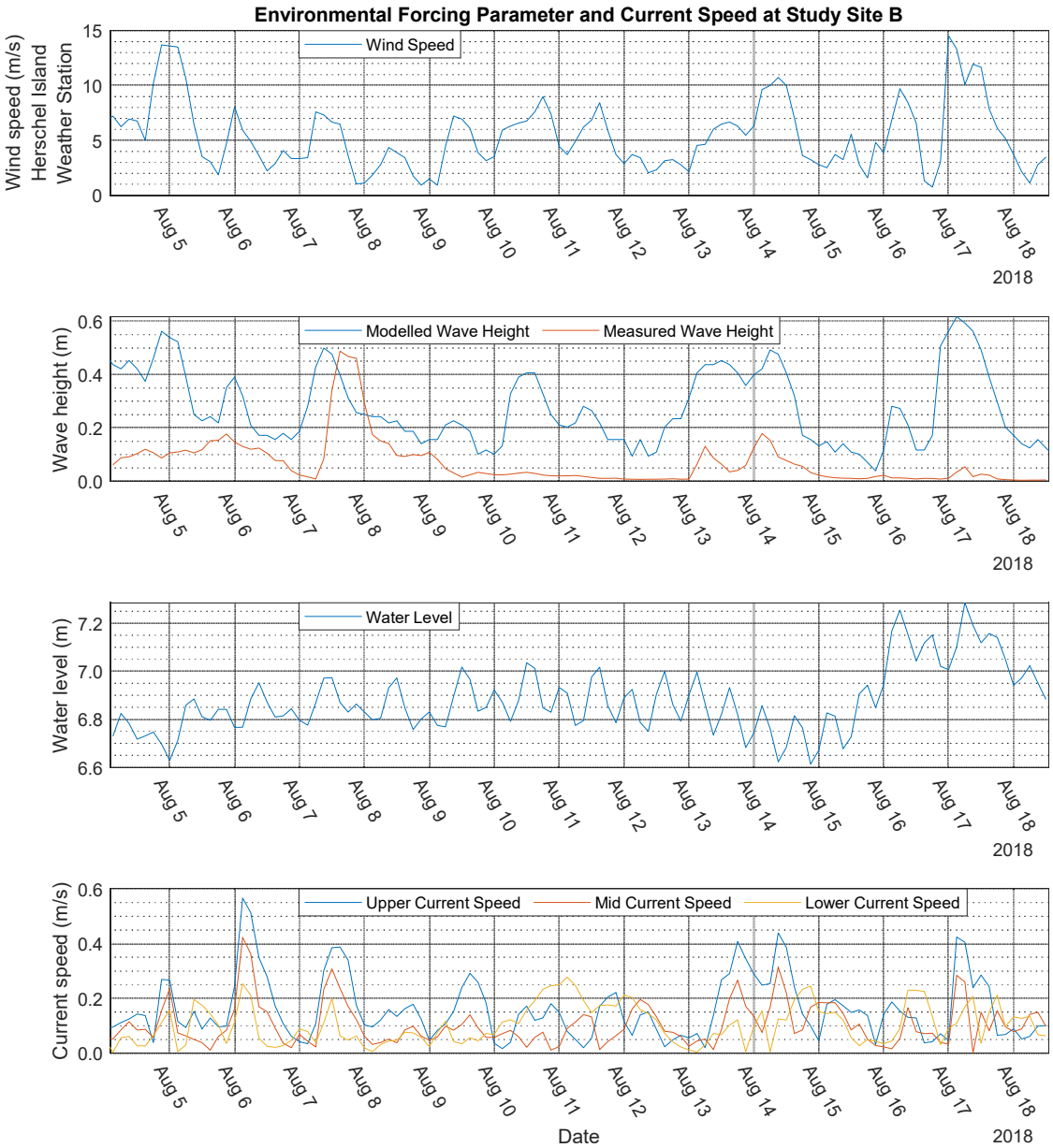

Figure 5-42: First plot shows the wind speed in the 2018 measurement period, obtained from the Herschel Island weather station (WMO ID: 71501). The second plot shows the wave height in meter of the NOAA WAVEWATCH III® modelled wave height at 69.4666°N and 139.0001°W in blue and the measured nondirectional wave height measurement obtained with a RBRsolo³ D |wave16 sensor, that was located at 69.465833°N 139.030555°W. The third plot shows the water depth at the sensor location measured with the RBRsolo³ D |wave16 sensor in meter. The fourth plot shows current speed of the upper water column, 4.59m to 5.59m above the seafloor, in blue, the current speed of the mid water column, 2.59m to 4.59m above the seafloor, in red and the lower water column from 1.59m to 2.59m above the seafloor in yellow in meter per second. The RDI Workhorse Sentinel 600 kHz ADCP was located at 69.465833°N 139.030555°W. The collective measurement period spans from the 4th of August 2018 3:00 to the 18th of August 2018 12:00.

5.4.1 Wind Speed and Current Speed

The wind speed of the Herschel Island weather station is combined with the adjacent measured current speed, in the upper, middle and lower column. The scatter plots serve as reflection of the potential correlation of the parameter. The correlation of wind speed and upper column current speed can be found in Figure 5-43. The R^2 value for this is 0.14 for the 117 data points.

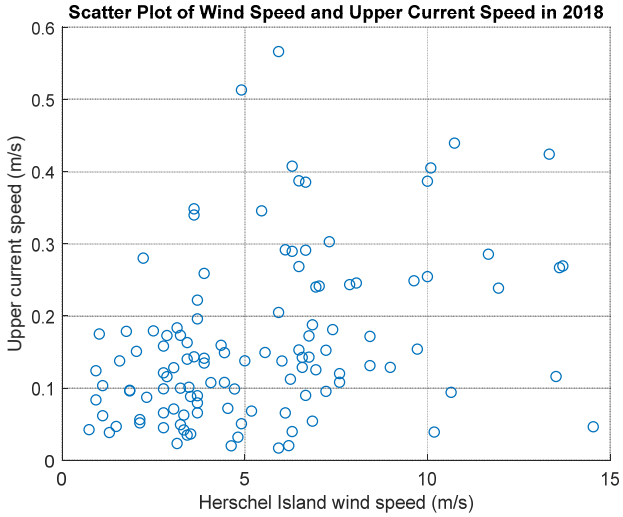

Figure 5-43: Scatter plot of wind speed in (m/s) in the 2018 measurement period from the 4th of August 2018 3:00 to the 18th of August 2018 12:00., obtained from the Herschel Island weather station (WMO ID: 71501) and the upper column current speed (4.59m to 5.59m above the seafloor), obtained using ADCP measurements in same period.

The correlation of wind speed and mid column current speed can be found in Figure 5-44. The R^2 value for this is 0.04 for the 117 data points.

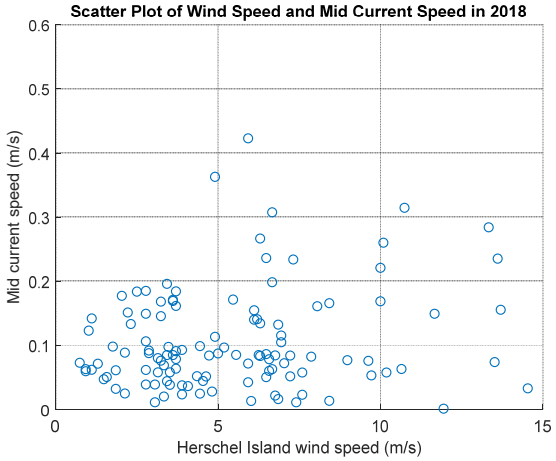

Figure 5-44 Scatter plot of wind speed in (m/s) in the 2018 measurement period from the 4th of August 2018 3:00 to the 18th of August 2018 12:00., obtained from the Herschel Island weather station (WMO ID: 71501) and the mid column current speed (2.59m to 4.59m above the seafloor), obtained using ADCP measurements in same period.

The correlation of wind speed and lower column current speed can be found in Figure 5-45. The R^2 value for this is 0.01 for the 117 data points.

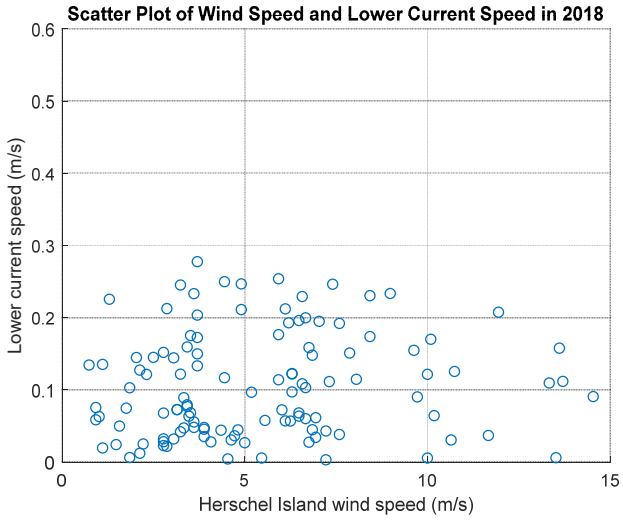

Figure 5-45: Scatter plot of wind speed in (m/s) in the 2018 measurement period from the 4th of August 2018 3:00 to the 18th of August 2018 12:00., obtained from the Herschel Island weather station (WMO ID: 71501) and the lower column current speed (1.59m to 2.59m above the seafloor), obtained using ADCP measurements of the same period.

The correlations of wind speed and current speed didn't show a linear correlation throughout the water column, indicated by the very low values of the coefficients of determination. To overcome potential of different wind directions having a varying influence on the current speed, another investigation is done, using wind directions to separate the data. In Figure 5-46 the wind speed and current speed for the upper water column is displayed, while the wind is categorized in eight directions. The directions are north from 337.5 to 22.5 degree, northeast from 22.5 degree to 67.5 degree, east from 67.5 degree to 112.5 degree, southeast from 112.5 degree to 157.5 degree, south from 157.5 degree to 202.5 degree, southwest from 202.5 degree to 247.5 degree, west from 247.5 degree to 292.5 degree and northwest from 292.5 degree to 337.5 degree.

The R^2 is calculated for categories, where more than ten data points were available to overcome potential statistical problems of low samples sizes. For the wind speed and the upper water column current speed the R^2 value is 0.135 for all 117 samples. The R^2 value for wind coming from southeast is 0.07 with 14 samples, 0.06 for south wind at 23 occurrences, 0.13 for the 47 southwest wind occurrences and 0.02 for west winds that occurred 25 times in the mooring period. North, northeast, east and northwest directions occurred too little, to consider.

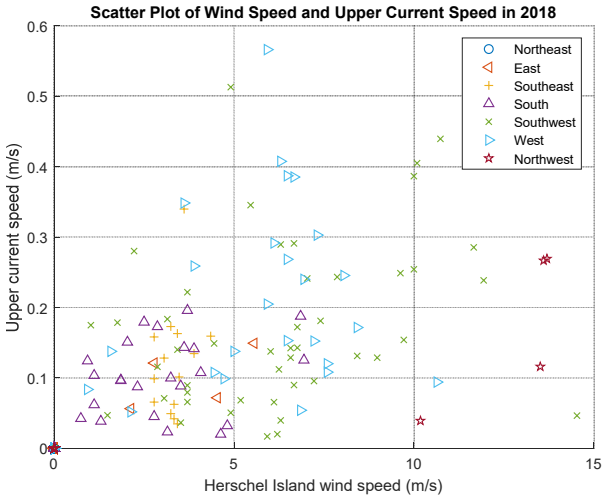

Figure 5-46: Scatter plot of wind speed in m/s in the 2018 measurement period from he 4th of August 2018 3:00 to the 18th of August 2018 12:00, obtained from the Herschel Island weather station (WMO ID: 71501) and currents of the upper water column (4.59m to 5.59m above the seafloor), obtained using in-situ ADCP measurements. The data points are symbolized using the symbols in the legend in the upper right corner. The wind direction is divided into eight categories, note that north winds were absent in this time period.

In Figure 5-47, the correlation of wind speed and mid column current speed is displayed, using wind directions as categories as mentioned above. The overall correlation value is 0.39 for the 117 samples. The R^2 is calculated for categories, where more than ten data points were available to overcome potential statistical problems of low samples sizes. The R^2 value for wind coming from southeast is 0.04 with 14 samples, 0.04 for south wind at 23 occurrences, 0.03 for southwest wind at 47 occurrences and 0.00 for west winds that occurred 25 times in the mooring period. North, northeast, east and northwest directions occurred too little, to consider.

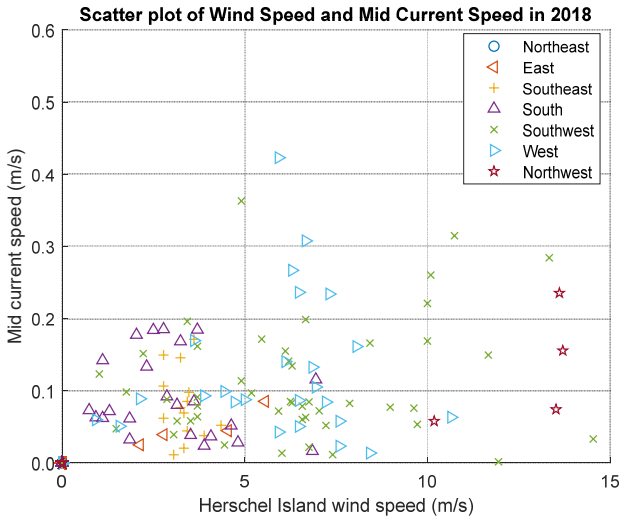

Figure 5-47: Scatter plot of wind speed in m/s in the 2018 measurement period from he 4th of August 2018 3:00 to the 18th of August 2018 12:00, obtained from the Herschel Island weather station (WMO ID: 71501) and currents of the mid water column (2.59m to 4.59m above the

seafloor), obtained using in-situ ADCP measurements. The data points are symbolized using the symbols in the legend in the upper right corner. The wind direction is divided into eight categories, note that north winds were absent in this time period.

In Figure 5-48, the correlation of wind speed and lower column current speed is displayed, using wind directions as categories as mentioned above. The overall correlation value is 0.01 for the 117 samples. The R^2 is calculated for categories, where more than ten data points were available to overcome potential statistical problems of low samples sizes. The R^2 value for wind coming from southeast is 0.01 with 14 samples, 0.05 for south wind at 23 occurrences, 0.00 for southwest wind at 47 occurrences and 0.02 for west winds that occurred 25 times in the mooring period. North, northeast, east and northwest directions occurred too little, to consider.

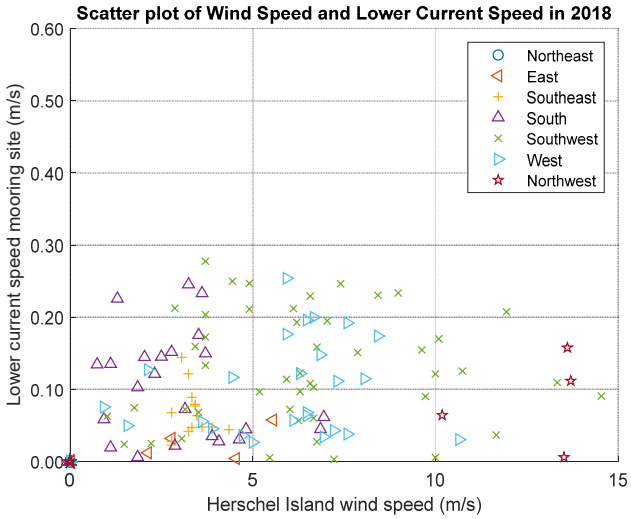

Figure 5-48: Scatter plot of wind speed in m/s in the 2018 measurement period from he 4th of August 2018 3:00 to the 18th of August 2018 12:00, obtained from the Herschel Island weather station (WMO ID: 71501) and currents of the lower water column (1.59m to 2.59m above the seafloor), obtained using in-situ ADCP measurements. The data points are symbolized using the symbols in the legend in the upper right corner. The wind direction is divided into eight categories, note that north winds were absent in this time period.

The wind speed and the current speed of the three water columns showed no linear correlation at the study site B in 2018 in terms of specific wind directions. To overcome the potential effect, that the categorical wind directions may not necessarily reflect the wind directions that have a large potential fetch, and so have more potential to generate large wave and current action, a new sorting is done. To do so the data is divided into upper, mid and lower column current speed and the wind speed into no fetch, small fetch and large fetch.

For this the average fetch for the different directions is used, that are calculated and used in chapter 5.2.2. The long fetch direction (more than 15 km potential directional fetch) is

here defined as wind directions, where directional fetch directions wind coming from directions between 40 degree and 140 degree clockwise. The small fetch direction (between three and 15 kilometre) is between 140 degree and 170 degree and between 310 degree and 40 degree clockwise. The no fetch direction, where the potential directional fetch is below three kilometre) is between 170 degree and 310 degree clockwise.

In Figure 5-49, the correlation of upper column current speed and wind speed is shown, the data points are categorized using the fetch conditions just explained. The correlation for the large fetch is 0.10 at a sample size of eleven, small fetch of 0.02 at sample size of 14 and for no fetch conditions that occurred 92 times the R^2 value is 0.11.

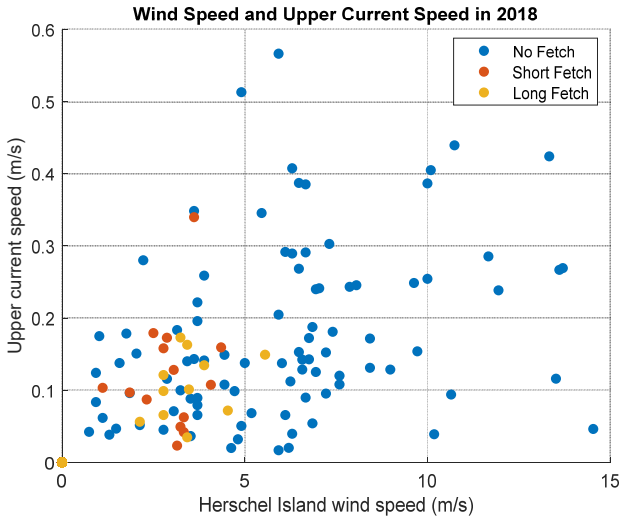

Figure 5-49: Scatter plot of wind speed in (m/s) in the 2018 measurement period from the 4th of August 2018 3:00 to the 18th of August 2018 12:00., obtained from the Herschel Island weather station (WMO ID: 71501) and the upper column current speed (4.59m to 5.59m above the seafloor), obtained using ADCP measurements of the same period. The data points are symbolized using the symbols in the legend in the upper right corner. No fetch is defined as directional fetch below 3 km, short fetch as between 3 and 15km and long fetch everything above 15km.

In Figure 5-50 the correlation of mid column current speed and wind speed is shown, the data points are categorized using the same conditions as before. The correlation for the large fetch is 0.00 with eleven data points, for the small fetch R^2 is 0.03 at 14 points and for no fetch conditions its 0.02 at a sample size of 92.

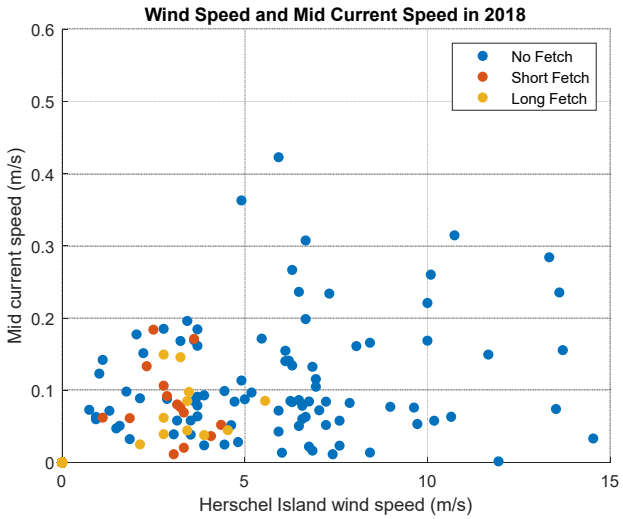

Figure 5-50: Scatter plot of wind speed in (m/s) in the 2018 measurement period from the 4th of August 2018 3:00 to the 18th of August 2018 12:00., obtained from the Herschel Island weather station (WMO ID: 71501) and the mid column current speed (2.59m to 4.59m above the seafloor), obtained using ADCP measurements of the same period. The data points are symbolized using the symbols in the legend in the upper right corner. No fetch is defined as directional fetch below 3 km, short fetch as between 3 and 15km and long fetch everything above 15km.

In Figure 5-51 the correlation of lower column current speed and wind speed is shown, the data points are categorized using the same conditions as before. The correlation for the large fetch is 0.00 with eleven data points, for the small fetch R^2 is 0.04 at 14 points and for no fetch conditions its 0.00 at a sample size of 92.

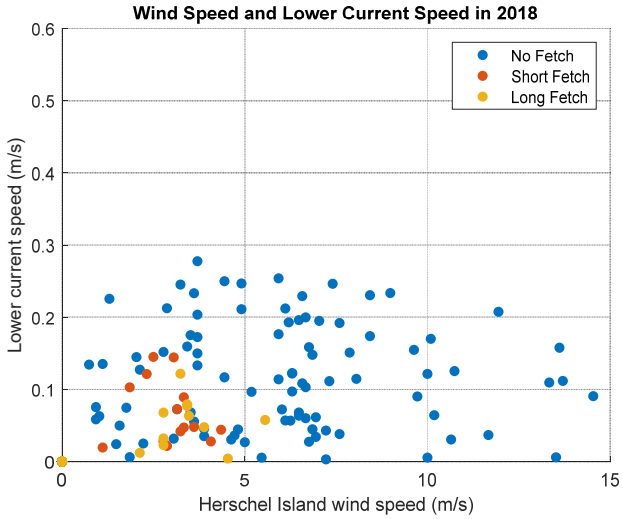

Figure 5-51: Scatter plot of wind speed in (m/s) in the 2018 measurement period from the 4th of August 2018 3:00 to the 18th of August 2018 12:00., obtained from the Herschel Island weather station (WMO ID: 71501) and the lower column current speed (1.59m to 2.59m above the seafloor), obtained using ADCP measurements of the same period. The data points are symbolized using the symbols in the legend in the upper right corner. No fetch is defined as directional fetch below 3 km, short fetch as between 3 and 15km and long fetch everything above 15km.

5.4.2 Modelled Waves and Current Speed

As no correlation was found between wind speed and current speed in general and under direction and fetch sorting, the next environmental forcing parameter is checked for potential correlation. For comparison reasons, the modelled wave heights is used here as well as the in-situ measured wave heights. The plot for linkage of upper current speed and modelled wave height can be found in Figure 5-52. The R^2 value is 0.00 for the 116 data points.

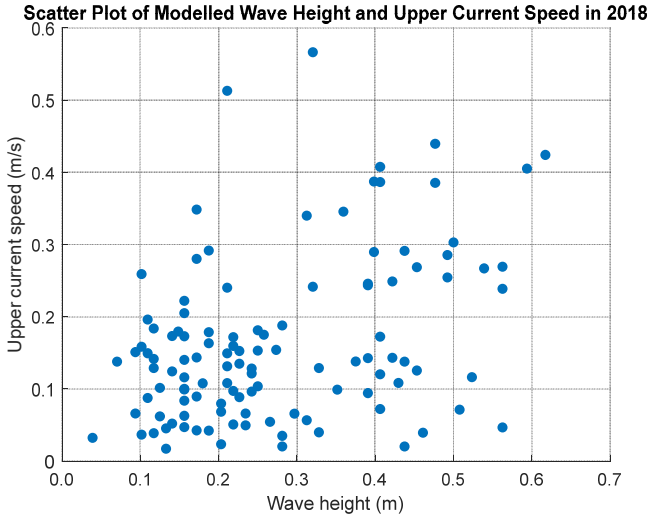

Figure 5-52: Scatter plot of NOAA WAVEWATCH III® modelled wave height in meter at 69.533°N and 138.867°W and the currents of the upper water column (4.59m to 5.59m above the seafloor), obtained using in-situ ADCP measurements. Data period is period from the 4th of August 2018 3:00 to the 18th of August 2018 12:00. The ADCP was located at 69.46583°N 139.030555°W.

In Figure 5-53 the linkage of modelled wave heights and current speed of the mid water column is displayed. The coefficient of determination is 0.01.

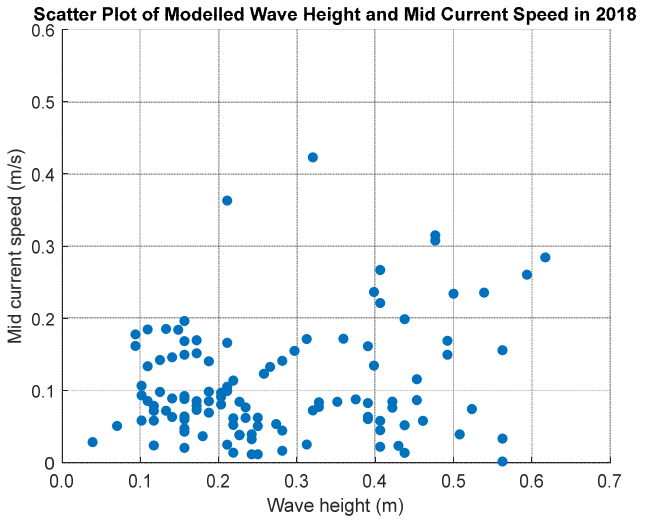

Figure 5-53: Scatter plot of NOAA WAVEWATCH III® modelled wave height in meter at 69.533°N and 138.867°W and the currents of the mid water column (2.59m to 4.59m above the seafloor),

obtained using in-situ ADCP measurements. Data period is period from the 4th of August 2018 3:00 to the 18th of August 2018 12:00. The ADCP was located at 69.46583°N 139.030555°W.

In Figure 5-54 the linkage of modelled wave heights and current speed of the lower water column is displayed. The coefficient of determination is 0.04.

The very low R^2 values indicate, that no linear correlation between the modelled wave heights and the current speed throughout the water column exists.

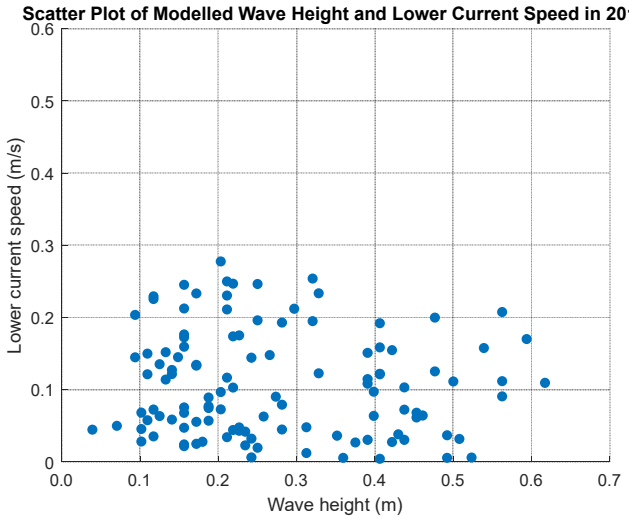

Figure 5-54: Scatter plot of NOAA WAVEWATCH III® modelled wave height in meter at 69.533°N and 138.867°W and the currents of the lower water column (1.59m to 2.59m above the seafloor), obtained using in-situ ADCP measurements. Data period is period from the 4th of August 2018 3:00 to the 18th of August 2018 12:00. The ADCP was located at 69.46583°N 139.030555°W.

5.4.3 Measured Waves and Current Speed

The linkage of measured wave heights and currents is done the same way as the modelled wave heights and currents were linked, using scatter plots to visualise and coefficient of determination to statistically control the correlation. In Figure 5-55 the correlation of measured wave heights in 2018 and the upper current speed is displayed, the R^2 value is 0.11.

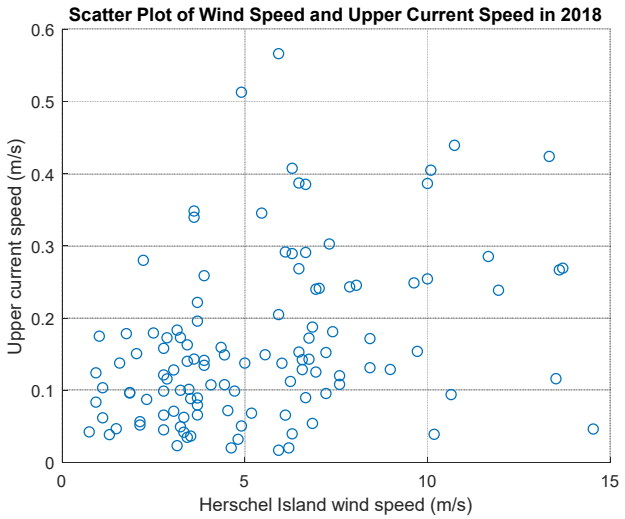

Figure 5-55: Scatter plot of in-situ measured wave heights in m at 69.46583°N 139.03055°W and the currents of the upper water column (4.59m to 5.59m above the seafloor),
obtained using in-situ ADCP measurements. Data period is period from the 4th of August 2018 3:00 to the 18th of August 2018 12:00. The ADCP was located at 69.46583°N 139.030555°W.

In Figure 5-56 the correlation of measured wave heights in 2018 and the mid current speed is displayed, the R^2 value is 0.05.

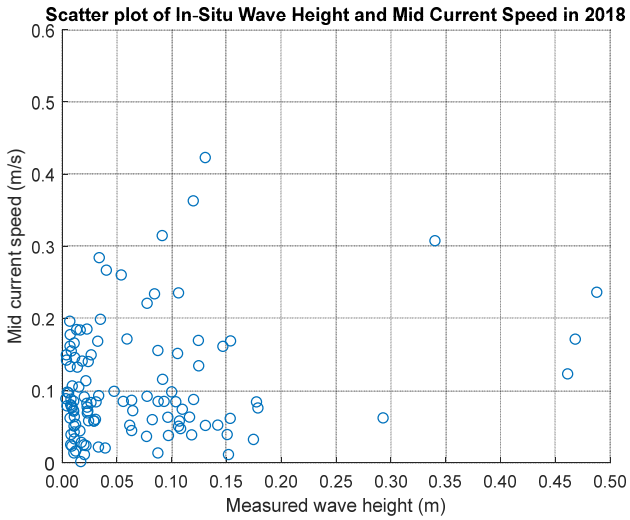

Figure 5-56: Scatter plot of in-situ measured wave heights in m at 69.46583°N 139.03055°W and the currents of the mid water column (2.59m to 4.59m above the seafloor),
obtained using in-situ ADCP measurements. Data period is period from the 4th of August 2018 3:00 to the 18th of August 2018 12:00. The ADCP was located at 69.46583°N 139.030555°W.

In Figure 5-57 the correlation of measured wave heights in 2018 and the lower current speed is displayed, the R^2 value is 0.02.

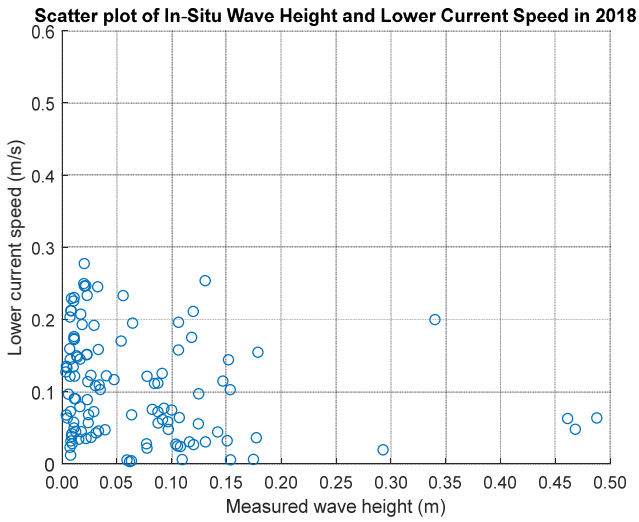

Figure 5-57: Scatter plot of in-situ measured wave heights in m at 69.46583°N 139.03055°W and the currents of the lower water column (1.59m to 2.59m above the seafloor), obtained using in-situ ADCP measurements. Data period is period from the 4th of August 2018 3:00 to the 18th of August 2018 12:00. The ADCP was located at 69.46583°N 139.030555°W.

Like in Chapter 5.4.2, no linear correlation between the measured wave height and the current speed exist.

5.4.4 Water Level and Current Speed

In 2018 at study site B additional to wave heights, the sensor measured the water level as changes in water level can potentially create movement of water masses. In the following, the water level is linked with current speed within the three columns. In Figure 5-58 the upper column current and water level is plotted. The R^2 value is 0.00. In Figure 5-59 the scatter of mid water current speed and the water level is shown. The R^2 value for the mid

column 0.01. The correlation of lower water column currents and the water level is shown in Figure 5-60, the R^2 value for this is 0.02.

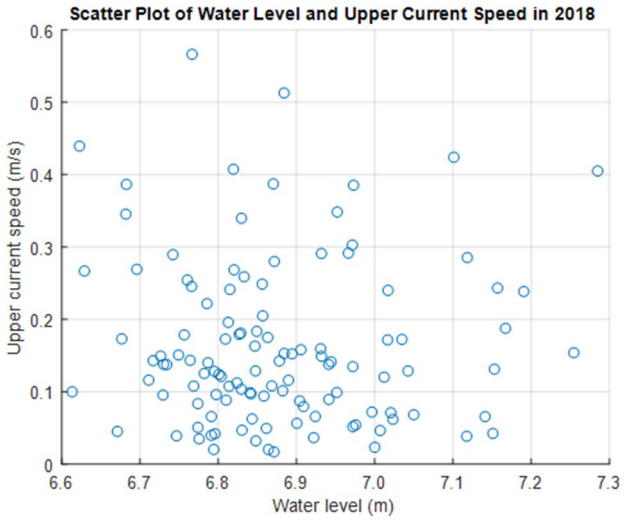

Figure 5-58: Scatter plot of water level in m at 69.46583°N 139.03055°W and the currents of the upper water column (4.59m to 5.59m above the seafloor), obtained using in-situ ADCP measurements. Data period is period from the 4th of August 2018 3:00 to the 18th of August 2018 12:00. The ADCP was located at 69.46583°N 139.030555°W.

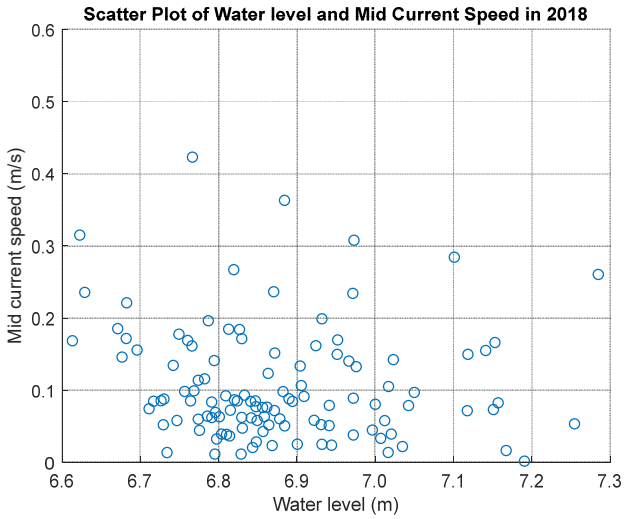

Figure 5-59: Scatter plot of water level in m at 69.46583°N 139.03055°W and the currents of the mid water column (2.59m to 4.59m above the seafloor), obtained using in-situ ADCP measurements. Data period is period from the 4th of August 2018 3:00 to the 18th of August 2018 12:00. The ADCP was located at 69.46583°N 139.030555°W.

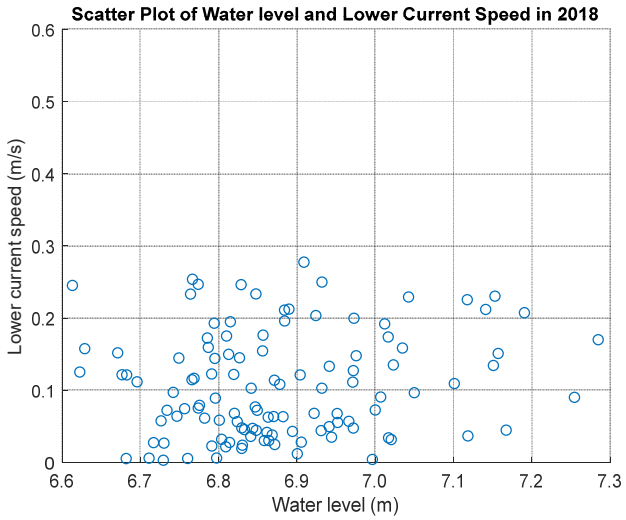

Figure 5-60: Scatter plot of water level in m at 69.46583°N 139.03055°W and the currents of the lower water column (1.59m to 2.59m above the seafloor), obtained using in-situ ADCP measurements. Data period is period from the 4th of August 2018 3:00 to the 18th of August 2018 12:00. The ADCP was located at 69.46583°N 139.030555°W.

6 Discussion

6.1 Environmental Forcing Conditions

6.1.1 Wind

The wind speed conditions in the 2015 and 2018 study periods, that are both mainly in the first half of August, show typical conditions for the coast of the Southwestern Canadian Beaufort Sea. The wind speeds were very similar to findings of (Hill et al., 1991; Radosavljevic et al., 2016; Cunliffe et al., 2019). Both measurement periods have similar average wind speeds with 5.3 m/s in 2018 and 5.4 m/s in 2015.

The prevailing wind directions contrast between 2015 and 2018. In 2015, a bimodal pattern of wind directions is recorded. Wind direction of moderate to high winds are group at W to W-NW and E, this fits into previous wind direction distributions for Herschel Island by Radosavljevic et al. (2016). In 2018, the prevailing wind direction is south to west, for winds of moderate to high speed, likely resulting from baroclinic influence (Chapter 3.1), except for a W-NW storm event.

Arctic storm events according to the definition of Atkinson (2005), occurred in both measurement periods. In the first study period, one storm event, with W-NW winds of 21 hours duration with peak wind speeds of 15.3 m/s was recorded. In the second study period, three storm events occurred, one SW, one S-SW and one W-NW with durations from 9 to 15 hours and wind speeds from 10 to 15 m/s.

6.1.2 Fetch and Waves

In both time series of the directional fetch (Figure 5-3 and Figure 5-18), large fluctuations are visible. In 2015, the main reason for this are shifts in wind direction, as the sea ice field was relatively constant in the measurement period and the average directional fetch is nearly identical to the maximum directional fetch. In 2018, the spiking resulted from a combination of sea ice variability and changes in wind direction. Due to the orientation of the shoreline of the study sites A and B, that is partly sheltered by Herschel Island, large difference between winds from the coast and winds from offshore direction exist. Uncertainties in fetch conditions arise with the assumption that the wind field is constant over the distance towards the coast or sea ice edge, yet previous studies applied the same method and found this assumption to be reasonable (Barnhart et al., 2014a; Overeem et al., 2011). Additionally, the usage of Komakuk Beach weather station in 2015, in compensation to the failure of the Herschel Island distorted the calculation of the actual fetch conditions.

Despite large differences in directional fetch conditions (Figure 5-4 and Figure 5-17), wave conditions, as reflected in average significant wave heights are nearly identical under comparable wind speed conditions, see the time series and wave data description in Chapter 5.1.3 and 5.2.3. The reason for this could be rapid changes from long to short fetch conditions, that is evident in both measurement periods. Another difficulty are differences in site specific properties, that could be due to nearby bathymetry and its influence of wave heights, or uncertainties within the modelled wave heights, even thought it is widely accepted and used in the scientific community (Chawla et al., 2012; Singhal et al., 2013; Hiles et al., 2014).

The modelled wave heights compared with the in-situ measured wave heights show clear discrepancies, even though the magnitude agrees and a. The reason for these differences, is most likely found in the large sea ice concentration in the measurement period, that locally damped the wave height more than the model calculated for the closest grid point.

The obtained wave heights in the study periods of 2015 and 2018 are fairly low, yet typical for the summer season of the Canadian Beaufort Sea. Hill et al. (1990), reported a similar wave height data set for the nearshore area of King Point (around 50 km in southwest direction), they also related the reduced wave heights to the dampening effect of nearby sea ice. Another similarity to results in here, are the quick rise in wave height in response to favorable conditions, visible in the in-situ measured waves in 2018. In the Western Canadian Beaufort Sea, Davidson et al. (1988) reported wave heights up to 2 m at a study site in the nearshore zone. They could link the generation of these waves, with favorable constant strong winds in combination with a large distance to the sea ice edge.

6.1.3 Stratification

The extent of the Mackenzie River plume in the Western Canadian Beaufort Sea in summer is mainly wind dependent (Hill et al., 1990; Ehn et al., 2019), with an extension under east winds and a retreat under west winds. In 2015, a strong separation of the water column at the study area is visible, while in 2018 the water column is relatively uniform.

In 2015, between the 28th of July and the 30th of July, the plume layer thinned, and the water column became more separated, most likely due to stable east winds in this period. Varying wind conditions with a tendency to west winds, between the 30th of July and the 5th of August, probably caused mixing a less stratified water column and mixing. From the 5th of August to the 9th of August stable and strong east winds led to a rise of cold water in the lower part of the column and led to a strong stratification, with a dense thin plume layer, resulting in a two layered water column, see Figure 5-7.

In 2018, the stratification of the water column differed significantly from 2015. The influence of Mackenzie plume was very limited, as can be seen in uniformity of the temperature profile, while the salinity is increasing with depth, one consideration could be a cooled temperature due to the presence of sea ice and overall cold temperatures within the measurement period.

The influence of sediment and water provided from the Mackenzie river is a major reason for the uniqueness of the coastal zone of the western Canadian Beaufort Sea. It therefore differs from other arctic coasts, like the Alaskan Beaufort Sea (Weingartner et al., 2009; 2017). While the plume extension is remarkable depending on wind conditions and season, it is less present than in the eastern Canadian Beaufort Sea (Dunton et al., 2006; Davidson et al.,1988).

6.2 Formation of Currents

Within the measurement presented here, currents are usually faster the higher in the water column. This agrees with measurements of Davidson et al. (1988) in the eastern Canadian Beaufort Sea. This can be expected for wave generated currents as well as for direct wind forcing (Davidson et al., 1988). Davidson et al. (1988) highlights the possibility to reveal forcing processes by their acting frequency and find that wind changes are largely agreeing with changes in currents in their measurements.

A similarity between the shifts in wind and a response in currents is visible in this data, see Figure 5-29 and Figure 5-42. However, the current response doesn't occur instantaneously and most likely has a complex dependence on direction, which is probably the reason for poor correlation values in Chapter 5.3 and 5.4. The fact that currents are wind driven is also supported by similar studies like Harper et al. (1990), Hill et al. (1991), Mulligan et al. (2019) for the coastal region of the eastern Canadian Beaufort Sea as well as studies in the coastal zone of the Alaskan Beaufort Sea (Dunton et al., 2006; Weingartner et al., 2009, 2017).

The currents showed not necessarily uniformity at different water level, yet events occurring were swift upper column currents influence lower ones. Hill et al. (1991) found that the response factor of bottom current speed to wind forcing for the inner shelf is 1.0 to 2.5%. For the 2015 period, the response is factor is at 1.7% for mean wind speed to mean lower current speed, and 1.5% when comparing the maximum values. In 2018, the scaling factor is slightly higher with 2.0% for mean and 1.9% for maximum values, but still in the range, probably due to a shallower site, that tend towards more water speed in general (Davidson et al., 1988). This finding is not supported by this study, where current speeds are very

similar between the study site A in 12 m water depth and study site B in 7 m water depth, yet the location and the conditions within the study period differed. However, Forest et al. (2016) found bottom current speeds of 0.4 to 0.5 m/s at the Beaufort Sea shelf break margin, which they could link to wind forced.

Local conditions most likely play a major role in the interplay of environmental forcing parameter and the currents in this study area. The mooring periods are too limited to give insights in the entirety of this complex interaction, but if we assume that the magnitude of currents in our study area is very limited in the landfast ice season (October to June), as in the Western Beaufort Sea (Dunton et al. 2006; Weingartner et al., 2017) and less coastal erosion occurs in fall as water temperatures are lower (Barnhart et al., 2014b), it may be reasonable to consider the presented data as valuable for the understanding of coastal erosion forcing in the study area.

The direction of currents complex and the causes not revealed by this study. In 2015 at study site A, the current in the upper water column tend to flow offshore and the currents below mainly in the same direction with reduced speed (Figure 6-1).

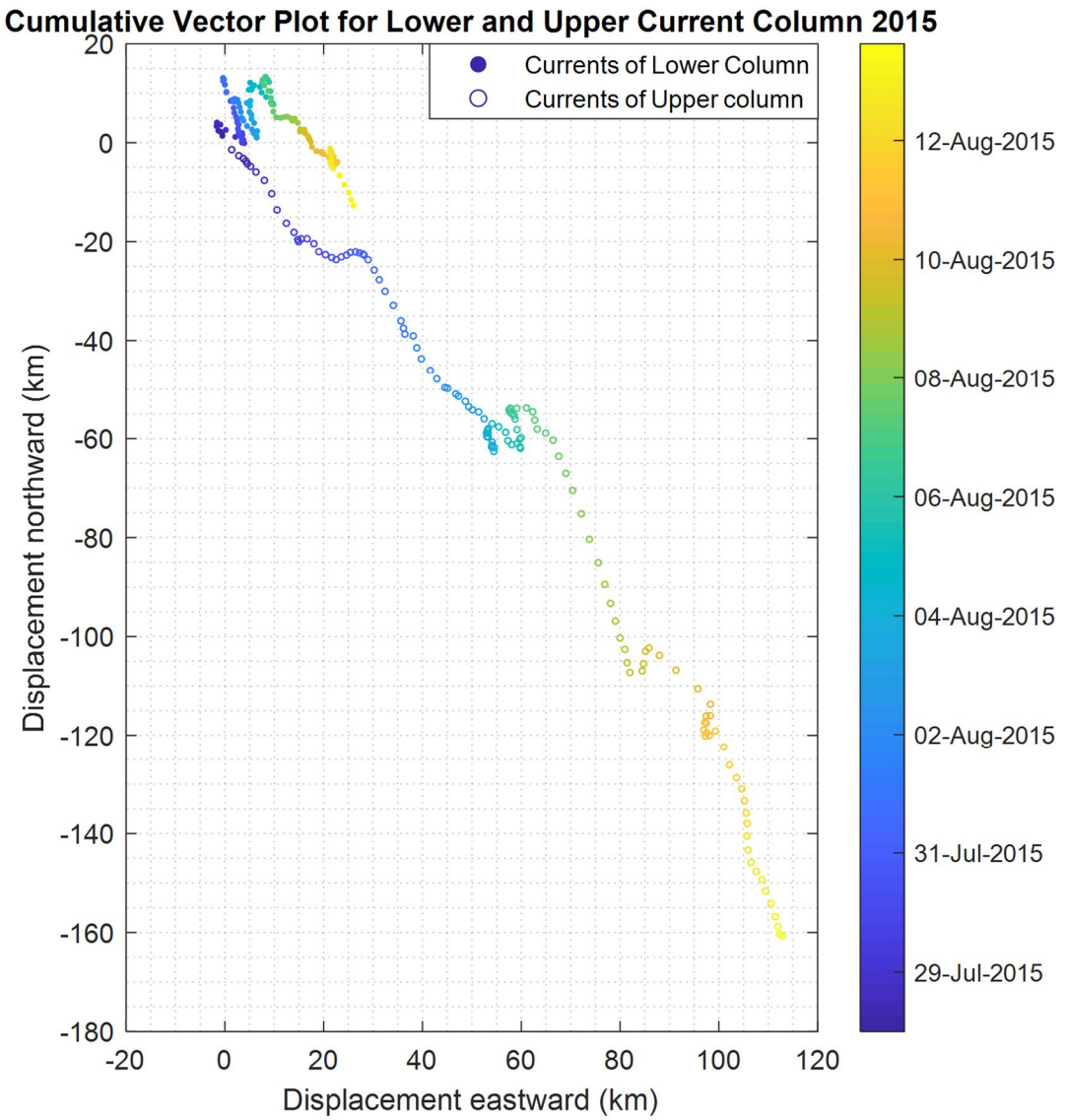

Figure 6-1: Cumulative vector plot for the current flow of the upper and lower water column in 2015. This graph serves to visualise the hypothetical movement of a particle, if it would move with the flow properties on the ADCP measurement site. The upper water column (circle) is defined as 9.59m to 10.59m above the seafloor, the lower water column (filled circle) from 1.59m to 2.59m above the seafloor. The measurement period spans from the 28th of July at 0:00 the 13th of August at 15:00. The sensor was located at 69.558393 °N 138.914445 °W. Data presentation was done in MATLAB with the use of the jLab MATLAB Toolbox (Lilly, 2019).

However, in 2018 at study site B the current of the upper water column was mainly direction onshore and the current in the lower water column was flowing mainly in the complete opposite direction (Figure 6-2).

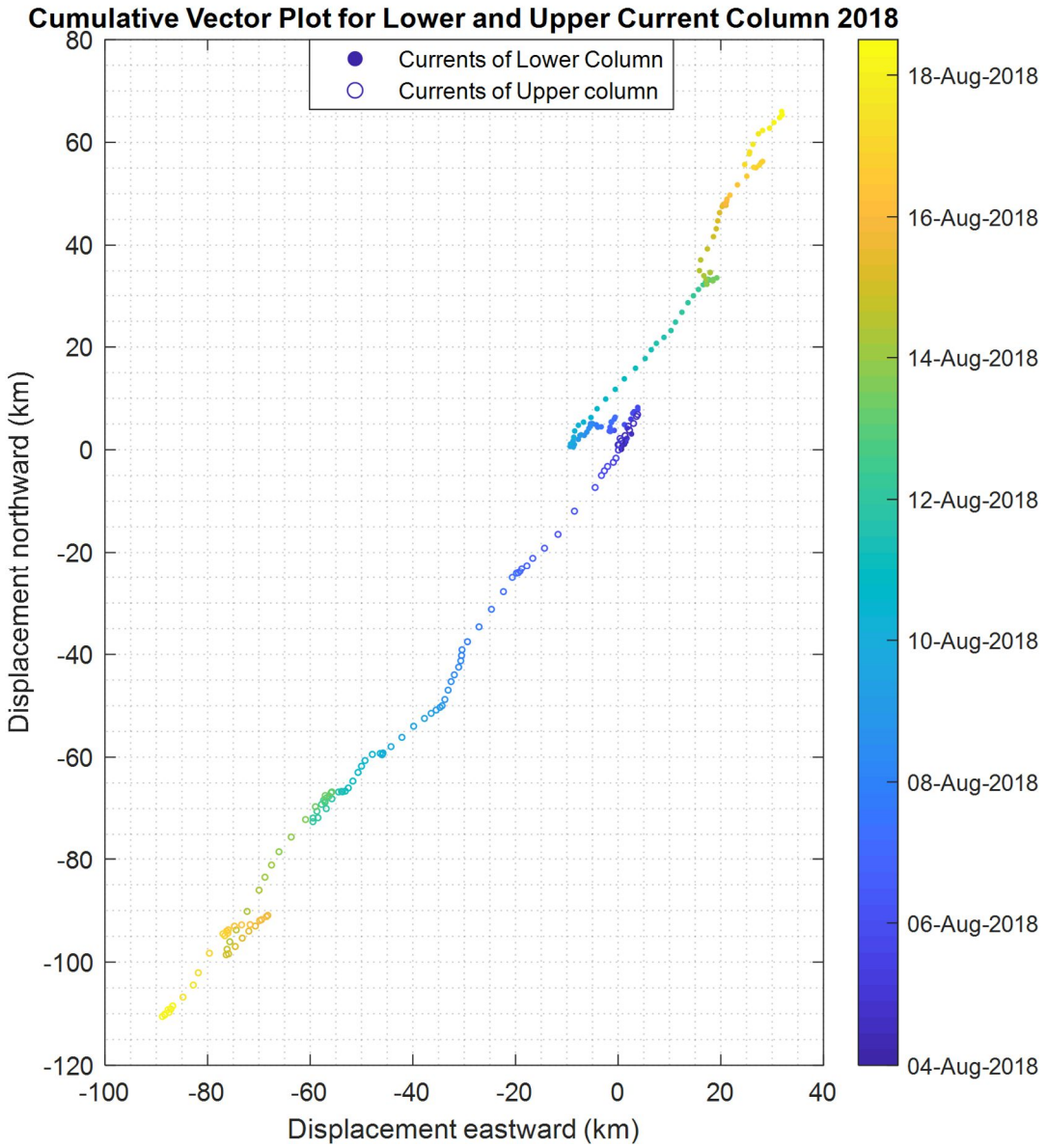

Figure 6-2: Cumulative vector plot for the current flow of the upper and lower water column in 2015. This graph serves to visualise the hypothetical movement of a particle, if it would move with the flow properties on the ADCP measurement site. The upper water column (circle) is defined as 4.59m to 5.59m above the seafloor, the lower water column (filled circle) from 1.59m to 2.59m above the seafloor. The measurement period spans from the 4th of August 2018 0:00 to the 18th of August 2018 12:00, spacing between dots is 3-hours. The sensor was located at 69.465833 °N 139.030555 °W. Data presentation was done in MATLAB with the use of the jLab MATLAB Toolbox (Lilly, 2019).

The observations of both study sites surprise to a degree, as the study sites are characterised by growing spits that are considered to get supplied by longshore drift sediment sources (Pelletier & Medioli, 2014; Radosavljevic et al., 2016; Irrgang et al., 2019).

A potential reason for the twofold pattern in current directions in 2018 could be a topographic effect, that led to a reflection of the upper flow at the shore (Davidson et al., 1988; Hequette et al., 2001). A possible explanation for the current direction in 2015 could be a larger scale effect were current turn around from the more open sited north site of Herschel Island and keep their flow direction from northwest, as Pelletier & Medioli (2014) highlight in the scheme for main current directions, see Figure 3-2.

Another reason for the missing longshore signal could be the fact, that the wave action was limited in both measurements. Longshore transport at coasts is generally associated with the energy of breaking waves, however the missing of wave breaking might explain the missing longshore signal (Davidson-Arnott, 2009).

6.3 Implications for Sediment Transport

Hill et al. (1991) and Davidson et al. (1988) classified the sediment transport in the nearshore zone of the Canadian Beaufort Sea as storm dominated. They highlight the importance of shear stress at the seafloor for the generation of turbulences that can mobilize sediments. Both studies show that this stress and resulting turbulences significantly increase with the presence of strong waves and are therefore the major component of the near bed current climate.

Due to the absence of larger wave events in the data here, most likely due to sea ice and fetch restrictions, in the mooring periods, the properties of the bottom current speed within the whole year are probably underestimated. Even though the current speed of the bottom column frequently topped 0.2 m/s, that falls into the lower range of mobilisation threshold of (0.18 – 0.36 m/s) for shelf sediments in the Canadian Beaufort Sea that Forest et al. (2016) calculated.

This might not be relevant for the longer term deposition of finer particles as they are mostly absent in this coastal zone, as described by O'Connor (1984) and Hill et al.(1991), who could not find deposition of plume sediments at the nearshore coast, besides Herschel Basin, but could be important for the residence time of suspended material that gets degraded after eroded from the coast (Vonk et al., 2014; Tanski et al., 2019). Jong et al. (2018) found an increased concentration of total organic carbon in water depths deeper than six meters, indicating that this zone could the start of a depositional environment of eroded organic material and highlight the importance for a potential erosion under enhanced water movement (see Chapter 6.4).

6.4 Potential Impacts of a Changing Arctic Ocean for the Study Sites

Recent climate studies note an ongoing change in the properties of environmental forcing parameter for the Canadian Beaufort Sea. Wood et al. (2013) highlight the change in wind direction towards more easterly winds, by a shift in large-scale pressure systems, since 2007. This is confirmed in the analysis of Wang et al. (2015), that investigated on long term climatic trends in the Beaufort Sea. Additionally, Frey et al. (2014) show a drastic weakening of sea ice persistence in the northern Canadian Beaufort Sea around Banks Island in recent years. Both changes, in wind direction and sea ice, could have major implications for the study area. The Figures 5-4 and 5-17 in this thesis show the potential directional fetch size and illustrate the limited fetch conditions, due to sheltering effect of Herschel Island, where large waves can only approach from the northeast. If the trend in wind direction shift continues and the relatively stable sea ice in front of Banks Island (Zhang et al., 2013; Moore et al., 2019) disappears, wave heights will likely increase at the study sites in respect to the newly developed favorable conditions for wave generation.

Solomon (2005) show a strong link between coastal erosion rates in the Canadian Beaufort Sea and the coastal orientation, towards wave approaching direction. The potential favorable conditions for waves in the future, increase the risk of a sudden increase in erosion rates for already threatened sites (Irrgang et al., 2019). Lantuit et al. (2012) found a link between wave action and the onset of erosion features like retrogressive thaw slumps, that can release vast amounts of organic-rich sediment into the nearshore zone (Tanski et al., 2017). Another possible implication for this potential enhanced wave action could be a remobilisation of organic-rich sediments buried in deeper parts of the coastal zone, due to an increase in bottom shear stress (Hill et al., 1991; Jong et al., 2018). However, for further insights into stress conditions at the bottom a more sophisticated analyse of orbital velocities and sediment properties is necessary (Hill et al., 1991).

7 Conclusion

The aim of this thesis was to analyse the currents in the nearshore zone of a region, that is threatened by coastal erosion. A second goal was to link environmental forcing parameter towards these currents and find a relationship between those. In a last step a connection to the sediment pathways was undertaken.

Measuring the currents in the nearshore zone of the Arctic Ocean is challenging, even though, in the two datasets presented here, first insights into the hydrodynamical conditions are gained. Further could the linkage with wind, wave and sea level data show, their potential for generating currents.

The study shows that currents are in general driven by the forcing of wind, even though a complex relationship of current and wind direction and a time-lag in the generation of currents complicate this linkage. In comparing the dataset of currents near Simpson Point and near Catton Point differences are visible in the direction and especially in the geometry throughout the water column. Since both measurements took place in different season, many different environmental parameters, like stratification, sea ice concentration and wind directions could be responsible for this deviation. Nevertheless, the currents of both sides agree in their magnitude of speed throughout the water column and in the trend the decreasing speed down the water column.

The fact that the presence of sea ice largely blocked the wave activity and movement of the upper water column might be important for the understanding of the future development of erosion rates at the study sites. As the analyse of directional fetch showed, differ the potential fetch lengths enormous depending on the direction of the wind. A shift in the prevailing wind direction, as shown by different authors could increase erosional force significant.

A surprising finding of this thesis is the decoupling of currents at the lower water column and wave activity at study site B and a generation of the highest flow speeds along the bottom water column within a period of no wave activity. This might be important in studying the sediment distribution in the breakup season, where the influence of waves is limited by the presence of sea ice. Yet, this data is only a snapshot of the seasonal cycle but might be used as guide for further studies. Especially a study during a strong wave event would benefit the understanding of bottom current generation.

As no previous data of nearshore currents in the Western Canadian Arctic exist, this thesis provides a first brought insight and gives a general idea about forcing mechanisms, speed and direction.

References

AMAP, (2019). AMAP Climate Change Update 2019: An Update to Key Findings of Snow, Water, Ice and Permafrost in the Arctic (SWIPA) 2017. Arctic Monitoring and Assessment Programme (AMAP), Oslo, Norway.

Atkinson, D. (2005). Observed storminess patterns and trends in the circum-Arctic coastal regime. Geo-Marine Letters, 25(2–3), 98–109. https://doi.org/10.1007/s00367-004-0191-0

Barnhart, K. R., Overeem, I., & Anderson, R. S. (2014a). The effect of changing sea ice on the physical vulnerability of Arctic coasts. The Cryosphere, 8(5), 1777–1799. https://doi.org/10.5194/tc-8-1777-2014

Barnhart, K. R., Anderson, R. S., Overeem, I., Wobus, C., Clow, G. D., & Urban, F. E. (2014b). Modeling erosion of ice-rich permafrost bluffs along the Alaskan Beaufort Sea coast. Journal of Geophysical Research: Earth Surface, 119, 1155–1179. https://doi.org/10.1002/2013JF002845

Berens, P. (2009). CircStat: A MATLAB Toolbox for Circular Statistics. Journal of Statistical Software, 31(10). https://doi.org/10.18637/jss.v031.i10

Burn, C. R. (2012). Herschel Island-Qikiqtaryuk: a natural and cultural history of Yukon's Arctic island. Alberta, University of Calgary Press.

Burn, C. R., & Zhang, Y. (2009). Permafrost and climate change at Herschel Island (Qikiqtaruq), Yukon Territory, Canada. Journal of Geophysical Research: Earth Surface, 114(2), 1–16. https://doi.org/10.1029/2008JF001087

Carrington, D. (2019). Global warming of oceans equivalent to an atomic bomb per second. The Guardian, London, January 7, 2019. Available at: https://www.theguardian.com/environment/2019/jan/07/global-warming-of-oceans-equivalent-to-an-atomic-bomb-per-second (Accessed: August 23, 2019)

Chawla, A., Spindler, D., & Tolman, H. (2012). 30 Year Wave Hindcasts using WAVEWATCH III® with CFSR winds Phase (p. 23). NOAA/NWS/NCEP/MMAB, Maryland USA.

Chawla A., Spindler D., & Tolman H. (2013). Validation of a thirty year wave hindcast using the climate forecast system reanalysis winds. Ocean Model. 70: 189–206. DOI: 10.1175/WAF-D-12-00007.1

CIS (Canadian Ice Service) (2005). MANICE: Manual of Standard Procedures for Observing and Reporting Ice Conditions. Ottawa: Environment Canada.

CIS (Canadian Ice Service) (2019). Archived Charts of the Canadian Ice Service. https://iceweb1.cis.ec.gc.ca/Archive/page1.xhtml?lang=en

Coch, C., Lamoureux, S. F., Knoblauch, C., Eischeid, I., Fritz, M., Obu, J., & Lantuit, H. (2018). Summer rainfall dissolved organic carbon, solute, and sediment fluxes in a small Arctic coastal catchment on Herschel Island (Yukon Territory, Canada). Arctic Science, 4(4), 750-780. https://doi.org/10.1139/as-2018-0010

Comiso, J. C. (2010). Polar Oceans From Space. Springer, New York.

Couture, N. J., Irrgang, A., Pollard, W., Lantuit, H., & Fritz, M. (2018). Coastal erosion of permafrost soils along the Yukon coastal plain and fluxes of organic carbon to the Canadian Beaufort Sea. Journal of Geophysical Research: Biogeosciences, 123(2), 406–422. https://doi.org/10.1002/2017JG004166

Dammann, D. O., Eriksson, L. E. B., Mahoney, A. R., Eicken, H., & Meyer, F. J. (2019). Mapping pan-Arctic landfast sea ice stability using Sentinel-1 interferometry. The Cryosphere, 13(2), 557–577. https://doi.org/10.5194/tc-13-557-2019

Davidson, S., De Margerie, S., & Lank, K. (1988). Sediment transport in the Mackenzie River plume. Geological Survey of Canada, Open File Report 2303.

Dunton, K. H., Weingartner, T., & Carmack, E. C. (2006). The nearshore western Beaufort Sea ecosystem: Circulation and importance of terrestrial carbon in arctic coastal food webs. Progress in Oceanography, 71(2–4), 362–378. https://doi.org/10.1016/j.pocean.2006.09.011

Edwards, T. (2019) Gwich'in partner with researcher to map important sites at risk in a shifting landscape, NNSL Media, Yellowknife, August 4, 2019. Available at: https://nnsl.com/nwtnewsnorth/gwichin-partner-with-researcher-to-map-important-sites-at-risk-in-a-shifting-landscape (Accessed: August 10, 2019).

Ehn, J. K., Reynolds, R. A., Stramski, D., Doxaran, D., Lansard, B., & Babin, M. (2019). Patterns of suspended particulate matter across the continental margin in the Canadian Beaufort Sea during summer. Biogeosciences, 16(7), 1583-1605. https://doi.org/10.5194/bg-16-1583-2019

EMC (2019). Wavewatch III® Production Hindcast, Multigrid: Feb 2005 to Mar 2019. Available at: https://polar.ncep.noaa.gov/waves/hindcasts/prod-multi_1.php (Accessed: November 13, 2019).

Environment Canada (2019). Archived weather data of Environment Canada. Available at: https://climate.weather.gc.ca/historical_data/search_historic_data_e.html (Accessed: November 18, 2018)

ESRI (2018). ArcGIS Desktop: Release 10.6.1. Redlands, CA: Environmental Systems Research Institute.

Fisher, J. A., Jacob, D. J., Soerensen, A. L., Amos, H. M., Steffen, A., & Sunderland, E. M. (2012). Riverine source of Arctic Ocean mercury inferred from atmospheric observations. Nature Geoscience, 5(7). https://doi.org/10.1038/ngeo1478

Forest, A., Osborne, P. D., Curtiss, G., & Lowings, M. G. (2016). Current surges and seabed erosion near the shelf break in the Canadian Beaufort Sea: A response to wind and ice motion stress. Journal of Marine Systems, 160, 1-16. https://doi.org/10.1016/j.jmarsys.2016.03.008

Francis, O. P., Panteleev, G. G., & Atkinson, D. E. (2011). Ocean wave conditions in the Chukchi Sea from satellite and in situ observations. Geophysical Research Letters, 38(24). https://doi.org/10.1029/2011GL049839

French, H. M. (2018). The Periglacial Environment (Fourth). England: John Wiley & Sons. https://doi.org/10.1002/9781118684931

Fritz, M., Wetterich, S., Meyer, H., Schirrmeister, L., Lantuit, H. & Pollard, W. H. (2011). Origin and Characteristics of Massive Ground Ice on Herschel Island (Western Canadian Arctic) as revealed by Stable Water Isotope and Hydrochemical Signatures. Permafrost and Periglacial Processes, 22(1):26 - 38. https://doi.org/10.1002/ppp.714

Fritz, M., Wetterich, S., Schirrmeister, L., Meyer, H., Lantuit, H., Preusser, F. & Pollard, W. H. (2012). Eastern Beringia and beyond: Late Wisconsinan and Holocene landscape

dynamics along the Yukon Coastal Plain, Canada. Palaeogeography, Palaeoclimatology, Palaeoecology, Vol. 319–320, 28-45. http://dx.doi.org/10.1016/j.palaeo.2011.12.015

Fritz, M., Vonk, J. E., & Lantuit, H. (2017). Collapsing Arctic coastlines. Nature Climate Change, 7(1), 6–7. https://doi.org/10.1038/nclimate3188

Gordon, R. (1996). Acoustic Doppler Current Profiler, Principles of Operation, A Practical Primer. RD Instruments.

Günther, F., Overduin, P. P., Sandakov, A. V., Grosse, G. & Grigoriev, M. N. (2013). Short- and long-term thermo-erosion of ice-rich permafrost coasts in the Laptev Sea region. Biogeosciences, 10, 4297–4318. https://doi.org/10.5194/bg-10-4297-2013

Günther, F., Overduin, P. P., Yakshina, I. A., Opel, T., Baranskaya, A. V. & Grigoriev, M. N. (2015). Observing Muostakh disappear permafrost thaw subsidence and erosion of a ground-ice-rich island in response to arctic summer warming and sea ice reduction. The Cryosphere, 9, 151–178. https://doi.org/10.5194/tc-9-151-2015

Hamilton, J. M. (2001). Accurate ocean current direction measurements near the magnetic poles. The Eleventh International Offshore and Polar Engineering Conference. International Society of Offshore and Polar Engineers, 11, 656– 670.

Harper, J. R. (1990). Morphology of the Canadian Beaufort Sea coast. Marine Geology, 91(1-2), 75-91.

Hequette, A., Desrosiers, M., Hill, P. R., & Forbes, D. L. (2001). The influence of coastal morphology on shoreface sediment transport under storm-combined flows, Canadian Beaufort Sea. Journal of coastal research, 507-516.

Hiles, C. E., Buckham, B. J., Wild, P., & Robertson, B. (2014). Wave energy resources near Hot Springs Cove, Canada. Renewable energy, 71, 598-608. https://doi.org/10.1016/j.renene.2014.06.020

Hill, P. R., Hequette, A., Ruz, M. H. & Jenner, K. A. (1990). Geological investigations of the Canadian Beaufort Sea Coast. Contract Report for Atlantic Geoscience Centre. Geological Survey Cananda, Open File 2387.

Hoque, M. A., & Pollard, W. H. (2009). Arctic coastal retreat through block failure. Canadian Geotechnical Journal, 46(10), 1103–1115. https://doi.org/10.1139/T09-058

IPCC (2019). Summary for Policymakers. In: Pörtner, H.-O., Roberts, D.C., Masson-Delmotte, V., Zhai, P., Tignor, M., Poloczanska, E., Mintenbeck, K., Nicolai, M., Okem, A., Petzold, J., Rama, B., Weyer, N. (eds.) IPCC Special Report on the Ocean and Cryosphere in a Changing Climate. In press.

Irrgang, A. M., Lantuit, H., Manson, G. K., Günther, F., Grosse, G., & Overduin, P. P. (2018). Variability in rates of coastal change along the Yukon coast, 1951 to 2015. Journal of Geophysical Research: Earth Surface, 123. https://doi.org/10.1002/2017JF004326

Irrgang, A. M., Lantuit, H., Gordon, R. R., Piskor, A., & Manson, G. K. (2019). Impacts of past and future coastal changes on the Yukon coast - Threats for cultural sites, infrastructure, and travel routes. Arctic Science, 5(2), 107-126. https://doi.org/10.1139/as-2017-0041

Jakobsson, M., Mayer, L., Coakley, B., Dowdeswell, J. A., Forbes, S., Fridman, B. & et al. (2012). The international bathymetric chart of the Arctic Ocean (IBCAO) version 3.0. Geophysical Research Letters, 39(12). https://doi.org/10.1029/2012GL052219

Jones, B. M., Farquharson, L. M., Baughman, C. A., Buzard, R. M., Arp, C. D., Grosse, G. & et al. (2018). A decade of remotely sensed observations highlight complex processes linked to coastal permafrost bluff erosion in the Arctic. Environmental Research Letters, 13(11). https://doi.org/10.1088/1748-9326/aae471

Jong, D., Tanski, G., Bröder, L., Haghipour N., Eglinton, T., Lantuit, H. & Vonk, J. (2018). Composition and fate of permafrost organic carbon in the Arctic nearshore zone of Yukon, Canada. Poster presented at: 5th European Conference on Permafrost (EUCOP), Jun 23 - Jul 1, 2018, Chamonix-Mont Blanc, France.

Joseph, A. (2014). Measuring ocean currents, Tools, technologies and data, 1. ed. Elsevier, Amsterdam.

Khon, V. C., Mokhov, I. I., Pogarskiy, F. A., Babanin, A., Dethloff, K., Rinke, A., & Matthes, H. (2014). Wave heights in the 21st century Arctic Ocean simulated with a regional climate model, Geophysical Research Letters, 41(8), 2956–2961. https://doi.org/10.1002/2014GL059847

Lammers, R. B., Shiklomanov, A. I., Vörösmarty, C. J., Fekete, B. M. & Peterson, B. J. (2001). Assessment of contemporary Arctic river runoff based on observational discharge records. Journal of Geophysical Research: Atmosphere, 106, 3321–3334.

Lantuit, H., & Pollard, W. H. (2008). Fifty years of coastal erosion and retrogressive thaw slump activity on Herschel Island, southern Beaufort Sea, Yukon Territory, Canada. Geomorphology, 95(1-2), 84–102. https://doi.org/10.1016/j.geomorph.2006.07.040

Lantuit, H., Rachold, V., Pollard, W. H., Steenhuisen, F., Ødegård, R., & Hubberten, H.-W. (2009). Towards a calculation of organic carbon release from erosion of Arctic coasts using non-fractal coastline datasets. Marine Geology, 257(1-4), 1–10. https://doi.org/10.1016/j.margeo.2008.10.004

Lantuit, H., Atkinson, D., Overduin, P., Grigoriev, M., Rachold, V., Grosse, G., & Hubberten, H.-W. (2011). Coastal erosion dynamics on the permafrost-dominated Bykovsky Peninsula, north Siberia, 1951-2006. Polar Research, 30(1). https://doi.org/10.3402/polar.v30i0.7341

Lantuit, H., Overduin, P. P., Couture, N., Wetterich, S., Aré, F., Atkinson, D., & et al. (2012). The Arctic coastal dynamics database: A new classification scheme and statistics on Arctic permafrost coastlines. Estuaries and Coasts, 35(2), 383–400. https://doi.org/10.1007/s12237-010-9362-6

Lantuit, H., Overduin, P. P., & Wetterich, S. (2013). Recent progress regarding permafrost coasts. Permafrost and Periglacial Processes, 24(2), 120–130. https://doi.org/10.1002/ppp.1777

Last, J. (2019). 'They're trying to rush us': Tuktoyaktuk relocating homes to soon, says resident. CBC News, Toronto, August 9, 2019. Available at: https://www.cbc.ca/news/canada/north/tuktoyaktuk-relocating-homes-erosion-1.5239765 (Accessed: August 30, 2019).

Lewkowicz, A. G. (1990). Morphology, Frequency and Magnitude of Active Layer Detachment Slides, Fosheim Peninsula, Ellesmere Island, N.W.T. Final Proceedings, Fifth Canadian Permafrost Conference. Université Laval, Quebec City, pp. 111–118.

Lilly, J. M. (2019). jLab: A data analysis package for Matlab v. 1.6.6, http://www.jmlilly.net/jmlsoft.html

Manson, G. K., Davidson-Arnott, R. G. D., & Ollerhead, J. (2016). Attenuation of Wave Energy by Nearshore Sea Ice: Prince Edward Island, Canada. Journal of Coastal Research,32(2), 253 - 263. https://doi.org/10.2112/JCOASTRES-D-14-00207.1

Moore, G. W. K., Schweiger, A., Zhang, J., & Steele, M. (2019). Spatiotemporal variability of sea ice in the arctic's last ice area. Geophysical Research Letters, 46. https://doi.org/10.1029/2019GL083722

Mulligan, R. P., Perrie, W., & Solomon, S. (2010). Dynamics of the Mackenzie River plume on the inner Beaufort shelf during an open water period in summer. Estuarine, Coastal and Shelf Science, 89(3), 214-220. https://doi.org/10.1016/j.ecss.2010.06.010

Murkowski, L. (2019). Unlocking Arctic Energy Is Vital for Alaska and America. Wall Street Journal, New York, September 11, 2019. Available at: https://www.wsj.com/articles/unlocking-arctic-energy-is-vital-for-alaskaand-america-11568243056?mod=searchresults&page=1&pos=16 (Accessed: October 1, 2019).

National Data Buoy Center (2019). Available at: https://www.ndbc.noaa.gov/ (Accessed: July 4, 2019)

NGDC (2019). Magnetic Field Calculators. National Centers for Environmental Information. Available at: https://www.ngdc.noaa.gov/geomag/calculators/magcalc.shtml#declination, (Accessed: August 14, 2019).

Obu, J., Lantuit, H., Fritz, M., Grosse, G., Günther, F., Sachs, T., & Helm, V. (2016). LiDAR elevation data of Yukon Coast and Herschel Island in 2012 and 2013. https://doi.org/10.1016/j.geomorph.2016.02.014

O'Connor, M. J. (1984). Surficial Geology and Granular Resources southeast of Herschel Island.

Onset (2012). HOBO® U20 Water Level Logger (U20-001-0x and U20-001-0x-Ti) Manual. Available at: https://www.onsetcomp.com/files/manual_pdfs/12315-E-MAN-U20.pdf (Accessed: November 23, 2018.)

Orlinsky, K. (2016). Apocalypse Tourism? Cruising the Melting Arctic Ocean, Come aboard! Let's sail the once-impenetrable Northwest Passage. Bloomberg Businessweek, New York, September 8, 2016. Available At: https://www.bloomberg.com/features/2016-crystal-serenity-northwest-passage-cruise/ (Accessed: August 27, 2019)

Overduin, P. P., Strzelecki, M. C., Grigoriev, M. N., Couture, N., Lantuit, H., St-Hilaire-Gravel, D. & et al. (2014). Coastal changes in the Arctic. Geological Society, London, Special Publications, 388(1), 103-129. https://doi.org/10.1144/SP388.13

Overeem, I., Anderson, R. S., Wobus, C. W., Clow, G. D., Urban, F. E., & Matell, N. (2011). Sea ice loss enhances wave action at the Arctic coast. Geophysical Research Letters, 38. https://doi.org/10.1029/2011GL048681

Pelletier, B. R., & Medioli, B. E. (2014). Environmental Atlas of the Beaufort Coastlands. Geological Survey of Canada, Open File Report 7619. https://doi.org/10.4095/294601

Prapuolenis, E. (2019). Arctic Melt Heightens U.S. Rivalry With Russia on the Northern Front (Video), Wall Street Journal, New York, July 15, 2019. Available at: https://www.wsj.com/video/arctic-melt-heightens-us-rivalry-with-russia-on-the-northern-front/89A25742-BEC7-459C-B908-8EABFA674C6A.html (Accessed: August 28, 2019).

Rampton, V. N. (1982). Quaternary geology of the Yukon Coastal Plain. Geological Survey of Canada, Bulletin 317. https://doi.org/10.4095/111347

RBR Ltd. (2017). RBRsolo³ D Datasheet.

RBR Ltd. (2018a). Wave Processing v4. Available on request at: https://rbr-global.com/support/

RBR Ltd. (2018b). RSKtools v3.0.0. Available at: https://rbr-global.com/support/matlab-tools.

RBR Ltd. (2019). Ruskin v. 2.9.0. Available at: https://rbr-global.com/products/software

Saetra, Ø., Carrasco, A., Röhrs, J., & Burud, A. (2018). Arctic Ocean Wave analysis and Forecast Product ARCTIC_ANALYSIS_FORECAST_WAV_002_010. Copernicus, Marine Environment Monitoring Service.

Schuster, P.F., Schaefer, K.M., Aiken, G.R., Antweiler, R.C., Dewild, J.F., Gryziec, J.D. & et al. (2018). Permafrost stores a globally significant amount of mercury. Geophysical Research Letters 45(3), 1463– 1471. https://doi.org/10.1002/2017GL075571

Schwanghart, W. & Scherler, D. (2014). Short Communication: TopoToolbox 2 – MATLAB-based software for topographic analysis and modeling in Earth surface sciences. Earth Surface Dynamics, 2, 1-7. https://doi.org/10.5194/esurf-2-1-2014

Serreze, M. C., & Barry, R. G. (2011). Processes and impacts of Arctic amplification: A research synthesis. Global and Planetary Change, 77(1–2), 85–96. https://doi.org/10.1016/j.gloplacha.2011.03.004

Signell, R. & Bhate, S. (2013). Netcdf-Java ToolBox for Matlab-njTBX. SourceForge. Available at: https://sourceforge.net/projects/njtbx/ (Accessed: July 23, 2019).

Singhal, G., Panchang, V. G., & Nelson, J. A. (2013). Sensitivity assessment of wave heights to surface forcing in Cook Inlet, Alaska. Continental Shelf Research, 63, 50-62. https://doi.org/10.1016/j.csr.2012.02.007

Stroeve, J. C., Markus, T., Boisvert, L., Miller, J., & Barrett, A. (2014). Changes in Arctic melt season and implications for sea ice loss, Geophysical Research Letters, 41, 1216–1225. https://doi.org/10.1002/2013GL058951

Swail, V. R., Cardone, V. J., Callahan, B., Ferguson, M., Gummer, D. J. & Cox, A. T. (2007). The MSC Beaufort Wind and Wave Reanalysis. Proc. 10th Int. Workshop on Wave Hindcasting and Forecasting and Coastal Hazard Symp., North Shore, Oahu, Hawaii, WMO/IOC Joint Technical Commission for Oceanography and Marine Meteorology.

Tanski, G., Lantuit, H., Ruttor, S., Knoblauch, C., Radosavljevic, B., Strauss, J. & et al. (2017). Transformation of terrestrial organic matter along thermokarst-affected permafrost coasts in the Arctic. Science of The Total Environment, 581, 434-447. https://doi.org/10.1016/j.scitotenv.2016.12.152

Tanski, G., Wagner, D., Knoblauch, C., Fritz, M., Sachs, T., & Lantuit, H. (2019). Rapid CO2 release from eroding permafrost in seawater. Geophysical Research Letters, 46. https://doi.org/10.1029/2019GL084303

Teledyne RD Instruments Inc. WorkHorse Sentinel ADCP User´s Guide (2001)

Teledyne RD Instruments Inc. WorkHorse Monitor / Sentinel User's Guide (2007).

Teledyne RD Instruments Inc. Workhorse Sentinel Datasheet (2008).

Teledyne RD Instruments Inc. Velocity Software User´s Guide (2017).

Terrey, E. A., Brumley, B.H. & Strong, B. (1999a). Measuring waves and currents with and upward-looking ADCP. Proceedings of the IEEE Sixth Working Conference on Current Measurement, San Diego, CA,66–71. https://doi.org/10.1109/CCM.1999.755216

The WAVEWATCH III® Development Group (WW3DG) (2016). User manual and system documentation of WAVEWATCH III® version 5.16. Tech.Note 329, NOAA/NWS/NCEP/MMAB, College Park, MD, USA.

Thomson, J. & Rogers, E. W. (2014). Swell and sea in the emerging Arctic Ocean. Geophysical Research Letters 41(9), 3136–3140. https://doi.org/10.1002/2014GL059983

Thomson, R. E. & Emery, W. J. (2014). Data analysis methods in physical oceanography. Newnes.

Tolman, H. L. (2008). A mosaic approach to wind wave modeling. Ocean Model. 25, 35-47. https://doi.org/10.1016/j.ocemod.2008.06.005

Tsai, C. H., Huang, M. C., Young, F. J., Lin, Y. C., & Li, H. W. (2005). On the recovery of surface wave by pressure transfer function. Ocean Engineering, 32(10), 1247-1259. https://doi.org/10.1016/j.oceaneng.2004.10.020

UN Environment (2019). Frontiers 2018/19: Emerging Issues of Environmental Concern. United Nations Environment Programme, Nairobi, March 4, 2019. Available at: https://www.unenvironment.org/resources/frontiers-201819-emerging-issues-environmental-concern (Accessed: August 27, 2019).

Vonk, J. E., Sanchez-Garcia, L., van Dongen, B. E., Alling, V., Kosmach, D., Charkin, A. & et al. (2012). Activation of old carbon by erosion of coastal and subsea permafrost in Arctic Siberia. Nature, 489, 137–140. https://doi.org/10.1038/nature11392

Vonk, J. E., Semiletov, I. P., Dudarev, O. V., Eglinton, T. I., Andersson, A., Shakhova, N. & et al. (2014). Preferential burial of permafrost derived organic carbon in Siberian-Arctic shelf waters. Journal of Geophysical Research: Oceans, 119, 8410–8421. https://doi.org/10.1002/2014JC010261

Vonk, J. E., Tank, S. E., Bowden, W. B., Laurion, I., Vincent, W. F. & et al. (2015). Reviews and syntheses: Effects of permafrost thaw on Arctic aquatic ecosystems. Biogeosciences, 12(23), 7129–7167. https://doi.org/10.5194/bg-12-7129-2015

WAMDI Group (1988). The WAM model, A third generation ocean wave prediction model. Journal of Physical Oceanography, 18, 1775-1810. https://doi.org/10.1175/1520-0485(1988)018<1775:TWMTGO>2.0.CO;2

Watts, J. (2018). Arctic warming: scientists alarmed by 'crazy' temperature rises. The Guardian, London, February 27, 2018. Available at: https://www.theguardian.com/environment/2018/feb/27/arctic-warming-scientists-alarmed-by-crazy-temperature-rises (Accessed: August 24, 2019).

Wegner, C., Bennett, K. E., de Vernal, A., Forwick, M., Fritz, & et al. (2015). Variability in transport of terrigenous material on the shelves and the deep Arctic Ocean during the Holocene. Polar Research, 34. https://doi.org/10.3402/polar.v34.24964

Weingartner, T. J., Danielson, S. L., Potter, R. A., Trefry, J. H., Mahoney, A., Savoie, M. & et al. (2017). Circulation and water properties in the landfast ice zone of the Alaskan Beaufort Sea. Continental Shelf Research, 148, 185-198. http://dx.doi.org/10.1016/j.csr.2017.09.001

Weingartner, T. J., Danielson, S. L., Okkonen, S. R., (2009). Circulation and Water Property Variations in the Nearshore Alaskan Beaufort Sea, Final Report. U.S. Department of Interior, Minerals Management Service, Anchorage, Alaska. OCS Study MMS 2005-028.

Wen, P. (2018). China unveils plan for 'Polar Silk Road' across the Arctic. The Independent, London, January 26, 2018. Available at: https://www.independent.co.uk/news/world/asia/china-polar-silk-road-arctic-xi-jinping-shipping-global-warming-a8178891.html (Accessed: September 1, 2019).

Wessel, P., & Smith, W. H. F. (1996). A Global Self-consistent, Hierarchical, High-resolution Shoreline Database, Journal of Geophysical Research, 101, 8741-8743.

White, D., Hinzman, L., Alessa, L. & et al. (2007). The arctic freshwater system: Changes and impacts. Journal of Geophysical Research, Biogeosciences, 112(G4). https://doi.org/10.1029/2006JG000353

Williams, W. J., & Carmack, E. C. (2015). The‘interior’shelves of the Arctic Ocean: Physical oceanographic setting, climatology and effects of sea-ice retreat on cross-shelf exchange. Progress in Oceanography, 139, 24-41. https://doi.org/10.1016/j.pocean.2015.07.008

Woods Hole Oceanographic Institution (2019). Arctic Ocean Circulation. Available at: https://www.whoi.edu/know-your-ocean/ocean-topics/polar-research/arctic-ocean-circulation/ (Accessed: October 18, 2019).

Xylem Inc. (2012). CastAway User's Manual 1.5.

Zingel, A. (2019). Protecting Tuktoyaktuk from coastal erosion could cost $50M, says mayor. CBC, Toronto, April 12, 2019. Available at: https://www.cbc.ca/news/canada/north/coastal-erosion-tuktoyaktuk-needs-more-money-1.5095115 (Accessed: August 21, 2019).

Zhang, J., Lindsay, R., Schweiger, A., & Steele, M. (2013). The impact of an intense summer cyclone on 2012 Arctic sea ice retreat, Geophysical Research Letters, 40(4), 720–726. https://doi.org/10.1002/grl.50190

Zhang, J., Schweiger, A., Steele, M., & Stern, H. (2015). Sea ice floe size distribution in the marginal ice zone: Theory and numerical experiments. Journal of Geophysical Research: Oceans, 120(5), 3484-3498. https://doi.org/10.1002/2015JC010770

Appendix

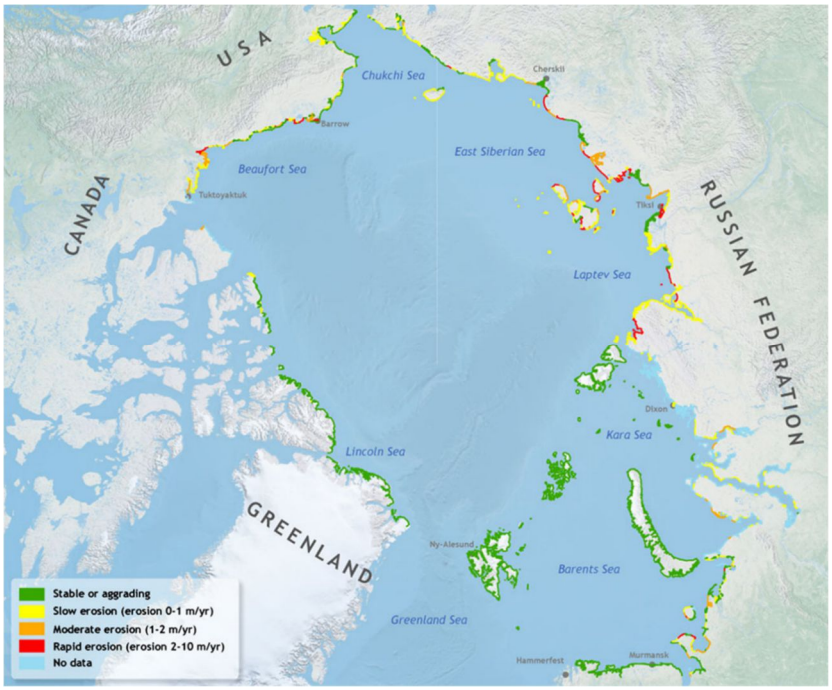

Appendix A: Map of coastal shoreline change rates along the Arctic, from Lantuit et al. (2012).

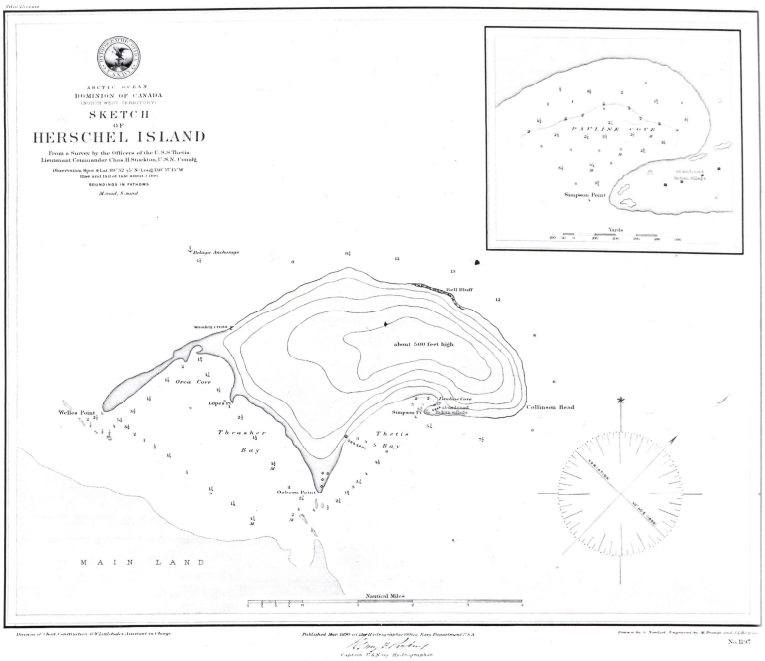

Appendix B: Historical map of Herschel Island from Burn (2012).

Acknowledgments

I thank my supervisors Prof. Dr. Hugues Lantuit and Dr. George Tanski, for their great insights into the science of the arctic and their support for preparation, field work as well as processing and writing this thesis. I also want to thank colleagues at Alfred-Wegener Institute in Potsdam, colleagues from the Nunataryuk project and fellow geoscience students from the University of Potsdam for their inspiration and exchange of knowledge.

I am thankful to the expedition team of the Yukon Coast 2018 expedition for great time in field and the support with field activities. I would like to thank the Yukon Coast 2015 summer expedition team for the in-situ measurements that I was able to analyse.

I would like to thank Peter, Frankie, Sam and the other inhabitants of Inuvik and Aklavik, that supported us in our activities and shared their fantastic knowledge and culture. Finally, I want to thank my friends, parents and family for their endless support.

Selbstständigkeitserklärung

Hiermit versichere ich, dass ich die vorliegende Arbeit ohne Hilfe Dritter und ohne Zuhilfenahme anderer als der angegebenen Quellen und Hilfsmittel angefertigt habe. Die den benutzten Quellen wörtlich oder inhaltlich entnommenen Stellen sind als solche kenntlich gemacht.

Die „Richtlinie zur Sicherung guter wissenschaftlicher Praxis für Studierende an der Universität Potsdam (Plagiatsrichtlinie) - Vom 20. Oktober 2010“, im Internet unter http://uni-potsdam.de/ambek/ambek2011/1/Seite7.pdf, habe ich zur Kenntnis genommen.

_____

Datum, Unterschrift

Anmerkung: Die Onlineversion dieser Arbeit wurde einer zusätzlichen typographischen Korrektur unterzogen.